X-RAY ANALYSIS OF HIGH MASS X-RAY BINARY PULSARS

A THESIS SUBMITTED TO
THE GRADUATE SCHOOL OF NATURAL AND APPLIED SCIENCES
OF
MIDDLE EAST TECHNICAL UNIVERSITY

BY

ŞEYDA ŞAHİNER

IN PARTIAL FULFILLMENT OF THE REQUIREMENTS
FOR
THE DEGREE OF DOCTOR OF PHILOSOPHY
IN
PHYSICS

AUGUST 2015

Approval of the thesis:

X-RAY ANALYSIS OF HIGH MASS X-RAY BINARY PULSARS

submitted by **ŞEYDA ŞAHİNER** in partial fulfillment of the requirements for the degree of **Doctor of Philosophy in Physics Department, Middle East Technical University** by,

Prof. Dr. Gülbin Dural Ünver
Dean, Graduate School of **Natural and Applied Sciences** _____

Prof. Dr. Mehmet T. Zeyrek
Head of Department, **Physics** _____

Prof. Dr. Altan Baykal
Supervisor, **Physics Department, METU** _____

Assoc. Prof. Dr. Sıtkı Çağdaş İnam
Co-supervisor, **E. E. Eng. Dept., Başkent Uni.** _____

Examining Committee Members:

Prof. Dr. Sacit Özdemir
Astronomy and Space Sciences Dept., Ankara Uni. _____

Prof. Dr. Altan Baykal
Physics Department, METU _____

Prof. Dr. Nilgün Kızıloğlu
Physics Department, METU _____

Assoc. Prof. Dr. Sinan Kaan Yerli
Physics Department, METU _____

Assoc. Prof. Dr. Ünal Ertan
Faculty of Eng. and Natural Sciences, Sabancı Uni. _____

Date: _____

I hereby declare that all information in this document has been obtained and presented in accordance with academic rules and ethical conduct. I also declare that, as required by these rules and conduct, I have fully cited and referenced all material and results that are not original to this work.

Name, Last Name: ŞEYDA ŞAHİNER

Signature   :

ABSTRACT

X-RAY ANALYSIS OF HIGH MASS X-RAY BINARY PULSARS

Şahiner, Şeyda

Ph.D., Department of Physics

Supervisor   : Prof. Dr. Altan Baykal

Co-Supervisor : Assoc. Prof. Dr. Sıtkı Çağdaş İnam

August 2015, 118 pages

In this thesis, X-ray properties of three high mass X-ray binary (HMXB) pulsars are analysed, using the data of X-ray satellites such as *RXTE*, *INTEGRAL* and *Swift*. Selected sources belong to different subgroups of the HMXB family. The first system, 4U 1907+09 is a classical wind-fed supergiant system with persistent X-ray emission; although it shows irregular flares and dips. SWIFT J1729.9–3437 and SWIFT J0513.4–6547 are newly discovered transient systems. Although the counterpart of SWIFT J1729.9–3437 could not be detected, its properties are in agreement with highly obscured wind-fed supergiant systems. SWIFT J0513.4–6547 resides in a *Be* X-ray binary system.

Timing studies of 4U 1907+09 shows that the pulsar entered to a new spin-down episode during the 4.5 years of monitoring campaign. Pulse period fluctuations of the source are consistent with noise processes implying a random walk. Orbital variations in spectral parameters and occurrence of dip states are also examined. Results show that the probability of observing a dip state is higher

for certain orbital phases. The column density is also changing with orbital period, giving clues on the geometry of the accretion and the structural properties of the matter. Outburst observations of SWIFT J1729.9–3437 are used to identify the timing and spectral properties of the source. The pulse frequency and its derivative are measured as $1.8734(8) \times 10^{-3}$ Hz and $6.42(6) \times 10^{-12}$ Hz s^{-1}, respectively. In addition a possible orbital period is detected as 15.3 days. The pulse and orbit periods place SWIFT J1729.9–3437 among the wind-fed supergiant systems in the Corbet diagram. Furthermore, X-ray spectrum, defined by a power law with a high energy cut-off, is highly absorbed ($n_H = 8.27 \times 10^{22}$ cm^{-2}). The two outbursts from SWIFT J0513.4–6547 are investigated for temporal and pulse-phase dependent variations in X-ray spectral properties. Two different models equally fit well the overall spectrum of 2009 outburst, however spectral parameters are unusual for both. A power law with a high energy cut-off model gives the lowest cut-off energy ($E_{cut} = 5.04$ keV) among HMXBs, where as a power law plus blackbody model gives the highest blackbody temperature ($kT = 1.89$ keV).

Keywords: Accretion, accretion disks, accretion torques, neutron stars, accretion powered pulsars, X-ray binaries

ÖZ

YÜKSEK KÜTLELİ X-IŞINI ÇİFT YILDIZ SİSTEMİ ATARCALARININ X-IŞINI ANALİZİ

Şahiner, Şeyda

Doktora, Fizik Bölümü

Tez Yöneticisi : Prof. Dr. Altan Baykal

Ortak Tez Yöneticisi : Doç. Dr. Sıtkı Çağdaş İnam

Ağustos 2015 , 118 sayfa

Bu tezde *RXTE*, *INTEGRAL* ve *Swift* gibi X-ışını uydularından elde edilen veriler kullanılarak, üç adet yüksek kütleli X-ışını çift yıldız (HMXB) sistemi atarcasının X-ışını özellikleri analiz edilmiştir. Seçilen kaynaklar HMXB ailesinin farklı alt gruplarına aittir. İlk kaynak 4U 1907+09, düzensiz parlamalar ve batışlar (dip) göstermesine rağmen sürekli X-ışını emisyonu yapan klasik bir rüzgar beslemeli süperdev sistemidir. SWIFT J1729.9–3437 ve SWIFT J0513.4–6547 ise yeni keşfedilmiş süreksiz sistemlerdir. SWIFT J1729.9–3437'nin bileşen yıldızı saptanamamış olsa da, özellikleri yüksek derecede perdelenmiş rüzgar belsemeli süperdev sistemler ile uyumludur. SWIFT J0513.4–6547 ise bir *Be* X-ışını çift yıldız sisteminde ikamet etmektedir.

4U 1907+09'un zamanlama çalışmaları göstermiştir ki, 4.5 yıllık gözetleme kampanyası boyunca atarca yeni bir yavaşlama (spin-down) evresine girmiştir. Kaynağın puls periyodundaki dalgalanmalar, serbest yürüyüş (random walk) ifade

eden gürültü prosesleri ile uyumludur. Tayfsal parametrelerdeki ve batma halinin (dip state) meydana gelme sıklığındaki yörüngesel değişimler de ayrıca incelenmiştir. Sonuçlar göstermektedir ki, batma halinin gözlemlenme olasılığı belirli yörünge fazları için daha fazladır. Kolon yoğunluğu da yörünge periyodu ile değişmekte olup, kütle aktarım geometrisi ve maddenin yapısal özellikleri hakkında ipuçları vermektedir. SWIFT J1729.9–3437'nin patlama gözlemleri, kaynağın zamanlama ve tayfsal özelliklerini belirlemek için kullanılmıştır. Puls frekansı ve frekans türevi, sırasıyla $1.8734(8) \times 10^{-3}$ Hz ve $6.42(6) \times 10^{-12}$ Hz s^{-1} olarak ölçülmüştür. Ayrıca, 15.3 günlük bir muhtemel yörünge periyodu saptanmıştır. Bu puls ve yörünge periyotları, SWIFT J1729.9–3437'yi Corbet diyagramında rüzgar beslemeli süperdev sistemleri arasına yerleştirmektedir. Ayrıca, yüksek enerji kesimli (cut-off) güç yasası (power law) ile tanımlanan X-ışını tayfı, yüksek derecede soğurulmuştur ($n_H = 8.27 \times 10^{22}$ cm^{-2}). SWIFT J0513.4–6547'nin iki patlaması, X-ışını tayfsal özelliklerindeki zamana ve puls fazına bağlı değişimler için incelenmiştir. 2009 patlamasının genel tayfı, iki farklı model ile eşit şekilde iyi uydurulabilmektedir, fakat her ikisi için de tayfsal parametreler olağandışıdır. Yüksek enerji kesimli güç yasası HMXB'ler arasındaki en düşük kesim enerjisini ($E_{cut} = 5.04$ keV) vermekte iken, güç yasası ve karacisim modeli en yüksek karacisim sıcaklığını ($kT = 1.89$ keV) vermektedir.

Anahtar Kelimeler: Kütle aktarımı, kütle aktarım diskleri, kütle aktarım torkları, nötron yıldızları, aktarım güçlü atarcalar, X-ışını çift yıldız sistemleri

to nature

ACKNOWLEDGEMENTS

I am sincerely grateful to my supervisor Prof. Dr. Altan Baykal for his invaluable guidance and continuous encouragement throughout my graduate study. His scientific perspective remarkably inspires and enriches my progress as a scientist. I am also indebted very much to my co-supervisor Assoc. Prof. Dr. S. Çağdaş İnam for his constructive advises and comments. Our extensive discussions nourished this study. I would also like to pay tribute to Prof. Dr. Ümit Kızıloğlu for the server systems he administers, so that we do not have to cope with any of the software related problems. He is also the one who introduced me the field of X-ray astronomy.

I would like to thank my colleagues in METU Astrophysics group, being a part of this family is a wonderful opportunity. I particularly thank to M. Mirac Serim for his unconditional efforts on theoretical discussions from scratch and his help on dealing with any technical problems encountered during this work.

I especially appreciate Prof. Dr. Mustafa Savcı and Dr. Selma Şenozan Baş for always being nearby during the hard times. Our long five o'clock coffee time conversations on variety of subjects made everything more tolerable. I also thank Prof. Dr. Sibel Başkal for the reinforcing talks along the journey of learning that all living beings should be treated as equals. We share the same compassion on choosing a vegan life style.

I feel very lucky since Ruki is involved in my life as my first dog housemate. She became the most powerful source of happiness and relaxation during the stressful times. Past months would really be emotionally harder without her.

TABLE OF CONTENTS

LIST OF TABLES

LIST OF FIGURES

FIGURES

CHAPTER 1

INTRODUCTION

X-ray binary (XRB) systems are the brightest point-like sources of the X-ray sky, which get enormous attention during the last decades owing to discoveries done by the X-ray space missions. These systems consist of a normal star and a collapsed compact object; a white dwarf, a neutron star or a black hole. X-rays are basically produced by the transfer of matter from the nuclearly active mass donor to the dense compact object. XRBs are divided into sub-classes according to the type of the compact object, since the physical processes are different for apiece. On the other hand XRBs are also divided into two considering the mass of the donor. If the mass of the donor (M_*) is less than 1 $M_\odot$ the systems are called low mass X-ray binary (LMXB), or if $M_* > 10$ $M_\odot$ they are called high mass X-ray binary (HMXB) (Chaty 2011). The galactic population of XRBs is reported to have more than 300 members (Liu et al. 2006, 2007). 187 of them are LMXBs, whereas 114 are HMXBs.

This work focuses on the HMXBs that host X-ray pulsars as the compact object. Pulsars are highly magnetized rotating neutron stars. Typical magnetic field strength of X-ray pulsars are at the order of $\sim 10^{12}$ Gauss. As soon as the transferred matter from the donor star is influenced by the magnetic field lines, it is directed along the poles (see Figure 1.1). While the in-falling matter loses its gravitational energy, released energy is transformed into X-ray emission. When the magnetic axis and the rotation axis of a neutron star are not aligned, the polar emission is modulated with rotation. The modulation is observed as pulsations in X-rays if the emission beams pass through the line of sight and the
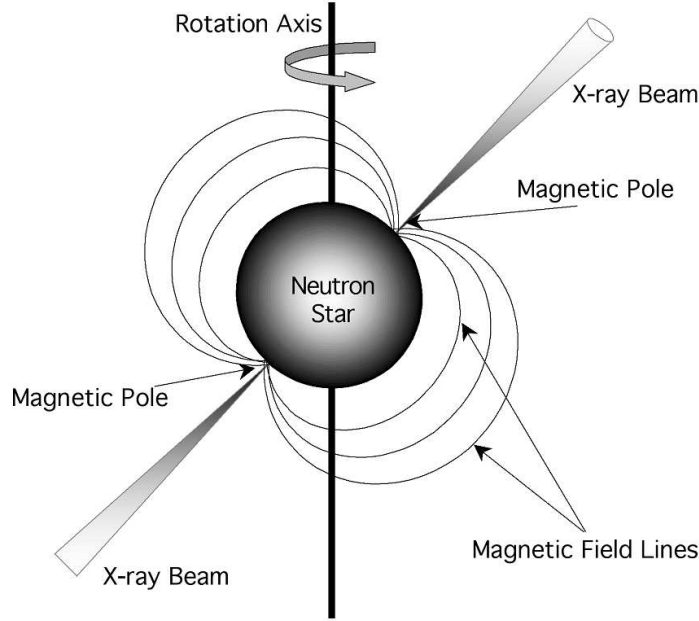
Figure 1.1: Basic diagram of a X-ray pulsar

source is defined as a pulsar. Pulsars in X-ray binaries are also called "Accretion Powered Pulsars" (APPs) and a full review of their properties are available in White et al. (1983), Nagase (1989) etc. APPs reside mostly in HMXB systems, although there are several exceptions with low mass companions. Important physical processes for APPs are accretion of matter through the magnetosphere, radiation transfer in the strong magnetic field, angular momentum transfer via accreting matter and the response of the pulsar to the accretion torque (Nagase 1989).

HMXBs hosting pulsars are further categorized by the type of the companion (see Figure 1.2). The companion may be either a *Be* type star or a OB supergiant star. In fact the supergiant group is divided into two according to the mass transfer mechanism at work. If the supergiant fills its Roche Lobe the mass is transferred via an accretion disk and the system is called disk-fed. If the companion does not fill its Roche Lobe the strong wind of the supergiant is the main supply of material and the system is called wind-fed. A study by Corbet (1984, 1986) showed that these different groups of systems form different clusters on the spin period (P_s) versus orbital period (P_o) diagram, i.e. the Corbet

2
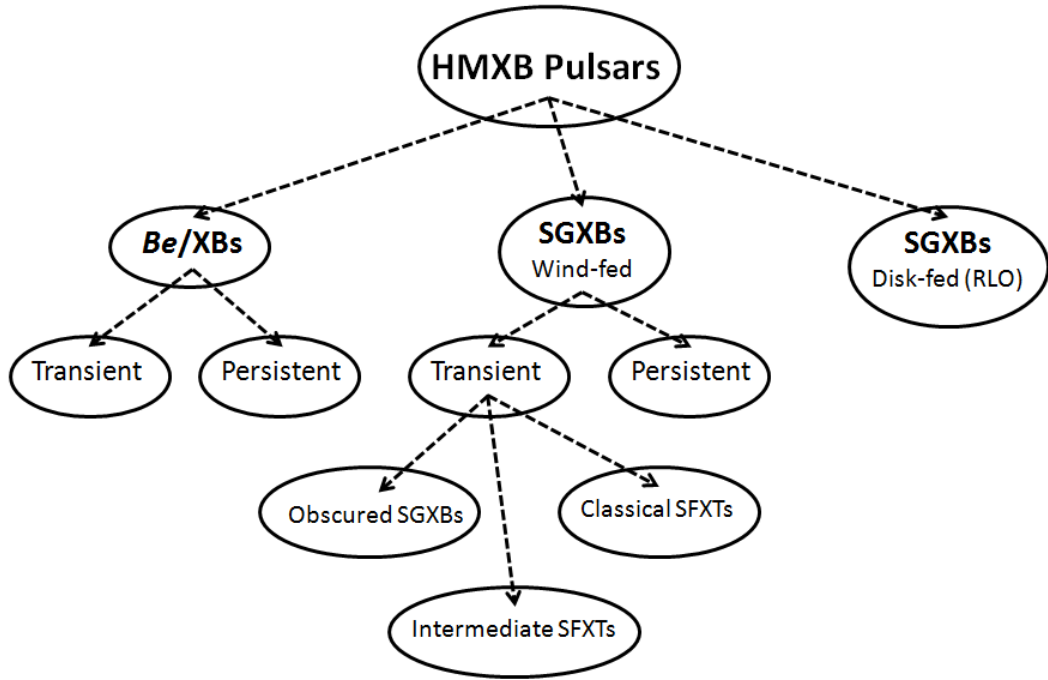
Figure 1.2: Subgroups of HMXBs that host pulsars.

diagram. The most up-to-date version of this diagram is given in Figure 1.3.

1.1 Classification of HMXB Pulsars

1.1.1 Be/XBs

The major group of HMXBs (63 of the galactic HMXBs, Reig 2011) is formed by the systems with Be type companion. In Be/XBs, the mass donor is a young main sequence star that does not fill its Roche Lobe. The stellar wind of the Be star constitutes a circumstellar disk around the equatorial region of the mass donor, which is commonly called the decretion disk. The existence of this disk is proven by the emission lines (Balmer series) emerging from the dense gas of the disk, which are also the reason why the affix "e" (meaning emission) is added to the spectral type. As the pulsar interacts with the material of the decretion disk, accretion takes place. The orbit of these systems are relatively wide and
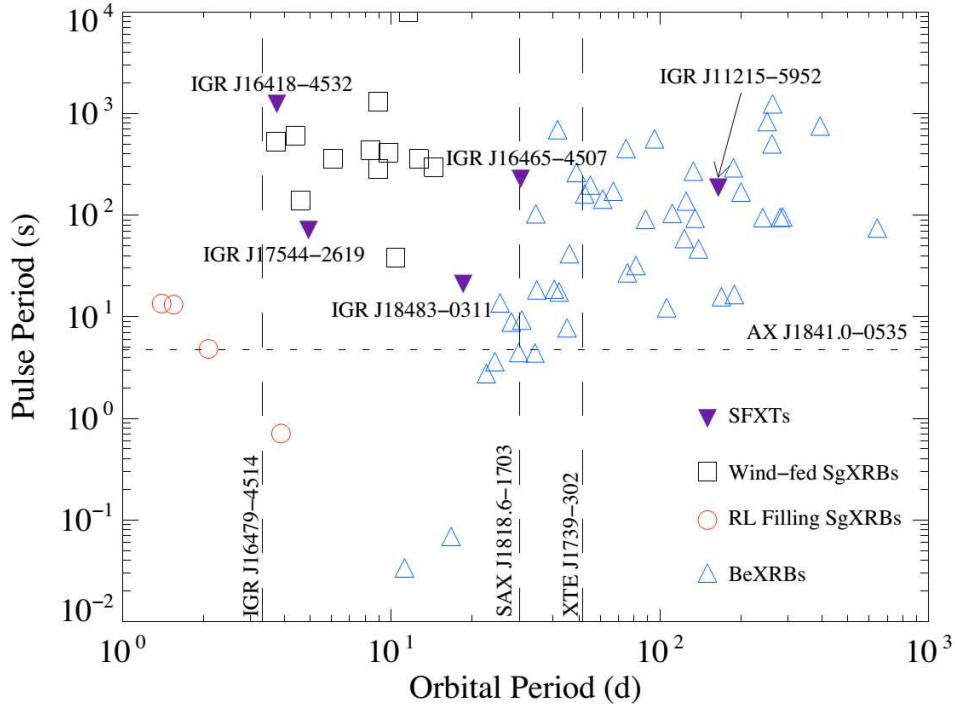
Figure 1.3: Up-to-date version of the Corbet Diagram (Drave et al 2012).

moderately eccentric ($P_o \geq 20$ days, $e \geq 0.3$; Reig 2011), resulting in changing interaction conditions during the orbital path. Therefore the X-ray emission of most Be/XBs is of transient nature. However there are several persistent sources (e.g. X Per) with lower luminosity ($L_x \approx 10^{34-35}$ erg s^{-1}) that display less variability. Persistent Be/XBs have low eccentric or circular orbits which naturally explains the continuity of the X-ray emission.

Transient Be/XBs have very low luminosities during the quiescence phase ($L_x \leq 10^{33}$ erg s^{-1}), where as their outbursts may reach up to Eddington limit ($L_x \sim 10^{38}$ erg s^{-1}). The distinct characteristics of the outbursts display that there are two different types (Stella, White & Rosner 1986). Type I outbursts periodically occur in every orbital passage from the periaston phases and they generally have luminosities $\sim 10^{36-37}$ erg s^{-1}. On the other hand, Type II outbursts are irregular events that occur during immense mass ejection episodes of the companion. The X-ray luminosities of these giant outbursts are observed to be larger than 10^{37} erg s^{-1} and the decay of the event proceeds for a longer time,

4

generally enclosing several orbits.

As the population of Be/XBs with known periodicities have grown in the past decades, the spin period of pulsars in Be/XBs are still strongly correlated with the orbital periods of the systems, as it is firstly demonstrated by Corbet (1984, 1986) (see Fig. 1.3). However the clear power law relation between P_s & P_o dispersed along the sides of the $P_s \propto P_o^2$ line in the log-log plot. The positive correlation between P_s and P_o implies that longer spin period pulsars reside in wider systems. In systems with wide orbits, the accreting matter is supplied from outer regions of the decretion disk, and accretion rates are lower as a consequence of the lower density material of the outer disk. Since the equilibrium period is inversely proportional to the accretion rate with $\sim \dot{M}^{-3/7}$ (Waters & van Kerkwijk 1989), the P_s of pulsars on wider orbits are larger as an outcome of lower accretion rates.

1.1.2 SGXBs

Young and massive ($\sim 15 - 30$ M$_\odot$) companions in the SGXBs are of O or B spectral type which have strong stellar winds. This class is further divided into two according to the following confinement; Roche Lobe (RL) filling or underfilling. Since the matter supplied by a RL filling companion forms an accretion disk, these systems are called disk-fed SGXBs. On the other hand, RL undefilling systems are called wind-fed SGXBs.

1.1.2.1 Disk-fed SGXBs

HMXBs with supergiant companions that lose material via Roche Lobe Overflow (RLO) have persistently high accretion rates and therefore high luminosities ($\sim 10^{37-38}$ erg s^{-1}) . These bright sources are close binaries with orbital periods less than 4 days. Sufficient accretion of matter forms an accretion disk around the pulsar which accelerates its rotation (spin-up) via supplying steady angular momentum from the disk material. As a consequence, the pulsars in disk-fed systems are rapid rotators with spin periods in the range $0.7 - 14$ s. There are

only 4 known systems in this class; they are SMC X–1, LMC X–4, Cen X–3 and RX J0648.1–4419. In Figure 1.3 (denoted with circles), a negative correlation appears between the P_s and P_o of RL filling SGXBs although they constitute very few points.

1.1.2.2 Wind-fed SGXBs

Supergiant companions that underfill their RL have dense and highly inhomogeneous stellar winds that provide material for the accretion process onto the pulsar. Wind-fed SGXBs have orbits that are wider than the orbits of disk-fed SGXBs. The rates of mass loss via stellar wind can be rather large being at the order of $10^{-6} - 10^{-5}$ M$_\odot$ yr^{-1}, however accretion of wind material continues with an inefficient process such that the fraction of accreted matter to the lost matter is as low as $\sim 10^{-3}$ (Frank et al 2002). Therefore the lower accretion rates of wind-fed SGXBs result in lower X-ray luminosities ($L_x \approx 10^{35-36}$ erg s^{-1}) than that of the disk-fed SGXBs. However, the inhomogeneity of the wind may cause large variations in the accretion rate and therefore the brightness of the source on short time scales, such that X-ray flares of the order of $\sim 10^{36-37}$ erg s^{-1} may occur.

The spin periods of pulsars in wind-fed SGXB systems are longer in the range $\sim 100 - 1000$ s, as a result of the lower accretion rates. Wind-fed systems form a distinct group on the upper left corner of the Corbet Diagram (see Fig. 1.3) which show no clear correlation with the orbital period of the system. The mass accretion variability due to the changing nature of the winds, produce unsteady supply of angular momentum and external torque fluctuations cause altering episodes of spin-up and spin-down both on short and /or long time scales and change the spin periods of the pulsars impulsively.

In the last decade, the population of the known wind-fed SGXBs has grown rapidly, thanks to the discoveries by the INTEGRAL satellite (Chaty 2011). The high energy emission of many new SGXBs is detected with the IBIS/ISGRI detector which operates beyond 20 keV. The energy range making the observations independent of the absorption in soft X-rays, discovery of sources in dense

regions towards the Galactic center and in directions of Galactic arms have formed a whole new population of transient wind-fed SGXBs, apart from the historically known persistent wind-fed SGXBs. Following the growth in the population, the main concern has become to describe the physical links between the transient and persistent SGXBs and possible explanations are raised by Walter & Zurita Heras (2007) and Negueruela et al. (2008).

SFXTs   The uttermost sub-group that finally joined the family of HMXBs is the Supergiant Fast X-ray Transients (SFXTs). SFXTs are transient systems that show very short X-ray outbursts with durations in the range from 100 to 10000 seconds and these outbursts may occur recurrently (Sguera et al. 2005, 2006; Negueruela et al. 2006). The first extreme source XTE J1739-302 was discovered by the extraordinary x-ray activity that continued for only one day in 1997 (Smith et al. 1998). After 2002, regular galactic plane survey observations with *INTEGRAL* had led a rapid increase in the number of similar sources. Recently, the number of sources which are definitely identified as SFXTs have reached to 11 and the number of candidate source are about the double (Sidoli 2013).

The peak luminosities of SFXT outburst reach up to 10^{36-37} erg s^{-1} whereas in quiescence periods their luminosities are at the order of 10^{32-33} erg s^{-1}. The dynamic range of luminosity being at the order of 3 to 5 is a common characteristic for SFXTs, which is rather very higher than the dynamic ranges of persistent SGXBs (< 20). It is also likely to detect x-ray activity with a luminosity level of 10^{33-34} erg s^{-1} outside outbursts, therefore real quiescence episodes are actually questionable. The discrimination between low level activity and quiescence is possible by the analysis of X-ray spectra. X-ray spectra of low level activity times are in agreement with the outburst spectra which can be defined by a hard power law; where as in quiescence softer spectra are observed (Sidoli et al. 2008).

The recurrent outbursts observed in some of the sources, revealed that these systems show their outbursts due to enhancement of accretion during certain orbital phases within the orbital geometry and they probably have eccentric

orbits, as a similarity to Be/XB systems. As of today pulse periods could be detected in 5 of the SFXTs, as a result these sources started taking their place in the Corbet diagram (see Fig. 1.3). Given that SFXTs spread over various regions instead of gathering about a specific place in this diagram, the hypothesis that SFXTs may form an evolutional link between SGXBs and Be/XBs has been put forward by Liu et al. (2011).

There are several mechanisms that are suggested for the explanation of transient outbursts of SFXTs (Sidoli 2009). Clumpy wind models, anisotropic winds and propeller mechanism are the most accepted ones. In the clumpy wind model (Runacres & Owocki 2005), X-ray outbursts of SFXTs are explained by rapid accretion of a dense wind clump. Negueruela et al. (2008) predict two different orbital geometries for short and rare outbursts to be observable from these systems. One of them is circular orbit outside the region where dense clumps are present and the other is wide eccentric orbit on which dense clumps may exist in certain orbital phases (e.g. periastron). Sidoli et al. (2007) assume that anisotropic wind material of the companion is accumulated at the equatorial region like in the case of Be donors. However for SFXTs, this disk-like structure is thought to be highly inclined with respect to the orbital plane such that the interaction with the material is short-lived causing the fast bursts. The propeller mechanism is described in Section 1.2.3. Bozzo et al. (2008) tried to use this mechanism to explain the high dynamic ranges of SFXTs, however their conclusion required high magnetic field ($\sim 10^{14}$ G) long spin period (~ 1000 s) systems, which are not compatible with observational facts.

Obscured SGXBs These transient systems have unusually high absorption levels in X-rays, their hydrogen column densities are generally at the order of 10^{23} cm^{-2} and may also be one more order higher. A strong intrinsic absorption in optical bands are also observed (Chaty 2011 and references therein). In the optical spectrum of the extraordinary example of IGR J16318–4848 (Filliatre & Chaty 2004), existence of many strong emission lines indicates a stratified circumstellar environment. The optical findings demonstrate that the dense absorbing material is surrounding the whole system and forming an envelope of

matter that hides the system.

There are five persistently obscured sources in our Galaxy. They are located in the direction of the Norma arm. The mass donors are of type O8– B1 and the orbital periods are less than 10 days. Their luminosities are highly variable with a dynamic range of about 20 and are at the order of 10^{36} erg s^{-1}. Obscured SGXBs may be considered as systems being in transition to the state of RLO or they may have low wind velocities (Walter et al. 2015). For example persistent systems such as GX 301–2 and 4U 1907+09 have high column densities and low wind velocities which resemble obscured sources.

1.2 Theory on Accretion

1.2.1 Accretion Power

The accretion of matter is the source for the high energy radiation in APPs. Gravitational energy release of the material, as it falls onto the magnetic poles of the neutron star, is basically transformed into EM radiation. The efficiency of the process is high for larger ratios of mass and radius, i.e. the compactness of the star. The luminosity of the emission also depends on the mass accretion rate $\dot{M}$ and is given by (Zel'dovich & Shakura 1969):

$$L_{accr} = \frac{GM\dot{M}}{R} \simeq 1.3 \times 10^{37} \dot{M}_{17} \frac{M}{M_\odot} R_6^{-1} \ \text{erg s}^{-1} \qquad (1.1)$$

where G is the gravitational constant, $\dot{M}_{17}$ is $\dot{M}$ in units 10^{17} gr s^{-1} and R_6 is radius in units of 10^6 cm. Therefore X-ray luminosities at the order of 10^{37} erg s^{-1} require accretion rates $\sim 10^{-9} M_\odot$ yr^{-1} assuming a radius of 10 km and a mass of 1.4 $M_\odot$ for a neutron star.

As the luminosity increases, a limiting case occurs when the force exerted by radiation is equal to the gravitational force. Assuming a spherically symmetric accretion of ionized Hydrogen, the accreting matter is subjected to the force $\frac{\sigma_T S}{c}$, where σ_T is the Thomson scattering cross-section, S is the radiant energy

flux $(\dfrac{L}{4\pi\,R^2})$ and c is the speed of light. Equating this with the gravitational force $\dfrac{GMm_p}{R^2}$ the maximum value for the accretion luminosity is defined as the Eddington limit;

$$L_{Edd} = \frac{4\pi\,GM\,m_p\,c}{\sigma_T} \simeq 1.3 \times 10^{38}\,\frac{M}{M_\odot}\ \ \text{erg s}^{-1} \tag{1.2}$$

where m_p is the mass of proton. For $L_x > L_{Edd}$ radiation pressure dominates and accretion is halted. It should be kept in mind that this theoretical limit is only valid in the vicinity of above assumptions. However the practical properties of accretion is far more complex, therefore a source with a luminosity exceeding the Eddington limit would not be a contradiction.

1.2.2 The Magnetosphere

The magnetic properties of the star and accretion are closely related in the vicinity of a pulsar. Near the pulsar, there exists an empty cavity called the magnetosphere, in which the dominant force is the magnetic force and therefore the accreting matter is stopped at the boundary. The radius of this region is calculated by equating the magnetic and plasma pressure together, such that (Lamb et al. 1973);

$$\frac{B^2(r)}{4\pi} \approx \rho(r)\,\nu^2(r) \tag{1.3}$$

here ρ and ν are density and velocity of the plasma as a function of radial distance r and B is the magnetic field strength. Assuming that the accreting plasma is freely falling with velocity $\nu_{ff}(r) \approx \sqrt{\frac{2GM}{r}}$ and that the flow of matter is spherically symmetric with accretion rate $\dot{M} = 4\pi r^2\,\rho(r)\,\nu(r)$ the magnetospheric radius, i.e. Alfvén radius, is calculated as (Davidson & Ostriker 1973, Lamb et al. 1973):

$$r_A = \left(\frac{\mu^4}{2GM\dot{M}^2}\right)^{1/7} \approx 3 \times 10^8 \left[\frac{\mu_{30}^4}{L_{37}^2\,R_6^2}\left(\frac{M}{M_\odot}\right)\right]^{1/7}\ \ \text{cm} \tag{1.4}$$

10

where μ_{30} is the magnetic moment in units of 10^{30} G cm^3 and L_{37} is the luminosity of accretion in units of 10^{37} erg s^{-1}.

1.2.3 Accretion Disk

As the companion loses matter via RLO, the escaping material is transferred into the RL of the neutron star from the inner Lagrangian point L_1. Accretion rates in the case of RLO are typically at the order of $10^{-10} - 10^{-9}$ $M_\odot$ yr^{-1}. In this process the angular momentum of the accreting matter is high, so that it cannot be directly accreted (Frank et al. 2002). The matter is accelerated by gravitational attraction and consequently the trajectory of the gas stream is ballistic around the neutron star. The effect of the high initial angular momentum molds a circular orbit for the stream. The disk matter intersects and collides with itself and settles down by dissipation of energy via shock mechanisms. Loss of energy causes the gas to sink into closer orbits slowly spiraling inwards, therefore angular momentum is lost. When the system lacks any external torques, the lost momentum is transferred outwards by internal torques, resulting in a gain of angular momentum for the matter at outer parts and they spiral outwards. Throughout this process matter is spread radially inward and outward and a disk of gas stream is formed.

Finally the motion of the material becomes Keplerian rotation of a geometrically thin, optically thick accretion disk. The angular velocity of matter in a certain radius r is found by balancing the gravitational force $\dfrac{GM}{r^2}$ with the centrifugal force $\Omega_K^2 r$ as;

$$\Omega_K(r) = \sqrt{\frac{GM}{r^3}} \tag{1.5}$$

which is called the Keplerian angular velocity. The differential rotation means that the angular velocities of the material moving in different radii are different and the lapse of neighbouring streamlines bring about chaotic thermal and turbulent motions of fluid elements such that viscous stresses are generated in the disk. The effect of shear viscosity vanishes in the case of steady symmetric
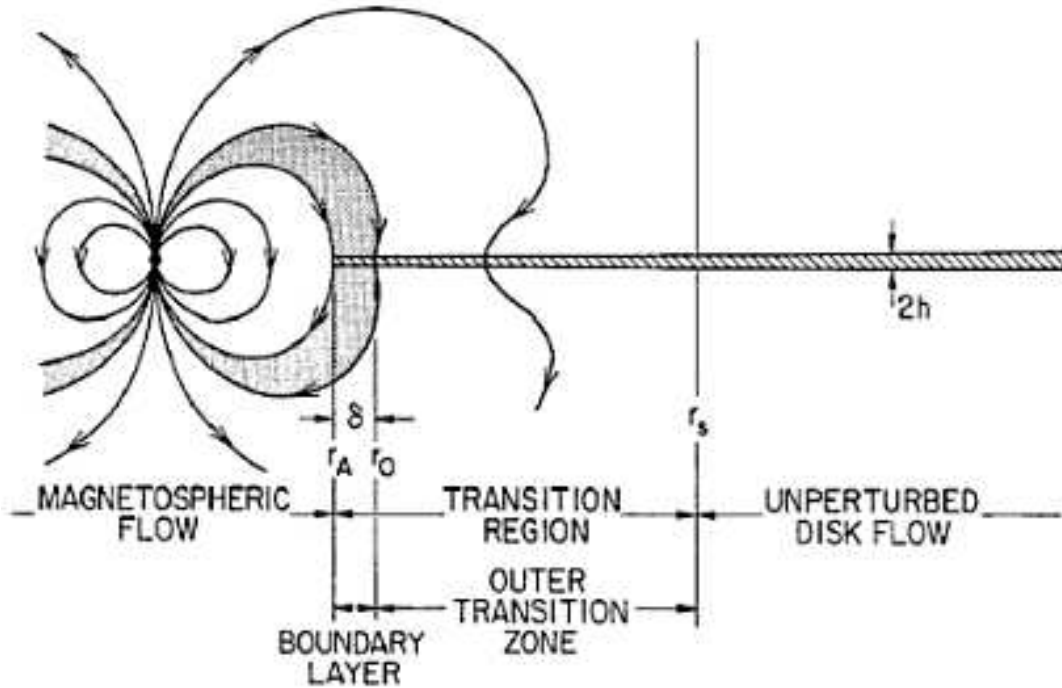
Figure 1.4: Schematics showing regions of disk – magnetosphere interaction (Ghosh & Lamb 1978).

flows, however it becomes important when hydrodynamical instabilities are considered. Magnetic fields may also play a major role as a ground to the viscosity generation (Frank et al. 2002 and references therein).

Disk & Magnetosphere Interaction The material of the accretion disk needs to penetrate into the magnetosphere of the neutron star in order to establish the accretion onto the poles. The configuration that describes the interaction of the disk and the magnetosphere is revised by Ghosh & Lamb (1978, 1979a). The disk flow outside the magnetosphere, compresses the field lines and pinches them near the disk plane (see Figure 1.4). Far outside a screening radius of r_s the magnetic field does not perturb the disk flow. At the transition region magnetic stresses remove angular momentum from the disk. The inner transition zone is a boundary layer between the magnetosphere and the inner disk, at which the viscous shear stresses vanish for $r < r_o$. The flow is no more Keplerian at this zone and the disk is coupled the neutron star, where the inner

disk matter rotates with the same angular velocity that of the star. Several magneto-hydrodynamic processes and turbulent diffusion are responsible for the coupling and penetration of matter into the magnetosphere (Lamb 1989, Ghosh 2007). Once the plasma descends into the region $r > r_A$ it follows the field lines, reaches to the magnetic poles and finally matter is accreted onto the compact object.

Propeller Effect The radius at which the disk matter co-rotates with the neutron star plays an important role in the incidence of accretion. The co-rotation radius r_{co} is defined by $\Omega_K(r_{co}) = \Omega_s$; where Ω_s is the angular velocity of the neutron star. Accretion is only possible if the inner disk can reach the co-rotation radius. Therefore r_{co} should fall to the region of magnetospheric flow that is; it should be less than the radius r_A. If $r_{co} < r_A$ a centrifugal barrier inhibits accretion and this mechanism is named as the 'propeller' effect (Stella et al. 1986). There are two possible conditions that bring propeller mechanism to work. If the rotation of the neutron star is faster than the rotation of the inner disk or if the accretion rate so low that the material pressure is not enough overcome the magnetic pressure to bring the inner disk inside the magnetosphere; matter is propelled and accretion stops. When $r_{co} > r_A$ accretion continues until the condition $r_{co} = r_A$ is reached by the change of physical properties such as mass accretion rate and spin period P_s of the neutron star. For the exact radius of equivalence spin period is named as the equilibrium period P_{eq} that is given by;

$$P_{eq} \approx 23 \; \mu_{30}^{6/7} \; \dot{M}_{15}^{-3/7} \left(\frac{M_x}{M_\odot} \right)^{-5/7} \; \text{s} \qquad (1.6)$$

where $\dot{M}_{15}$ is mass accretion rate in units of 10^{15} g s^{-1} (Reig 2011 and references therein). P_{eq} corresponds to a maximum which can be reached for a specific accretion rate.

13

1.2.4 Wind Accretion

Accretion from the strong stellar winds of early type companions is commonly referred as Bondi-Hoyle-Lyttleton accretion because of the pioneering work of the authors (Hoyle & Lyttleton 1939; Bondi & Hoyle 1944). In 1970s, the effort of Elsner & Lamb (1977) nourished the theory of wind accretion. The topic is still being developed further by a recent approach to the subject by Shakura et al. (2014).

Supergiant companions which do not fill their RLs, have high mass loss rates at the order of $10^{-6} - 10^{-5}$ $M_\odot$ yr^{-1}. Accretion from the wind material is an inefficient process; however the sources are sufficiently powered by the process since the wind material is in immense amounts. The accretion flow is mainly radial with a relative velocity of the wind with respect to orbital velocity of the neutron star, defined as $\nu_{rel}^2 = \nu_{wind}^2 + \nu_{orbit}^2$. The accretion radius is related as;

$$r_{acc} \approx \frac{2GM}{\nu_{rel}^2} \tag{1.7}$$

and it is at the order of 10^{10} cm for typical wind velocities. The accretion rate would then become;

$$\dot{M} = \pi r_{acc}^2 \, \rho_w(r) \, \nu_w(r) = 4\pi (GM)^2 \, \frac{\rho_w(r) \, \nu_w(r)}{\nu_{rel}^2} \tag{1.8}$$

where ρ_w is the wind density. Since the accretion luminosity is proportional to the mass accretion rate, the velocity and density of the wind material has the primary importance in the process.

The overall characteristics of persistent wind-fed sources can basically be explained by the above plain theory. However most sources are very variable in any time scale, which is probably due to the violent nature of the winds. Accretion of highly inhomogeneous material structured in clumps of different density, result in unpredictable variations in X-ray light curves of the SGXBs.
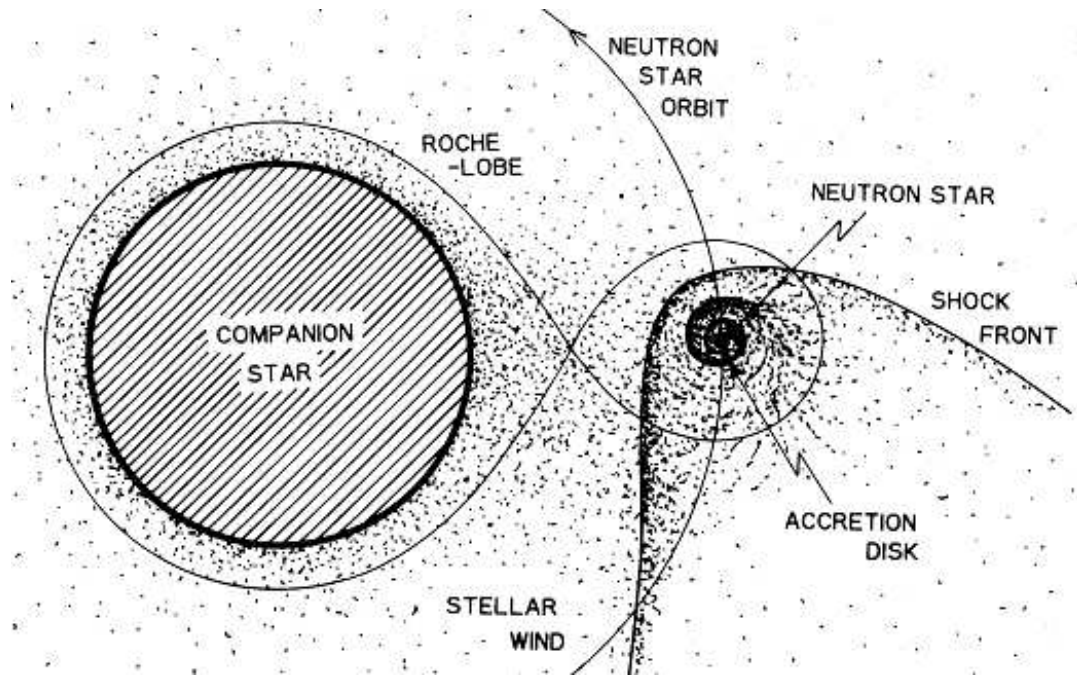
Figure 1.5: Schematics showing disk formation from wind material below a shock front (Nagase 1989).

Wind & Magnetosphere Interaction   When the accretion of wind plasma starts, as it approaches to the central star with high velocity the magnetic field of the neutron star is compressed. As the material and the magnetic field interact with each other, the magnetic pressure decelerates the flow and a shock front forms due to a boundary between high and low density regions. The shock is named as magnetopause (see Figure 1.5), since the flow is paused by the magnetic field. As the flow is accumulated above the shock it is heated and it needs to be cooled in order to enter to the magnetosphere (Elsner & Lamb 1977). The cooling is implemented by inverse Compton process, where electrons are cooled by the X-ray photons. Collisions of ions by these cooled electrons cool the plasma. The cooled plasma finally becomes very dense at the boundary such that the boundary becomes unstable to perturbations. The dominant mechanism for this perturbation is the Rayleigh - Taylor instability which gives rise to the entry of matter into the magnetosphere and accretion occurs.

The velocity and density gradients of the wind material may possibly create circulation of matter forming an accretion disk around the neutron star. These

15

gradients break the symmetry of the system and excessive angular momentum content of the accreting matter give rise to a circulation of the gas stream (Ghosh 2007 and references therein). Since realistic winds are neither symmetric nor uniform the disk formation scenario is likely. The excessive amount of matter interacting with the shock front may gain angular momentum and the flow may start circulating temporarily (Blondin et al. 1990). Magneto-hydrodynamical simulations of stellar winds (Matsuda et al. 1987) show that the initial existence of small asymmetries is capable of forming accretion disks.

1.3 Thesis Content

In Chapter 2, the results of a comprehensive study on the persistent wind-fed HMXB system 4U 1907+09 based on its observations from *RXTE* and *INTE-GRAL* are introduced. Long term monitoring of the source with frequent *RXTE* pointings, gives the opportunity to derive the timing solution by connecting $\sim$ 1600 days of pulse arrival times in phase. The source is found to be in a new long term spin-down episode with a rate similar to its previous spin-down rate during the 4.5 years of monitoring. Short term fluctuations in the pulse period, observed for the first time for 4U 1907+09, are successfully interpreted as white noise in pulse frequency derivatives. Five period measurements from *INTE-GRAL* time series are also reported for times corresponding to the gap in the period history before the *RXTE* measurements. Furthermore, orbital variations in spectral characteristics and irregular dipping activities are examined. The column density variations along the orbit insight the structure of the accretion geometry and properties of the accreting matter. The statistics of the dipping episodes, in which the pulsations are interrupted and the X-ray flux decreases several orders in magnitude, is maintained for the first time. The results show that occurrence probability of dipping are certainly higher for specific orbital phases.

In Chapter 3, the X-ray properties of a new transient SWIFT J1729.9–3437, are extensively studied. The first and only outburst of the source is monitored for about three weeks in 2010. *RXTE* and *Swift* observations are used to determine

the timing parameters of the source. The pulse frequency and its derivative are accurately measured as $1.8734(8) \times 10^{-3}$ Hz and $6.42(6) \times 10^{-12}$ Hz s^{-1}, respectively. The residuals of the timing solution are further investigated by means of two possibilities. Assuming that the fluctuations represent noise processes, the order of the noise strength is found to be in agreement with other HMXBs. However, the residuals can also be interpreted as a circular orbit with a period of 15.3(2) days. The periodicities of SWIFT J1729.9–3437 place the source among the wind-fed supergiants in the Corbet diagram. The spectral characteristics of the source are also in agreement with HMXB systems. Temporal variations of the pulse profiles and hardness ratios of the source are also examined. The emission is found to be softening as the outburst flux declines, while the pulse shape changes from double-peaked to single-peaked after MJD 55406.7.

In Chapter 4, all available X-ray observations of another new transient source SWIFT J0513.4–6547 are analysed. The counterpart in the system is identified by a recent optical study as a Be type star. Two outburst activities are observed. The outburst that brought on the discovery of the source was a Type II outburst in 2009. The source re-brightened in 2014 with a lower flux, and seems to be peaking in times of optical maximum. We studied the X-ray spectra of the source and find that the continuum can equally be described by two models, a power law with a high energy cut-off or a power law plus blackbody. Further spectral study is carried by analysing $RXTE$ spectra of individual observations and pulse-phase resolved spectra during the 2009 outburst. Energy dependent pulse profiles, hardness ratios with respect to count rate and pulse phase, and flux dependence of pulse fraction are also investigated.

In the final Chapter 5, the final conclusions on the results are given.

CHAPTER 2

4U 1907+09

In this chapter, $\sim$1600 days of *RXTE* monitoring observations of 4U 1907+09 are analysed for long term X-ray spectral and timing properties of the source. In addition, previously selected *INTEGRAL* pointing observations for spectral analysis (Şahiner 2009), are analysed for the timing properties just before the *RXTE* observations. The main study is published on MNRAS with the title "*A Comprehensive Study on RXTE & INTEGRAL Observations of the X-ray Pulsar 4U 1907+09*" (Şahiner et al. 2012a) along with several other publications covering parts of the results during a 4.5 year journey (İnam et al. 2009a, Şahiner et al. 2011, Şahiner et al. 2012b).

2.1 Introduction

4U 1907+09 is an HMXB system that was discovered during the *Uhuru* survey in 1970s (Giaconni et al. 1971). The system consists of an X-ray pulsar and a blue supergiant counterpart. The binary orbit of the system is eccentric ($e \sim 0.28$) with a period of $\sim$ 8.3753 days (In't Zand et al. 1998). The pulse period of the pulsar has increased from $\sim$ 437 s (Makishima et al. 1984) to $\sim$ 442 s (Şahiner et al. 2012b) over 30 years.

The X-ray emission from 4U 1907+09 is persistent with moderate X-ray luminosity at the order of $10^{35} - 10^{36}$ erg/s . However, the system shows irregular activities such as flares and dips. Aperiodic X-ray flares are rare and reach up to a luminosity of 4×10^{36} erg/s. It is mainly claimed that, the intensity of the

source falls below the detection threshold during the dipping states (In't Zand et al. 1997). In't Zand et al. (1997) reported that no pulsations were observed throughout the dipping episodes observed by *RXTE*. Conversely, Doroshenko et al. (2012) did find that pulsed emission is sustained within the dipping states observed by *Suzaku*, and reported typical dip state luminosity to be at the order of 10^{34} erg/s. Several studies, focusing on the spectra of dipping episodes, did not find any evidence of an increased absorption (In't Zand et al. 1998, Roberts et al. 2001, Rivers et al. 2010); therefore origin of the dips are considered to be a cessation of accretion due to lower density regions within the stellar wind of the counterpart. Typical length of dipping episodes varies between few minutes to 1.5 hours.

As the pulsar orbits around its companion; the X-ray intensity of 4U 1907+09, rises two times in one orbit cycle with an orbital phase separation of $\simeq 0.5$. Primary X-ray maximum occurs at the periastron passage, where as a secondary maximum takes place at the apastron passage (Marshall & Ricketts 1980, In't Zand et al. 1998). At first; two "phase-locked" flares per orbit were supported by the existence of a circumstellar disk around a Be companion, the passage of the pulsar through the disk causing the temporal increase in the intensity (Iye 1986, Cook & Page 1987). However optical (Cox et al. 2005a, b) and infra-red (Nespoli et al. 2008) studies of the counterpart, concluded that the companion is an O8.5 Iab supergiant star, leaving the Be explanation out. This supergiant is highly reddened ($E_{(B-V)} \simeq 3.45$ mag) with a visual magnitude of 16.37. Its mass loss rate is estimated as $\dot{M} = 7 \times 10^{-6}$ $M_\odot$ yr^{-1}. The distance to the binary system is $\geq$ 5kpc.

The pulse profile of 4U 1907+09 is double-peaked below 20 keV, where as one peak disappears above 20 keV (In't Zand et al. 1998). The pulsed fraction is constant around 30 per cent, however relative intensities of the peaks differ within days (Mukerjee et al. 2001). The pulse period of the pulsar had been steadily increasing (i.e spin-down) with an average rate of $\dot{\nu} = -3.54 \times 10^{-14}$ Hz s^{-1} until 1998 (see Fig. 2.6) (Cook & Page 1987, In't Zand et al. 1998, Baykal et al. 2001, Mukerjee et al. 2001). During 2001 observations of the source, a significant decrease in the steady spin-down rate by a factor of $\sim$0.60 had been

observed (Baykal et al. 2006). Later on, *INTEGRAL* observations revealed a torque reversal to spin-up (i.e decrease in period) from MJD 53131 onwards, with a spin-up rate of 2.58×10^{-14} Hz s^{-1} (Fritz et al. 2006). Our studies on the timing properties of 4U 1907+09 presented in this work and relevant publications (İnam et al. 2009a, Şahiner 2009, Şahiner et al. 2011, Şahiner et al. 2012b), showed that the source returned to spin-down once more, with a rate close to its historical spin-down rate, which is -3.59×10^{-14} Hz s^{-1}.

The X-ray spectrum of 4U 1907+09 is compatible with basic X-ray pulsar spectra. An absorbed power law (index ~ 1.2) with an exponential cut-off at ~ 13 keV is basically used to describe the general characteristic of the continuum in several studies of the source (Schwartz et al. 1980, Marshall & Ricketts 1980, Makishima et al. 1984, Cook & Page 1987, Chitnis et al. 1993, Roberts et al. 2001, Coburn et al. 2002, Baykal et al. 2006, Fritz et al. 2006). The absorption is highly variable over the binary orbit, n$_H$ changing between 1×10^{22} cm^{-2} and 9×10^{22} cm^{-2} (In't Zand et al. 1997). Leahy (2001) and Kostka & Leahy (2010) modeled the orbital variation of the column density and decided that the double-peaked orbital profile is a consequence of an accretion from a dense stellar wind enhanced by spiral stream of material between the pulsar and its counterpart.

Other spectral features observed in the spectrum of 4U 1907+09 are *Fe* emission complex and cyclotron resonant scattering features (CRSFs). *Fe* Kα emission at 6.4 keV is reported to be narrow with an equivalent width around 50 eV (Rivers et al. 2010). Rivers et al. (2010) also detected for the first time, *Fe* Kβ emission at 7 keV in *Suzaku* spectrum of the source. CRSFs of 4U 1907+09 are discovered in high energy observations with *Ginga* (Mihara 1995, Makishima et al. 1999) and *BeppoSAX* (Cusumano et al. 1998). The fundamental line energy is ~ 19 keV, where as its second harmonic is found at ~ 39 keV. Since CRSFs are a tool to measure the surface magnetic field strength directly, for 4U 1907+09 magnetic field is calculated as 2.1×10^{12} G (Cusumano et al. 1998). The fundamental CRSF of 4U 1907+09 is found to be varying with pulse phase (Rivers et al. 2010, Maitra & Paul 2013), whereas a dependence on X-ray luminosity is only resolved as a marginal detection (Hemphill et al. 2013).
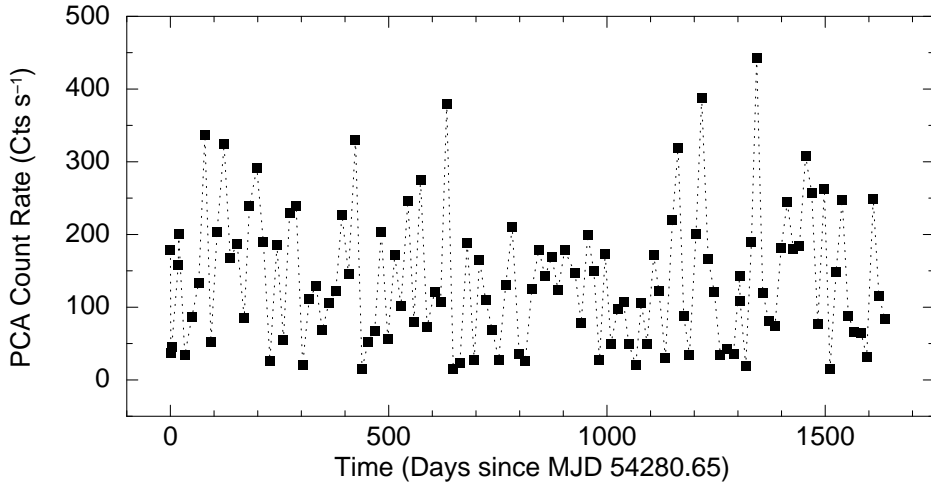
Figure 2.1: 1 day binned *RXTE*–PCA light curve of 4U 1907+09.

2.2 Observations and Data Reduction

2.2.1 *RXTE*

Monitoring observations of 4U 1907+09 with *RXTE* were held on from June 2007 until the satellite was decommissioned at the end of 2011. The source being observed for $\sim$ 2 ks in every 15 days for a 4.5 year period of time, resulted in a total exposure of 255 ks for 118 pointings. Şahiner (2009) studied the first set with proposal ID 93036 (39 observations), whereas 94036, 95350, 96366 sets are extensively analysed during this work (see Table 2.1). Daily averaged count rates from *RXTE* are plotted in Figure 2.1 in order to give an illustration of the time coverage and the variability in the intensity of the source.

RXTE consisted of three main instruments: PCA (2–60 keV; Jahoda et al. 1996), HEXTE (15–250 keV; Rothschild et al. 1998) and ASM (2–10 keV; Levine et al. 1996). In this work, data from *Proportional Counter Array* (PCA) are considered only. PCA had five co-aligned identical proportional counter units (PCUs) each with an effective area of $\sim$ 1300 cm^2. The detectors being sensitive in 2–60 keV, their energy resolution was 18% at 6 keV. The field of view (FOV) of this instrument at full width at half maximum (FWHM) was 1°. Usually PCUs were operating in groups of two or three during the observations. However PCU0

22

Table2.1: Log of *RXTE* observations of 4U 1907+09

Proposal ID	Time (MJD)	# of obs.	Exposure (ks)
93036[a]	54280 − 54825	39	74.114
94036	54839 − 55184	24	45.347
95350	55208 − 55555	26	49.433
96366	55571 − 55918	29	86.620
Total:	1638 days	118	255.514

[a] Observations analysed in Şahiner 2009.

and PCU1 had lost their propane layers due to a micro-particle hit and the data obtained by these PCUs were not reliable for spectral analysis since the data is contaminated by increased particle flux. Only PCU2 was kept on during all of the operations, therefore only PCU2 data was selected for spectral extraction in order to avoid possible calibration differences between different PCUs. No PCU selection was done for the timing analysis.

The standard tools of the software package `HEASOFT v.6.10` are used for data reduction. Applied selection criteria for data filtering consisted of elevation angles to be $\geq 10°$, offset to be $\leq 0°.02$ and electron contamination of PCU2 to be ≤ 0.1. The 'Standard2f' mode data, which had 128 energy channels, are examined for the spectral extraction. For light curve extraction, high time resolution mode 'GoodXenon' was considered. Background estimation were performed by using the estimator models supplied by the *RXTE* Guest Observer Facility (GOF) suitable for observation times (`Epoch 5C`).

2.2.2 *INTEGRAL*

The *INTEGRAL* observations selected for spectral analysis in Şahiner (2009) are considered for timing analysis in this work. The data is downloaded from the *INTEGRAL* Science Data Centre (ISDC) archive. 611 science windows (SCWs) (each ~ 3 ks) were selected from revolutions between 366 and 623 in order to
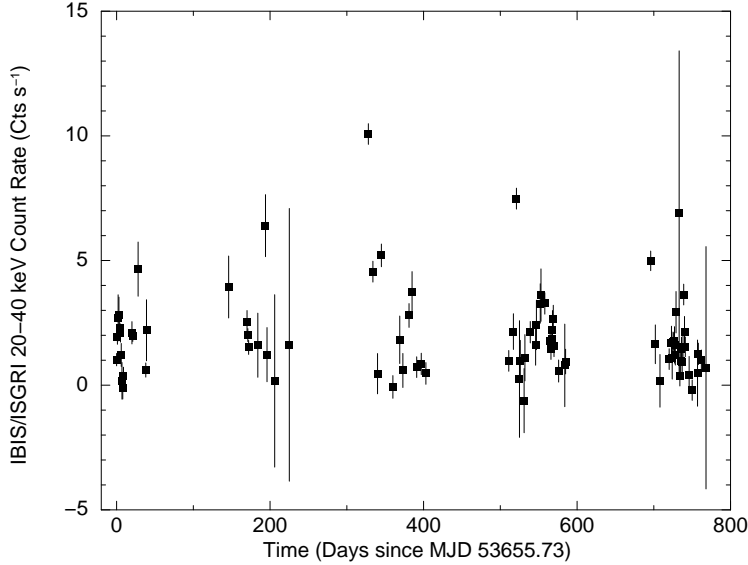
Figure 2.2: 1 day binned IBIS–ISGRI light curve of 4U 1907+09.

cover the times of the gap in the pulse period history of 4U 1907+09, just before the *RXTE* observations. Applied selection criteria included to have good times of IBIS-ISGRI above 1 ks and the source to be in the FOV with an offset smaller than 5°. A log of these observations, between October 2005 and November 2007, were given in Table 4.3 of Şahiner (2009). Daily averaged count rates are plotted in Figure 2.2.

INTEGRAL satellite (Winkler et al. 2003) consisted of four instruments: OMC (500–850 nm; Mas-Hesse et al. 2003) JEM-X (3–35 keV; Lund et al. 2003), IBIS (15 keV – 10 MeV; Ubertini et al. 2003) and SPI (20 keV – 8 MeV; Vedrenne et al. 2003). The data considered here are from *INTEGRAL Soft Gamma-Ray Imager* (ISGRI) of the *Imager on Board the INTEGRAL Satellite* (IBIS). IBIS is a coded mask instrument with a large FOV (8°.3 × 8°.0 fully coded, 29° × 29° zero response). The angular resolution at FWHM is 12'. The upper layer of this instrument is called ISGRI and it is sensitive to photon in energies from 15 keV to 1 MeV. The energy resolution of ISGRI is 8% at 60 keV (Lebrun et al. 2003).

The standard pipeline of the *INTEGRAL* software `OSA v.7.0` is used for data reduction. The data reprocessing includes the steps of gain correction, good-time handling, dead-time derivation, background correction and energy reconstruc-

24
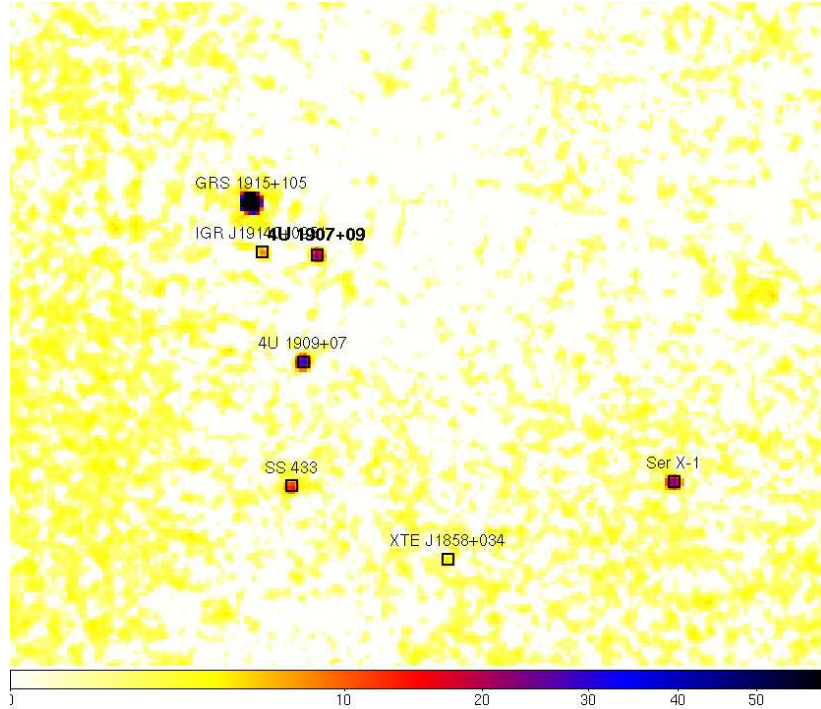
Figure 2.3: A sample for *INTEGRAL* IBIS–ISGRI significance map in 20–40 keV. Regions with labels show several bright sources in the FOV.

tion respectively. The bright sources detected in the mosaic images are Ser X-1, XTE J1855–026, 4U 1909+07, SS 433, IGR J19140+0951, GRS 1915+105 and 4U 1907+09. A sample significance map is given in Figure 2.3. Catalogue coordinates are used for the source positions. Ghosts due to coded mask modulation are cleaned from the image by selecting `SEARCHMODE==3` and `NEGMODELS==1`. In order to obtain optimal flux and signal-to-noise ratio (SNR), counts are not spread in pixels. Background is estimated in pipeline standards by using the maps provided by the ISGRI team. Resulting 20–40 keV images are used to produce light curves. The standard light curve extraction tool of the pipeline is time and disk-space consuming and it is not recommended to use it for generating high time resolution time series. An alternative algorithm called `II_LIGHT` uses Pixel Illuminated Fraction (PIF) technique, but it works only on SCW level. Therefore, light curve of each SCW is constructed with this tool and then merged to obtain the light curve of 4U 1907+09. `BARYCENT` task is used for correcting the time column as if the photons arrive to the solar system barycentre.

2.3 Timing Analysis

2.3.1 The Method

First, the time series are folded independently on trial periods to find a statistically appropriate period that gives the maximum χ^2 (Leahy et al. 1983). Then, sample pulse profiles are constructed for each observation using the preferred period. The most significant profile is chosen to be the "master" profile and other sample profiles are cross-correlated with this master profile in order to obtain the phase differences. For cross-correlation, pulse profiles are defined with Fourier harmonic representation as;

$$g(\phi) = G_o + \sum_{k=1}^{m} G_k \cos k(\phi - \phi_k) \tag{2.1}$$

$$f(\phi) = F_o + \sum_{k=1}^{m} F_k \cos k(\phi - \phi_k + \Delta\phi_k) \tag{2.2}$$

where $g(\phi)$ and $f(\phi)$ stand for the master and sample profiles (Deeter & Boynton 1985). The phase difference between the profiles, $\Delta\phi_k$, are obtained by the orthogonality relation for the harmonics;

$$\Delta\phi_k = \frac{\sum_{k=1}^{m} k G_k F_k \sin k\Delta\phi_k}{\sum_{k=1}^{m} k^2 G_k F_k \cos k\Delta\phi_k} \tag{2.3}$$

Consequently; the offsets of all pulse profiles from the master, form a series which is called the pulse arrival times. $\Delta\phi_k$ values of pulses are in between -0.5 and 0.5, therefore they need to be shifted appropriately, in order to take into account the pulse cycles during time gap between the observations. This procedure is called cycle counting, which should be repeated for different possibilities to crosscheck the ambiguities during the modelling. The cycle counts of pulses (or the pulse arrival times) are modelled according to;

$$\delta\phi = \delta\phi_o + \delta\nu(t - t_o) + \sum_{n=2}^{a} \frac{1}{n!} \frac{d^n\phi}{dt^n}(t - t_o)^n \tag{2.4}$$

26
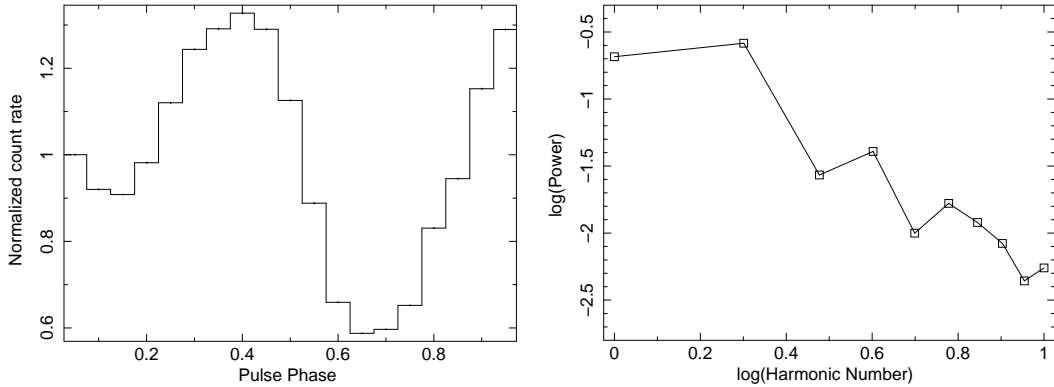
Figure 2.4: A sample pulse profile (left) and the power of the harmonics (right) obtained from the observation on MJD 55586.

which is a Taylor expansion. Here; $\delta\phi$ is the phase offset found from the timing analysis, t_o is the time epoch of the analysis, $\delta\phi_o$ is the residual offset at t_o, $\delta\nu$ is the correction to the pulse frequency and $\frac{d^n\phi}{dt^n}$ are n^{th} order derivatives of the pulse phase (e.g. for n=2, it is the pulse frequency derivative $\dot{\nu}$).

If $\delta\nu$ is significantly large, new pulse profiles are constructed with the new period and entire cross-correlation analysis is repeated for the corrected frequency until one finds the best solution. Finally, the pulse arrival times should be connected in phase, giving the right timing solution for the source.

2.3.2   Timing Solution

Background subtracted and barycentred $RXTE$–PCA light curves of the source are subjected to the timing analysis described in Section 2.3.1. 1 s binned light curves are also corrected for the binary orbital motion using the relevant parameters from In't Zand et al. (1998). Since 4U 1907+09 is known to have dipping states which may degenerate the quality of pulses, dip times are removed from the light curves used in timing analysis. Pulse profiles are constructed in 20 phase bins and represented with 10 harmonics ($m = 10$ in Eqn. 2.1). A sample pulse profile and its power spectra of harmonics are given in Figure 2.4.

$RXTE$ pulse arrival times for the ~ 1300 days are connected in phase by applying

27
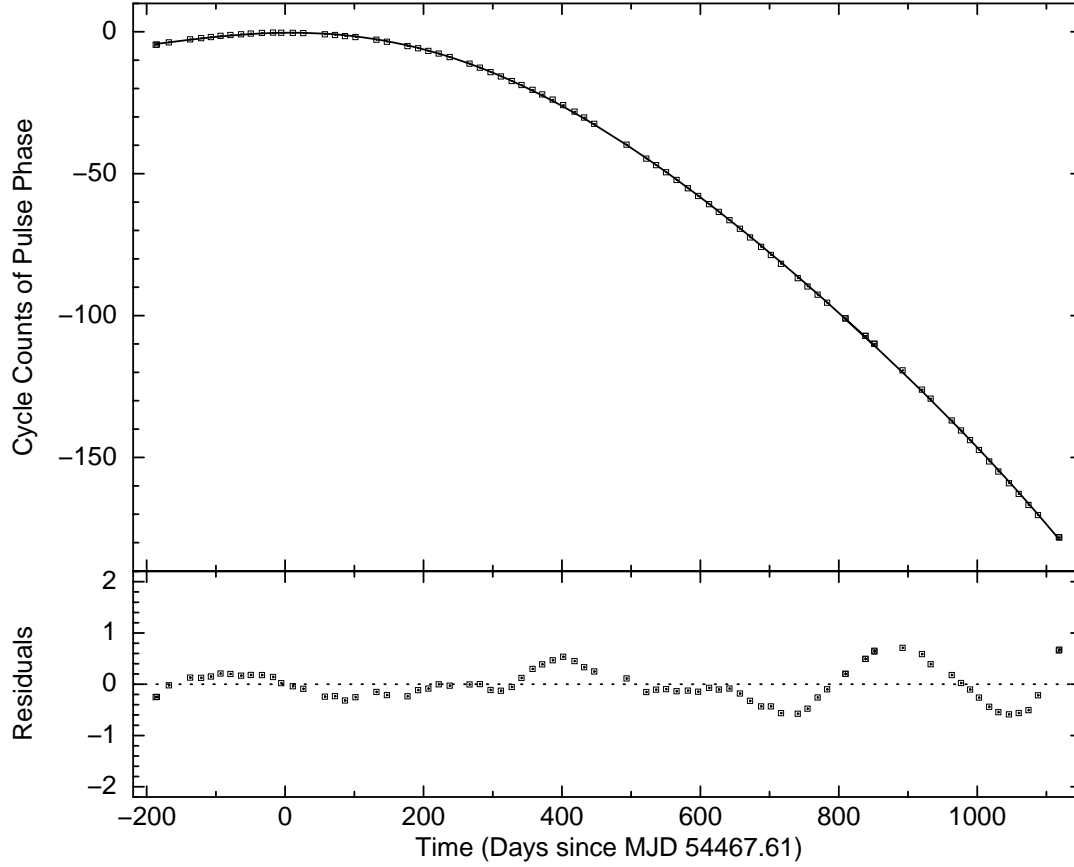
Figure 2.5: Cycle counts of pulse phase for 4U 1907+09 for MJD 54280 − 55600. The solid line represents the best-fit polynomial, which is a 5th order from of Eqn. 2.4. The residuals of the fit are given in the bottom panel.

Table2.2: Timing solution of 4U 1907+09 between MJD 54280 and 55600.

Parameter	Value
Epoch (t_o)	MJD 54467.61(6)
Pulse Period (P)	441.2088(2) s
Spin frequency (ν)	$2.2665002(8) \times 10^{-3}$ Hz
$\dot{\nu}$	$-3.672(1) \times 10^{-14}$ Hz s^{-1}
$\ddot{\nu}$	$-1.497(5) \times 10^{-21}$ Hz s^{-2}
$\dddot{\nu}$	$1.063(9) \times 10^{-28}$ Hz s^{-3}
$\ddddot{\nu}$	$-2.44(3) \times 10^{-36}$ Hz s^{-4}
RMS residual (pulse phase)	0.32

the cross-correlation techniques. Since the time span of the data is considerably long, the data is handled in smaller segments in order to avoid any possible ambiguity in cycle counting procedure. The total time span is divided into 10 segments (each $\sim$ 160 days) and the best period of each segment is determined separately. Then, the slopes of the arrival times obtained for each segment are aligned in the overlapping time intervals to facilitate the final cycle count graph given in the upper panel of Figure 2.5. The cycle counts of the pulses are fitted with the fifth order form of Eqn. 2.4. The residuals of the fit are given in the lower panel of Figure 2.5, whereas the parameters of the fit are given in Table 2.2.

Aiming to display the pulse period changes of 4U 1907+09, each pair of points in Figure 2.5 is fitted linearly. Pulse period at the mid-time of a pair is calculated from the individual derivative (i.e the slope) found from that pair. Pulse period measurements obtained, by carrying this procedure for all consecutive pairs, are given in Table 2.3. Along with the historical measurements from other studies, pulse periods are also plotted over time in the upper panel of Figure 2.6. In the lower panel of Figure 2.6, a closer view of the results from this work are presented.

The *INTEGRAL* observations of 4U 1907+09 are selected to measure periods for the times with no measurements ((B) division of Figure 2.6), just before the *RXTE* observations. 10 s binned, background subtracted and barycentered 20–40 keV IBIS–ISGRI light curves are used for this purpose. In 770 days, *INTEGRAL* data are stacked massively in five time zones (see Fig. 2.2). Timing analysis is carried out for each stack separately; therefore five periods are measured for five stacks. In one stack of data, $\sim$ 7–10 days of light curves are sampled to construct the pulse profiles for cross-correlation. Corrected pulse frequencies are acquired using a linear fit ($\delta\phi = \delta\nu(t - t_o)$) on the pulse arrival times. Pulse period measurements using *INTEGRAL* data are also given in Table 2.3 and Figure 2.6.
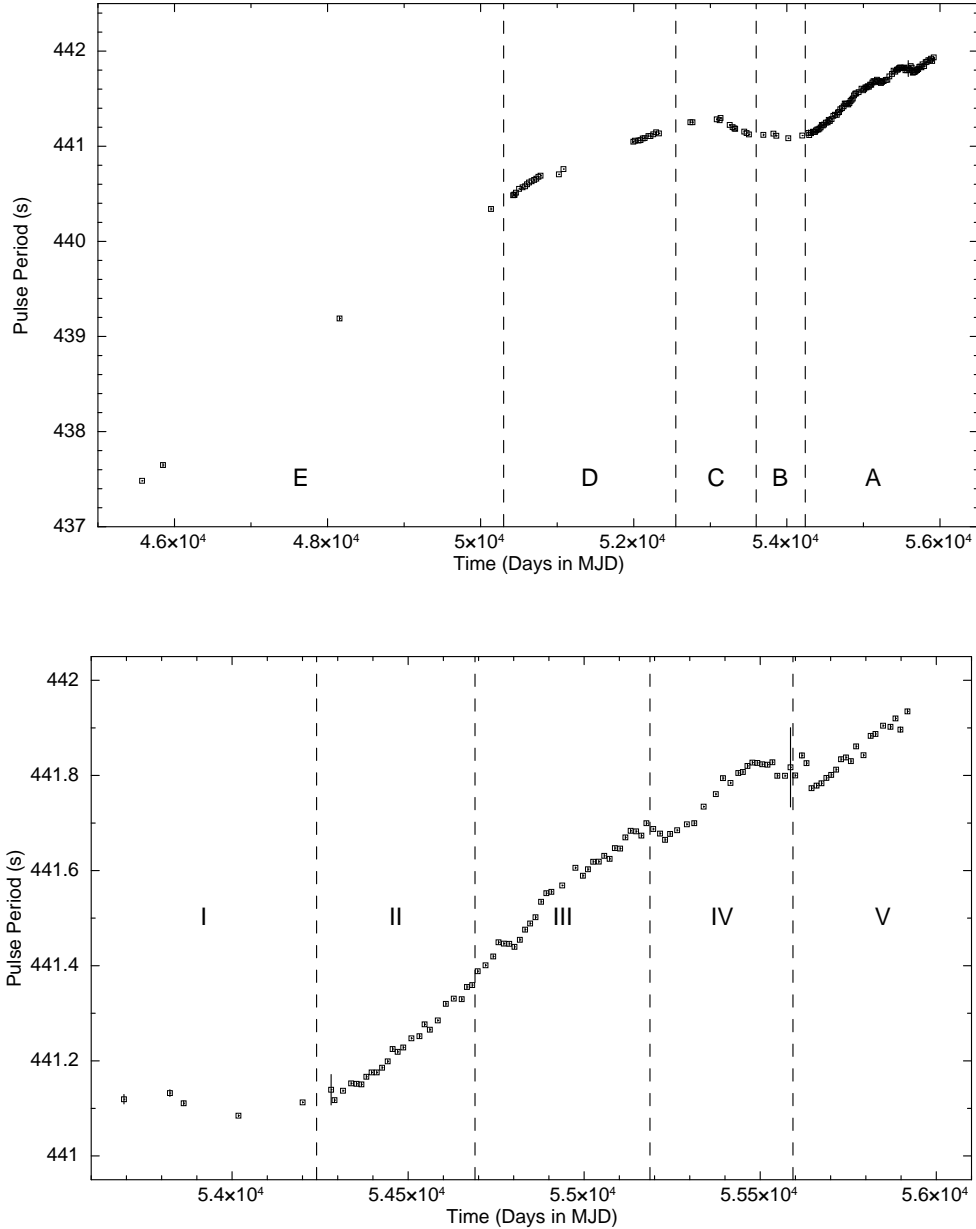
Figure 2.6: Pulse period history of 4U 1907+09. All historical measurements are plotted on the upper panel. Oldest measurements lie in region E (In't Zand et al. 1998, Mihara 1995, Cook & Page 1987, Makishima et al. 1984). The measurements from Baykal et al. (2001, 2006) are in region D, where as the measurements from Fritz et al. (2006) are in region C. The regions A & B contain the measurements of this work, which are plotted seperately on the lower panel (see Table 2.3). Region I (B on upper panel) contains the measurements from *INTEGRAL* observations. Regions II, III, IV & V contain measurements from *RXTE* observations (II: İnam et al. 2009a, III: Şahiner et al. 2011, IV: Şahiner et al. 2012a , V: Şahiner et al. 2012b).

30

Table2.3: Pulse period measurements of 4U 1907+09

Epoch (MJD)	Pulse Period (s)	Epoch (MJD)	Pulse Period (s)
$53693.0^{c}*$	441.1193 ± 0.0100	54719.7^{b}	441.4009 ± 0.0020
$53823.6^{c}*$	441.1322 ± 0.0070	54741.6^{b}	441.4195 ± 0.0037
$53862.6^{c}*$	441.1108 ± 0.0050	54756.8^{b}	441.4492 ± 0.0037
$54018.1^{c}*$	441.0847 ± 0.0020	54771.9^{b}	441.4465 ± 0.0038
$54200.4^{c}*$	441.1127 ± 0.0014	54787.2^{b}	441.4460 ± 0.0036
54281.5^{a}	441.1030 ± 0.0372	54802.1^{b}	441.4398 ± 0.0040
54291.0^{a}	441.1213 ± 0.0038	54817.2^{b}	441.4544 ± 0.0035
54315.0^{a}	441.1367 ± 0.0021	54832.1^{b}	441.4758 ± 0.0041
54338.2^{a}	441.1545 ± 0.0041	54846.6^{b}	441.4889 ± 0.0037
54353.3^{a}	441.1509 ± 0.0046	54861.8^{b}	441.5019 ± 0.0037
54367.3^{a}	441.1543 ± 0.0047	54877.5^{b}	441.5344 ± 0.0035
54381.3^{a}	441.1623 ± 0.0046	54892.7^{b}	441.5526 ± 0.0040
54396.2^{a}	441.1750 ± 0.0042	54907.0^{b}	441.5553 ± 0.0039
54410.9^{a}	441.1761 ± 0.0047	54937.6^{b}	441.5687 ± 0.0012
54426.0^{a}	441.1862 ± 0.0041	54975.3^{b}	441.6058 ± 0.0020
54442.1^{a}	441.1992 ± 0.0040	54996.5^{b}	441.5892 ± 0.0040
54456.1^{a}	441.2245 ± 0.0056	55010.7^{b}	441.6029 ± 0.0039
54470.4^{a}	441.2185 ± 0.0039	55025.6^{b}	441.6185 ± 0.0037
54486.3^{a}	441.2284 ± 0.0043	55041.4^{b}	441.6188 ± 0.0034
54509.4^{a}	441.2472 ± 0.0021	55057.0^{b}	441.6310 ± 0.0038
54532.3^{a}	441.2537 ± 0.0044	55072.3^{b}	441.6247 ± 0.0036
54546.8^{a}	441.2756 ± 0.0046	55087.2^{b}	441.6473 ± 0.0040
54561.6^{a}	441.2657 ± 0.0043	55102.0^{b}	441.6462 ± 0.0037
54584.3^{a}	441.2855 ± 0.0022	55117.2^{b}	441.6697 ± 0.0037
54607.1^{a}	441.3195 ± 0.0043	55132.0^{b}	441.6836 ± 0.0038
54629.6^{a}	441.3301 ± 0.0022	55147.4^{b}	441.6826 ± 0.0035
54652.1^{a}	441.3307 ± 0.0043	55162.5^{b}	441.6737 ± 0.0040
54667.2^{a}	441.3549 ± 0.0044	55176.8^{b}	441.6996 ± 0.0039
54682.1^{a}	441.3596 ± 0.0044	55196.2^{c}	441.6874 ± 0.0023
54697.5^{b}	441.3883 ± 0.0035	55215.3^{c}	441.6777 ± 0.0040

31

Table2.3: Continued

Epoch (MJD)	Pulse Period (s)	Epoch (MJD)	Pulse Period (s)
55229.7^c	441.6647 ± 0.0039	55618.2^d	441.8421 ± 0.0054
55243.9^c	441.6772 ± 0.0041	55631.4^d	441.8259 ± 0.0046
55264.0^c	441.6848 ± 0.0021	55645.6^d	441.7732 ± 0.0046
55291.7^c	441.6973 ± 0.0020	55659.8^d	441.7787 ± 0.0046
55312.5^c	441.6998 ± 0.0043	55673.9^d	441.7836 ± 0.0047
55339.4^c	441.7343 ± 0.0014	55687.8^d	441.7949 ± 0.0047
55373.8^c	441.7607 ± 0.0020	55701.6^d	441.8011 ± 0.0048
55394.1^c	441.7943 ± 0.0045	55715.6^d	441.8122 ± 0.0046
55415.6^c	441.7842 ± 0.0018	55729.5^d	441.8342 ± 0.0048
55437.5^c	441.8052 ± 0.0042	55743.3^d	441.8379 ± 0.0047
55450.7^c	441.8073 ± 0.0043	55757.5^d	441.8302 ± 0.0046
55463.7^c	441.8199 ± 0.0043	55772.3^d	441.8610 ± 0.0044
55477.6^c	441.8271 ± 0.0038	55793.3^d	441.8426 ± 0.0024
55491.5^c	441.8263 ± 0.0043	55813.6^d	441.8833 ± 0.0048
55505.8^c	441.8235 ± 0.0037	55827.3^d	441.8872 ± 0.0048
55520.5^c	441.8227 ± 0.0040	55848.7^d	441.9046 ± 0.0022
55534.6^c	441.8278 ± 0.0040	55869.8^d	441.9023 ± 0.0051
55548.6^c	441.7993 ± 0.0041	55884.0^d	441.9199 ± 0.0042
55570.5^c	441.7994 ± 0.0019	55897.9^d	441.8964 ± 0.0053
55585.8^c	441.8172 ± 0.0834	55918.0^d	441.9348 ± 0.0047
55599.7^d	441.8001 ± 0.0025		

The pulse periods were presented before by [a] İnam et al. 2009a & Şahiner 2009 [b] Şahiner et al. (2011) [c] Şahiner et al. (2012a) [d] Şahiner et al. (2012b). Stars indicate measurements from *INTEGRAL* observations.

2.3.3 Torque Noise Strength

The changes in spin frequencies of pulsars are related with the external and internal torques exerted on the star. In an accreting system, the external torque is supplied by the angular momentum content of the accreting matter (Pringle & Rees 1972, Lamb et al. 1973). In addition, internal torque originates from the coupling between the crust and the superfluid interior of the neutron star (Lamb et al. 1978a, b). The net torque that changes the angular velocity of the neutron star is not expected to be smooth. Observed pulse period variations are a measure of the torque fluctuations for the system. Even if the pulse arrival times could be represented with high order polynomials, a random fluctuation remains in the residuals generally. These irregularities in arrival times are often referred as 'timing noise'.

A statistical analysis of the noise elements (Boynton et al. 1972, Cordes 1980, Deeter 1984) showed that the timing noise might arise from 'random walk' processes (white noise). Boynton et al. (1972) proposed three simple models for random walk in; (1) phase ϕ (2) frequency ν and (3) frequency derivative $\dot{\nu}$, which are r^{th} order ($r = 1, 2, 3$) time integral of the noise time series. For a time span of T, the relation between the variance of the angular velocity (Ω) and the noise strength S_r is supposed to be as follows;

$$< \Delta\Omega^2 > \propto \ S_r \ T^{2r-1} \tag{2.5}$$

The factor for this proportionality depends on the degree of the polynomial (m) removed to obtain the mean-square residuals and it is determined either by Monte Carlo Simulations (Cordes 1980) or mathematical evaluation (Deeter 1984). In terms of 'analysis frequency' $f = \frac{1}{T}$, S_r is related to the power density by,

$$P_\Omega = S_r \ (2\pi f)^{-2r} \tag{2.6}$$

Carrying on the analysis on shorter time scales such as $\frac{T}{n}$ (n is a positive integer), the analysis frequencies $f_n = \frac{n}{T}$ and corresponding noise strength values form the power density spectrum of the source.

After the removal of the fifth order polynomial from the arrival times of 4U
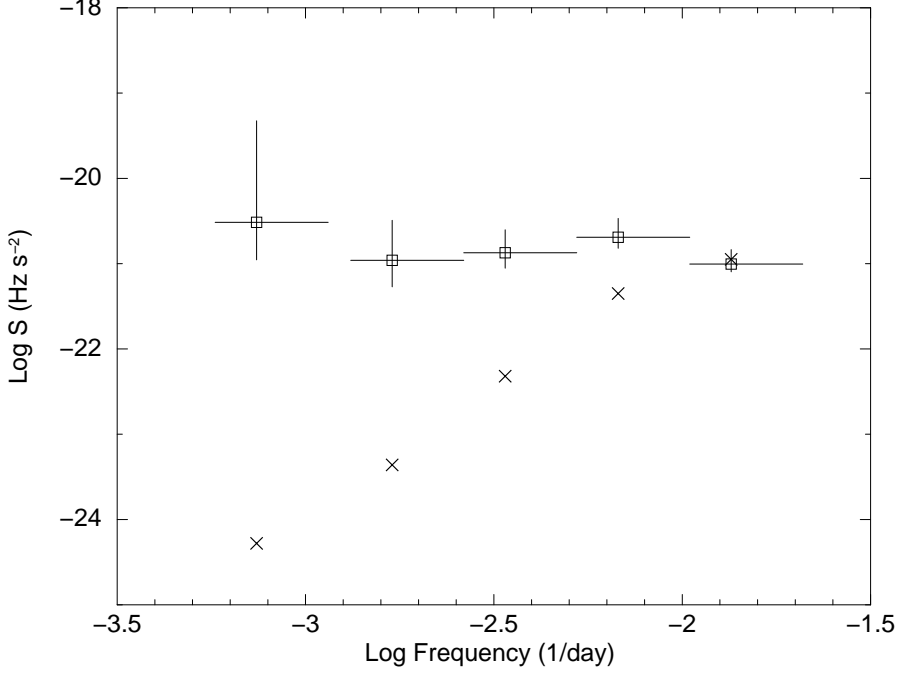
Figure 2.7: Power density of spin frequency derivatives of 4U 1907+09. The power due to measurement noise is subtracted from the estimates and shown independently by the cross symbols.

1907+09, the fluctuation of residuals is evident in Figure 2.5. Since the physical meaning of higher order derivatives is abstract, we derived the noise strength for a cubic polynomial as if higher orders are a part of the noise processes. We construct the power density spectrum in order to investigate the small changes in pulse frequency derivatives (see Fig. 2.6). The polynomial estimator method (Deeter 1984) is used for this purpose.

The power density estimator $P_{\dot{\nu}}(f)$ is defined as

$$\int_0^\infty P_{\dot{\nu}}(f)\, df = < (\dot{\nu} - <\dot{\nu}>)^2 > \tag{2.7}$$

where $<\dot{\nu}>$ is the mean of pulse frequency derivatives for analysis frequency f. The square root of the integrated power for an analysis frequency gives the r.m.s amplitude of variations in $\dot{\nu}$ during the sampling time. The pulse arrival times of 4U 1907+09 are simulated to have a unit white noise strength ($P_{\dot{\nu}}(f) = 1$) and a third order polynomial is used to fit the time series. Then, the power estimate for the time interval of interest is calculated by dividing the square of the cubic

34

term to the value from simulations. Same analysis is repeated for shorter time scales such as $\frac{T}{n}$ to construct the power density spectrum.

The results from this analysis is plotted in Figure 2.7 over logarithmic analysis frequencies. The slope of the power density spectrum between analysis frequencies $1/1300$ and $1/75$ d^{-1} is flat. The mean value for the noise strength is 1.27×10^{-21} Hz s^{-2}. The noise estimates are also calculated using a quadratic polynomial for comparison. Results of the quadratic and the cubic are found to be consistent with each other. Flat power spectrum is an indication of white noise in the pulse frequency derivatives, therefore the pulse frequency fluctuations of 4U 1907+09 are consistent with the random walk model.

In studies of wind-fed binary systems such as Vela X–1, 4U 1538–52 and GX 301–2 (Deeter 1981, Deeter et al. 1989, Bildsten et al. 1997), the power density spectra are observed to be flat with noise strength ranging from 10^{-20} to 10^{-18} Hz s^{-2}. White torque noise is thought to be originating from rotationally altering transient accretion flow due to accretion from an inhomogeneous stellar wind. The time scale of these alternations is simulated to be at the order of hours (Taam et al 1988). Bildsten et al. (1997) also found that the noise of two disk-fed LMXB systems, Her X–1 and 4U 1626–67, are also consistent with the random walk model, with noise strength ranging from 10^{-21} to 10^{-18} Hz s^{-2}. For disk-fed HMXBs such as Cen X–3, GX 1+4 and OAO 1657–415; it is found that the noise strength varies from 10^{-15} to 10^{-18} Hz s^{-2} showing red noise in pulse frequency derivatives (Bildsten et al. 1997). In disk-fed systems, less noise in short time scales may imply that the accretion is dominated by the disk, whereas on longer time scales there is excessive noise.

2.4 Spectral Analysis

2.4.1 Orbital Phase Resolved Spectra with *RXTE*–PCA

The spectral analysis of *RXTE*–PCA observations of 4U 1907+09 are done with the software `XSPEC v.12.6.0`. Selected energy range for the analysis is from 3 to 25 keV. A systematic error of 2 per cent is applied to data. The basic background

estimation is carried on with the supplied PCA background models. However the source is near the Galactic Ridge and a supernova remnant, and needed additional background estimations since *RXTE* spectra are affected by sources in the FOV. The count rates of the dipping episodes of 4U 1907+09, are observed to be consistent with count rates from Galactic Ridge observations (In't Zand et al. 1997, Roberts et al. 2001). Furthermore, the spectra from the dipping times are found to be consistent with spectra from the diffuse emission from the Galactic Ridge (Valinia & Marshall 1998) plus a 6.4 keV Gaussian required for the strong *Fe* emission from the supernova W49B (Miceli et al. 2006). In the view of these facts, an overall dipping state spectrum for each set of data given in Table 2.1 is constructed to be used as additional background during the analysis of individual spectra from the corresponding set [1]. The background produced from the PCA estimator models are directly subtracted from source spectra using `MATHPHA`. The resultant file is used as the source spectrum, whereas dipping state spectrum is given as background in `XPSEC` [2].

Since *RXTE* observations of 4U 1907+09 are maintained in every 15 days and the orbital period of the system is ~ 8.4 days, each observation coincide with a different phase of the binary orbit. Observations, covering a variety of phases, give us the opportunity to study the orbital variations in the spectral properties of the system. Individual *RXTE*–PCA spectra of each non-dip observation are fitted with a model that consist of an absorbed power law with high energy cutoff and the fundamental CRSF ~ 18.9 keV of the source. The cyclotron absorption model `cyclabs` is preferred for the fits (Mihara et al. 1990 and Makishima et al. 1990). The cyclotron line energy is fixed, because individual observations have low quality spectra due to short exposures (~ 2 ks). The mean of line depth and line width are found as 0.4 keV and 1.7 keV respectively. These values are in agreement (within 1 σ uncertainty) with previous studies of the cyclotron feature (Mihara 1995, Cusumano et al. 1998 and Makishima et al. 1999). The *Fe* emission line at 6.4 keV previously reported in spectra from more sensitive instruments (Rivers et al. 2010), could not be resolved in single observation

---

[1] A single dipping background is not used for all sets, since background statistics might have changed during the 4.5 years.

[2] Model background estimates are also subtracted from the dipping source spectra during the production of background file.

36

PCA spectra after the subtraction of the Galactic Ridge emission. However, we confirm that *Fe* line component is required in the fit of a summed spectrum from a set of observations (Şahiner 2009).

Spectral results obtained from individual observations of similar orbital phases are statistically averaged to represent 20 phase bins of one orbit. In Figure 2.8, variation of parameters along with the orbital profile folded from *RXTE*–ASM count rate are given. In the first panel, ASM profile shows the large primary maximum corresponding to periastron passage (indicated with vertical dashed lines). 3–25 keV unabsorbed flux values of 4U 1907+09 are measured to be in between $1.37 - 11.04 \times 10^{-10}$ erg cm^{-2} s^{-1} for individual measurements. When the results are binned in orbital phases, the resulting flux variation (see second panel of Fig 2.8) hardly resembles the ASM profile of the source. This is mainly because of the highly variable nature of 4U 1907+09 independent of the orbital phase. For example the maximum flux measurement is obtained from an observation corresponding to phase 0.4. This type variability is commonly observed in other persistent X-ray pulsars accreting in wind-fed systems, such as Vela X–1 and GX 301–2 etc. As the pulsar orbits around its companion supergiant star, it passes through higher density regions of the companion's wind. As more matter is accreted during these passages, the X-ray flux of the source increases.

Orbital variability of Hydrogen column density (n$_H$) is given in the third panel of Figure 2.8. n$_H$ stands in its standard value of $\sim 2 \times 10^{22}$ cm^{-2} in about half of the orbital phases. The maximum measurements of n$_H$, above 10×10^{22} cm^{-2}, are always measured for orbital phases between $0.8 - 0.9$. Previously reported maximum value for n$_H$ was $\sim 9 \times 10^{22}$ cm^{-2} (In't Zand et al. 1997). Nine measurements in this work exceed this value and the maximum is measured as $\sim 15.5 \times 10^{22}$ cm^{-2}. Averaging the results for similar phases clarifies the trend in n$_H$. The column density reaches to its maximum after the periastron and it slowly decreases until the apastron phases. During the apastron and until the next periastron n$_H$ remains low. A similar variation in the column density was observed previously by Roberts el at. (2001).
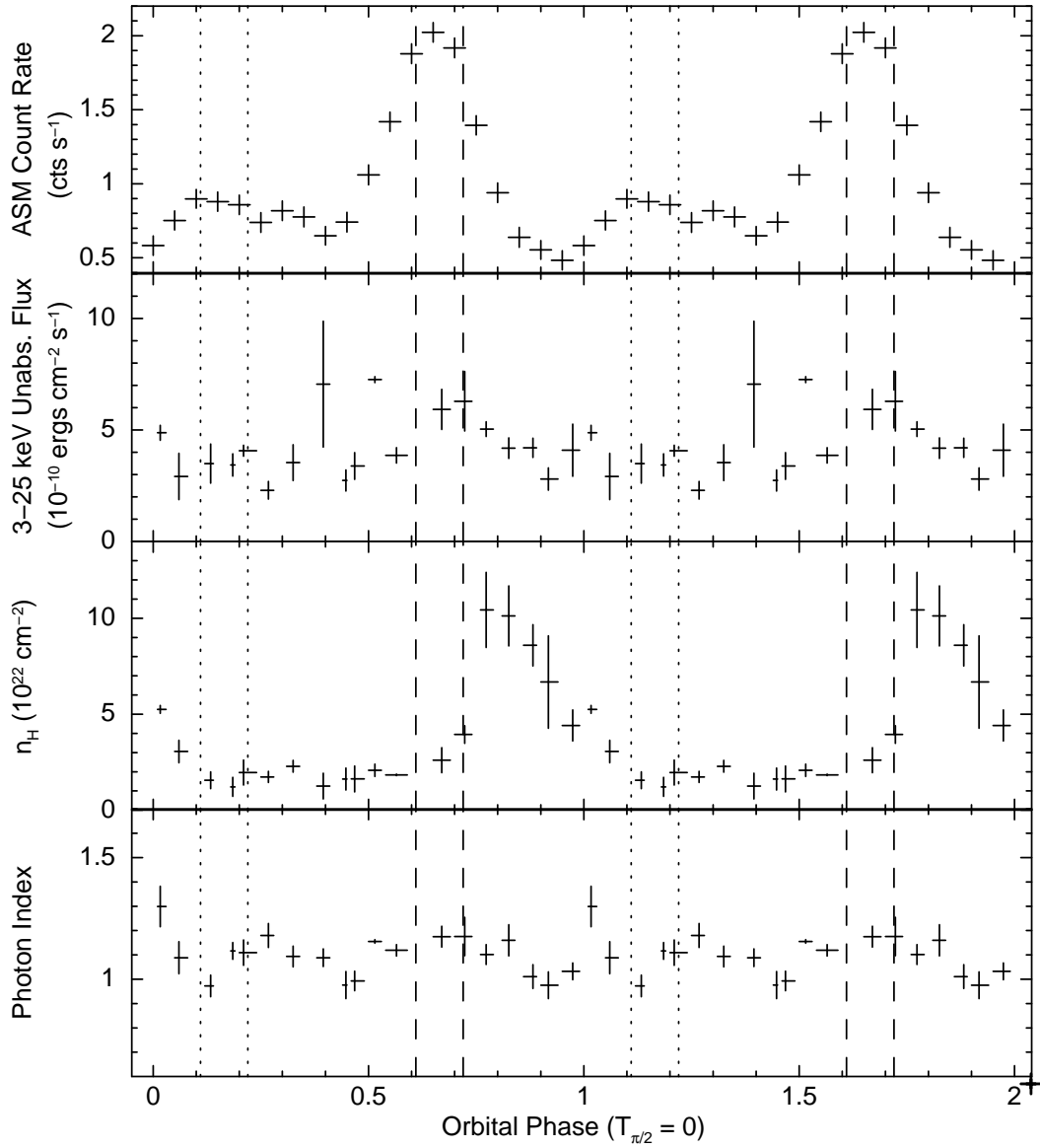
Figure 2.8: Orbital variations in the spectral parameters of 4U 1907+09. The data points are repeated for a cycle for clarity. From top to bottom; orbital profile folded from *RXTE*–ASM count rate, unabsorbed flux measured from 3–25 keV spectra, Hydrogen column density and photon index plotted over orbital phase presented with 20 bins respectively. All uncertainties are calculated at 90% confidence level. The vertical dashed lines correspond to time of periastron passage,whereas dotted lines correspond to time of apastron passage within 1 σ.

High variability in column density is also a characteristic of some other accretion powered pulsars (e.g. Vela X–1 (Haberl & White 1990)). Variations may even range up to $\sim 10^{23} - 10^{24}$ cm^{-2}. The Hydrogen density in the accretion column is a probe to the distribution of the accreting material. Enhanced accretion due to increased matter causes higher absorption in the column. High absorption at periastron passages or eclipse ingresses is generally linked to the existence of a stream of matter trailing the pulsar (Haberl et al. 1989). Leahy (2001) and Kostka & Leahy (2010) modelled the n_H variation in the case of 4U 1907+09 and found that, along with a spherical accretion from the wind there should exist an equatorially enhanced dense spiral stream of gas around the companion in order to explain the observed absorption profile of the source. Leahy & Kostka (2008) also studied on GX 301–2 and found evidence to support the idea that the dynamic effects of high eccentricity orbits of X-ray pulsars are likely to form similar stream of matter from the stellar wind of the companion (Stevens 1988). For 4U 1907+09, the conservation of high absorption until apastron implies that, after the trailing stream catches the neutron star the star remains in the stream of matter until apastron.

Although the power law index values of individual observations are measured to be in between $0.9 - 1.4$, when the results are binned for similar orbital phases no significant variation is observed (see bottom panel of Fig. 2.8). The mean value of the spectral index is ~ 1.1. It seems to be slightly increased during the apogee and perigee of the orbit, where the X-ray flux increases. The high energy cutoff of the power law is constant through the orbit. The mean of the cutoff energy is found to be ~ 12.7 keV, whereas the exponential folding energy is ~ 9.6 keV. CRSF parameters left free (i.e. depth and width) could only be estimated with high uncertainties, therefore no variation could be resolved.

2.4.2   X-ray Flux Dependence of Spectral Parameters

In order to search for the possible correlation of spectral parameters with the X-ray flux, spectral results presented in Section 2.4.1 are statistically averaged to be represented by 9 bins for different X-ray flux ranges. In other words, the
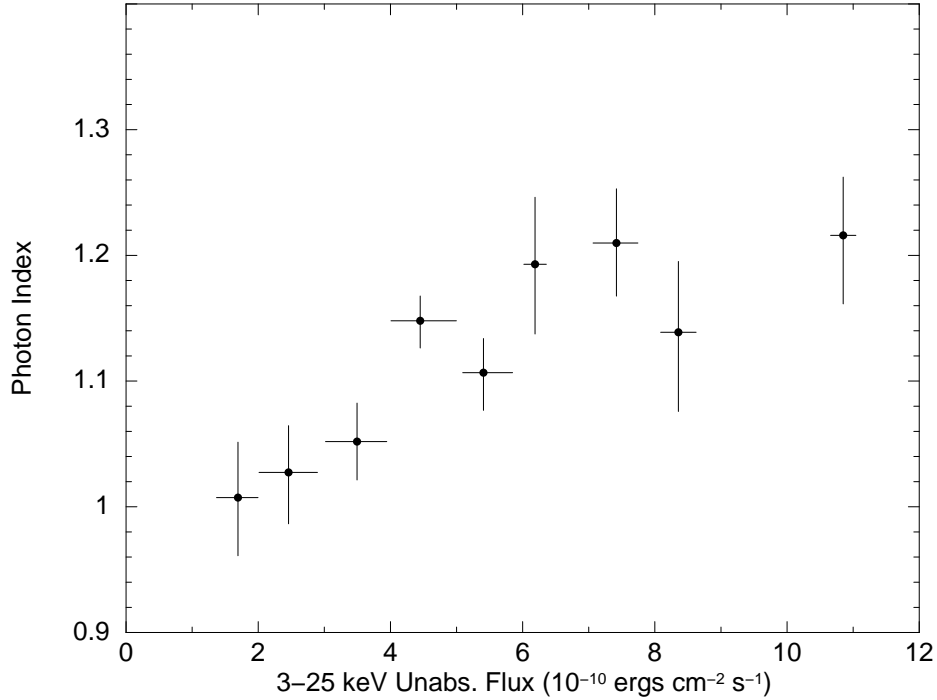
Figure 2.9: Variation of power law index with X-ray flux of 4U 1907+09.

set of spectral parameters from individual observations which have similar flux measurements, are averaged together for each bin. The flux ranges of each bin are represented as x-axis error bars in Figure 2.9. Although the procedure is applied for all free parameters, only correlation is found for the photon index. The correlation of power law index and 3–25 keV unabsorbed flux is plotted in Figure 2.9, in which the spectral index is increasing with increasing flux.

Increasing spectral index is an indication of softening in X-ray spectra. In the case of 4U 1907+09, the spectral softening is observed as the X-ray flux of the source increases. Other accretion powered pulsars for which a similar softening is observed are V0332+53 (Klochkov et al. 2011), 4U 0115+63 (Klochkov et al. 2011), 4U 1626–67 (Jain et al. 2010) and Vela X–1 (Fürst et al. 2009). Although there are sources that show similar variation, an opposite correlation (i.e. spectral hardening with increasing X-rat flux) is more commonly observed in sources such as Her X–1 (Kolochkov et al. 2011), Swift J1626.6–5156 (İçdem et al. 2011), XMMU J054134.7–682550 (İnam et al. 2009b), 2S 1417–62 (İnam et al. 2004) and SAX J2103.5+4545 (Baykal et al. 2007). Any type of correlation

(positive of negative) between spectral index and flux are generally considered to be an indication of variation in accretion rates due to inhomogeneities of the accreting matter.

2.5   Dipping States and Pulse-to-pulse Variability

As 4U 1907+09 is a source well known to show irregular dipping activity, during which count rates fall dramatically and pulsations disappear (In't Zand et al. 1997); *RXTE*–PCA light curves of the source are extensively examined to distinguish the irregularities due to ingress and egress to dipping episodes. Although single observations only cover about 2 ks of time, a variety of pulse-to-pulse variations are also detected.

Ten sample light curves given in Figure 2.10 are 22 s binned in order to have about 20 bins per pulse. The x-axes of the light curves are converted pulse phase. Let us have a look at the panels one by one. Panel (a) is an example of a regular ingress to dipping,in which the source goes in a sudden reduction in intensity after two standard pulses. In general, a variation in pulsed intensity is observed in most of the ingresses, like in the one on panel (b). Three pulses are observed to lose pulse-to-pulse intensity before a dipping episode that only lasts for one pulse period duration. Similar intensity variations are also observed for egresses, e.g. on panel (c) the pulsed intensity of the source increases pulse-to-pulse as it comes out of another dip.

Beyond these regular examples, there are two extreme events one of which is given on panel (d). In this light curve source is first observed in a dipping episode, which is followed by an X-ray flare reaching to ~ 600 cts s^{-1} and after two pulse cycles of smooth decrease another dip starts. The sudden interruption of a dip with an X-ray flare had sparkled the comparison of 4U 1907+09 with SFXTs (Doroshenko et al. 2012). These authors furnish the idea that a flare within a dip resembles the flares of SFXTs and can be explained by the "gated accretion" scenario proposed for SFXTs (Bozzo et al 2008).

The double-peaked pulse profile of 4U 1907+09 is often conserved in time, how-
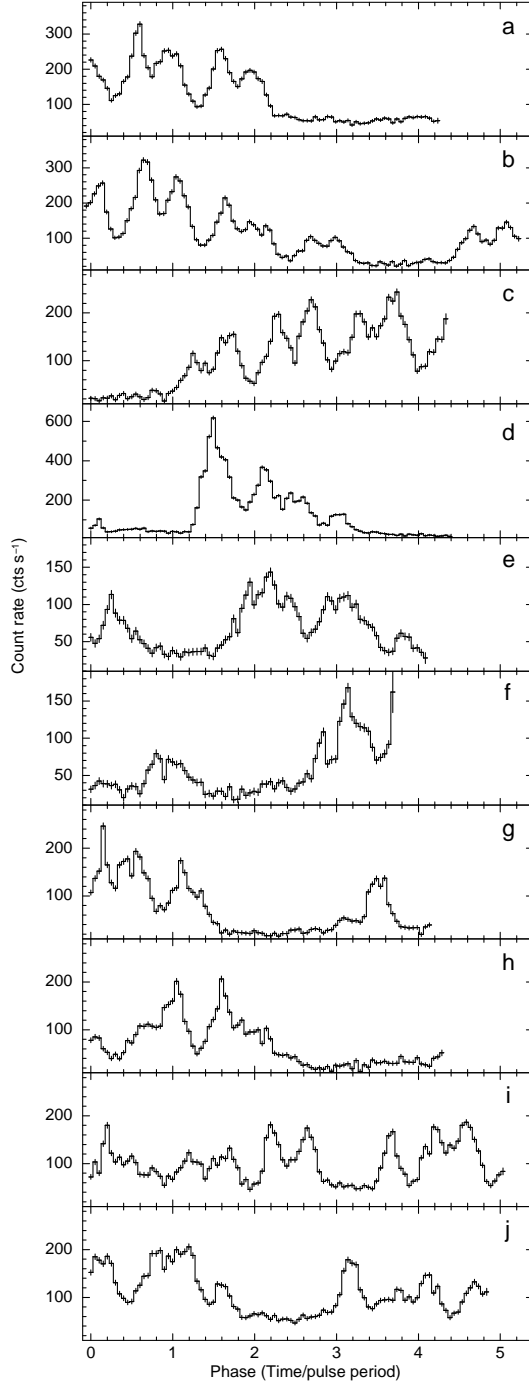
Figure 2.10: A set of examples for pulse-to-pulse variation and irregularities due to dipping activity. The time column of 22 s binned light curves are converted to phases (or time/pulse period) for arbitrary observation epochs. Explanations to each panel are given in Section 2.5. Observation IDs of panels from top to bottom are a:94036-01-19-00, b:96366-02-01-00, c:94036-01-05-00, d:94036-01-23-00, e:94036-01-13-00, f:93036-01-20-00, g:94036-01-03-00, h:93036-01-34-00, i:93036-01-38-00 and j:95350-01-06-00.

ever in low count rate observations there is a possibility of disruption of the pulse shape. For example in panel (e) after a dip that ends in one pulse period duration, the shape of the pulse is transformed into a single broad peak. The shape of the faint pulse at the onset of panel (f) light curve sharpens after the dip, where the double peaks are detached. The count rates at the beginning of panel (f) are comparable to dipping episodes, though faint pulsations are observed. Similar situations detected occasionally, are named as "unsuccessful dips" by In't Zand et al. (1997).

Other variations in pulse shape due to dipping ingress and egress are missing peaks of the pulse. Before and after the 1.5 pulse long dip in panel (g), the pulse is single-peaked. In panel (h) two single-peaked pulses are observed before the dip that starts on phase 2.6. It should be noted that the peaking pole is different for these two pulses. A very rare event is demonstrated in panel (i); here one peak of a pulse totally disappears during a period of time the source pulsates in its regular manner. As we suppose this is due to a dip, the intensity drop in phases between 2.9 and 3.4 is recorded to be the shortest dip of 4U 1907+09 with only half a period duration. In panel (j) a dip between phases 1.8 and 2.8 is due to similar disappearance of pulse peaks. This time the opposite peaks of two consecutive pulses disappear, resulting in a longer dip.

There are no known regularities in time or orbital phase in the occurrence of the dipping episodes of 4U 1907+09. Since $RXTE$–PCA observations of the source cover a variety of orbital phases, an attempt to investigate the orbital distribution of the dipping episodes is maintained for the first time. About half of the pointings include a dip state (either all of the exposure or a part of it). In terms of total exposure, 24 per cent of the total observing time is spent on dipping episodes of the source. In order to find the orbital coverage of dipping episodes, the total exposure of each orbital phase (with resolution of 0.1 phases) and the dipping episode exposures matching to that phase are calculated to evaluate the percentage of dipping states. Resulting dip exposure percentages are plotted on orbital phase in the middle panel of Figure 2.11. Top panel of this figure is the orbital profile from $RXTE$–ASM, where as the bottom panel is a 10 bin version of n_H variation over the orbit measured from non-dip observations
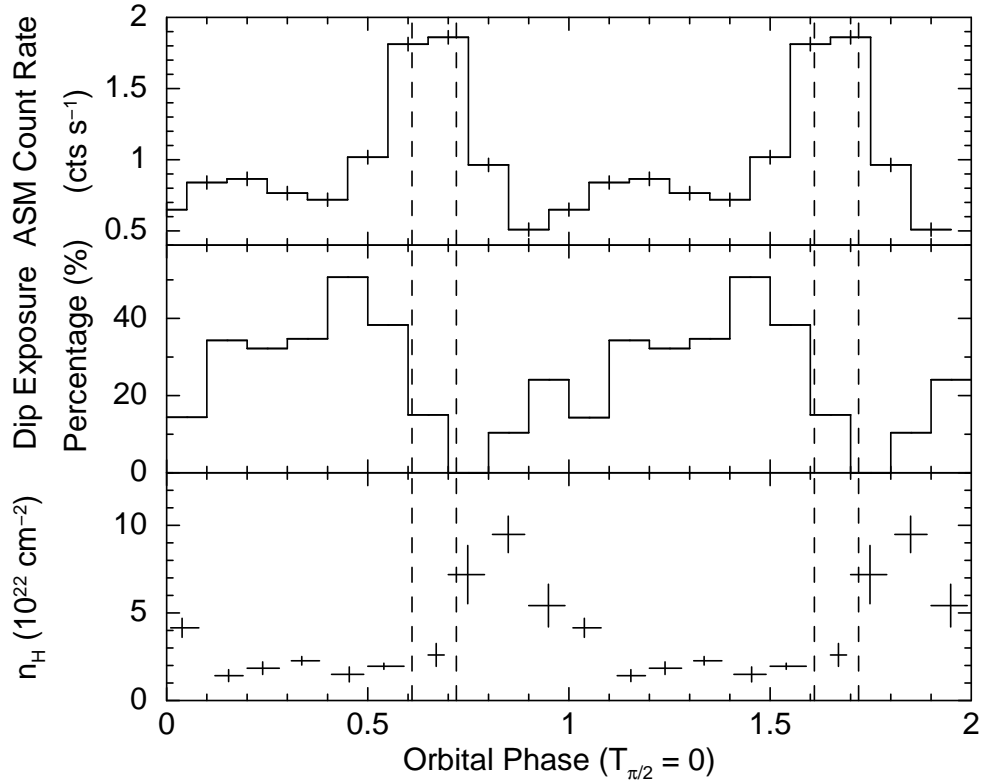
Figure 2.11: The orbital profile from *RXTE*–ASM(top panel), the percentage of dip exposure times to the total exposure through the binary orbit (middle panel) and the n_H variation over the orbit (bottom panel). The data points are repeated for a cycle for clarity. The vertical dashed lines represent the time of periastron passage within 1 σ. Probability of observing a dipping state is lower during periastron passage and afterwards (between orbital phases 0.6 and 1.1), where n_H measurements from non-dip observations remain high.
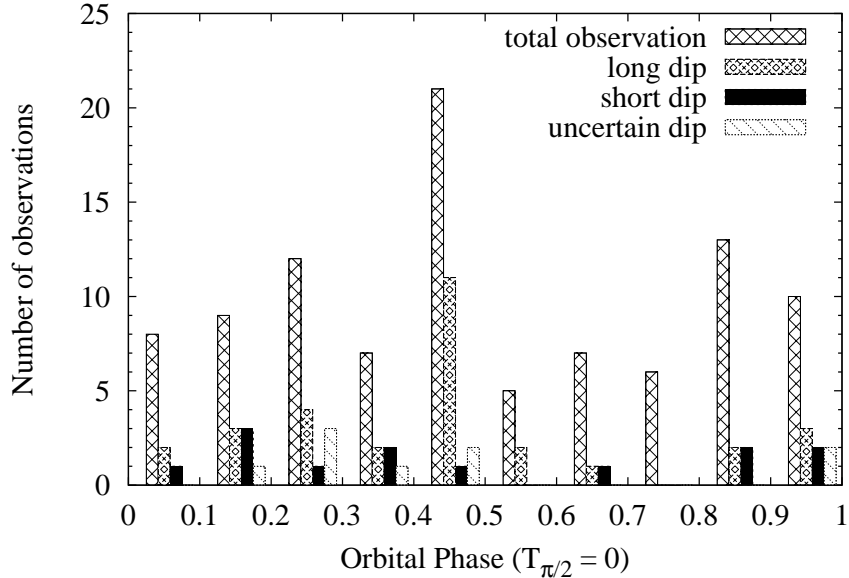
Figure 2.12: Orbital phase distribution of total and dipping state observations. Long dips are longer than 1 ks whereas short dips are shorter than 1 ks. Uncertain dips are the dips that cannot be verified as long or short, because of the location of the dip in the light curve (at the beginning or end of the observation).

(see third panel of Figure 2.8 for 20 bin version).

Starting from the periastron time of the orbit, the occurrence of dips is lower until the apastron (see Figure 2.11). The only phase with no dipping observed is between phases 0.7 and 0.8. This phase corresponds to the times when n_H measurements from non-dip observations increases to its maximum. The lower probability of dipping phases (between 0.8–1.1) also match up with the times of high n_H. 4U 1907+09 frequently experiences dipping states between phases 0.1 and 0.6, when n_H remain in its base value. Nevertheless, it should be emphasized that n_H values are measured from non-dip observations, since spectral study of dipping states is not possible with *RXTE*. The possibility that an observation coincides to a dipping state is maximum for orbital phases 0.4–0.5. In terms of number of observations (see Figure 2.12) these orbital phases are the ones that observed most and about half of the observing time correspond to a dip.

The duration of the dipping activity were previously reported to be between few minutes to 1.5 hours (In't Zand et al. 1997). Although the short exposure

time ($\sim$ 2 ks) of *RXTE* observations apply a limit on the dipping durations we witness, we try to distinguish the long and short dips and work out their distribution along the orbital phase. We define long dips to be longer than 1 ks and short dips to be shorter than 1 ks. Dips that could not be verified as long or short due to the location of the dip in the light curve (at the beginning or end of an observation), are categorized as uncertain dips. We count the number of dips in each orbital phase and draw an histogram of number of observations (see Figure 2.12). Both short and long dips are observed in a variety of phases. However, the histogram shows that most of the long dips are observed in phases 0.4–0.5, where the dip exposure percentage peaks in Figure 2.11. Short dips seem to be exceptional events for this phase; whereas the numbers of long and short dips are mostly similar for other orbital phases. The shortest dip we observe have a duration about half of the pulse period ($\sim$ 220 s, see panel (i) of Figure 2.10), where short dips generally survive for about one pulse period.

2.6   Summary and Discussion

In this chapter, 4U 1907+09 is studied extensively with the data of *INTEGRAL* and *RXTE* observatories. IBIS–ISGRI light curve between 2005 October and 2007 November is used to measure pulse periods of the source. PCA observations covering a 4.5 year of time (2007 June – 2011 December) allowed us to work on the orbital variations in the properties of the source, along with the long term timing solution.

The period measurements of 4U 1907+09 are used to update the pulse period history of the source (see Figure 2.6). *INTEGRAL* data covering the gap in the period history, demonstrates the final stages of the spin-up episode of the pulsar, which was detected by Fritz et al (2006). The timing solution obtained from the *RXTE* data between MJD 54280 and 55600 shows that the source had returned to its spin-down trend with a rate of $-3.672(1) \times 10^{-14}$ Hz s^{-1}, which is similar to the historical spin-down rate of 4U 1907+09.

In *RXTE* measurements, small fluctuations of the pulse period have come in

view for the first time. In order to investigate these small changes the power density spectrum of 4U 1907+09 is constructed (see Figure 2.7). The noise strength of 1.27×10^{-21} Hz s^{-2} is evaluated to be constant since the slope in the power density spectrum is found as flat between $1/1300$ and $1/75$ d^{-1}. Therefore the pulse period fluctuations of 4U 1907+09 are successfully explained by the random walk model, which implies the existence of white noise in the pulse frequency derivatives. This implication leads us to suppose that there may be an accretion disk formation in the system, which contributes to the white noise on short time scales.

Spectral results from of $RXTE$–PCA observations, verified the orbital variation of Hydrogen column density (n$_H$). A base value of 2×10^{22} cm^{-2} increases significantly just after the periastron passage (see Figure 2.8). The maximum n$_H$ is measured to be about 15.5×10^{22} cm^{-2}. As the accreting matter accumulates in the accretion column, absorption increases. Hence the supply of matter enhances during the periastron passage. High absorption being conserved until apastron, gives the scheme of a trailing stream of gas in which the neutron star lingers inside it. Therefore the orbital variation of n$_H$ indicates a wind structure, that contains both an equatorially located spiral dense material around the companion and spherical wind clumps.

Another result of the spectral analysis is the correlation of the power law index with the source flux. As the X-ray flux of 4U 1907+09 increases, the photon index also increases indicating the governance of soft photons in the X-ray spectra (see Figure 2.9). The X-ray flux variations are related to accretion rate variations. Increased material reaching to the thermal mound of the neutron star might result in the enhancement of soft photon production.

Frequent observations with $RXTE$ for 4.5 years produce a good coverage of many dipping states of 4U 1907+09. Dipping light curves are screened to focus on pulse-to-pulse irregularities due to ingress and egress from the dip (see Figure 2.10). We find that dipping episodes may be exceptionally as short as half of the pulse period (~ 220 s). Although the exposure time of single observations do not allow to determine an upper limit to the duration of dips, generally the dipping

in the light curves take up all the observation time of the single observation (~ 2 ks). The orbital dependence of the dipping incidences is investigated for the first time (see Figure 2.11). Obviously, the probability of dipping is less in certain orbital phases, and high in others. A sharp decrease in the probability during the periastron continues until the apastron. Moreover 4U 1907+09 frequently enters to dipping states during the second part of the orbit, that is after apastron until the next periastron. When this variation is compared with the column density measurements from non-dip observations, a relation is evident.

Among X-ray binaries the dipping states are very common in low mass systems (Balman 2009 and references therein). The dipping states in these systems are supposed to be due to an obscuring material located between the line of sight and the X-ray source (White & Swank 1982). The properties of the system are expected to change strongly during the dips in LMXBs. Generally, the spectrum hardens due the absorption of soft X-ray by the obscuring material (Church et al. 1997). Therefore spectra of dipping times give clues about the behavior of the absorber covering the source partially. A neutral absorber scenario fails to satisfactorily explain the dipping activities rarely seen in HMXB systems. Though there are very few examples of dipping HMXBs. A similar source to 4U 1907+09, Vela X–1 does not show any transitions in the X-ray spectral characteristics during the dipping episodes (Kreykenbohm et al. 2008). In this work of 4U 1907+09, we could not analyze the spectra of dips because $RXTE$ is not an appropriate instrument as the diffuse emission from the Galactic Ridge dominates PCA spectra of dipping times. However, there are other studies which verify that the dipping state spectra of the source lack any sign of a partial covering absorber (In't Zand et al. 1998, Roberts et al. 2001, Rivers et al. 2010). Another HMXB that exhibits dipping activity is GX 301–2. Göğüş et al. (2011) investigated pulse-to-pulse spectral variation during a dip of GX 301–2 and found an increase in the photon index before and during the dip. Furthermore, Fürst et al. (2011) did not find any variation in column density during the low flux episodes of GX 301–2. The findings in both of these studies indicate that the scenario to explain the dips of GX 301–2 is not obscuration of the X-ray source.

The dips of Vela X−1 are mainly explained by cessation of accretion due to insufficient amount of matter (Kreykenbohm et al. 2008). When the magnetic pressure dominates the material pressure, the material cannot reach to co-rotation radius and accretion is inhibited by a centrifugal barrier resulting in a 'propeller' effect (Lamb et al. 1973). As soon as the accretion stops the pulsations in X-rays are no longer observable. The limiting luminosity to turn on/off the propeller is derived from the condition that the co-rotation radius is equal to magnetospheric radius (Illarionov & Sunyaev 1975). Kreykenbohm et al. (2008) gives the simplified equation for propeller flux as;

$$
F_x = 4.3 \times 10^{-7} \, \text{erg cm}^{-2} \, \text{s}^{-1}
$$
$$
\times \left(\frac{B}{10^{12} \, \text{G}} \right)^{2} \left(\frac{P}{1 \, \text{s}} \right)^{-7/3} \left(\frac{d}{1 \, \text{kpc}} \right)^{-2} \left(\frac{M}{1.4 \, M_\odot} \right)^{-2/3} \tag{2.8}
$$

where B is the surface magnetic field strength, P is the pulse period, F_x is the X-ray flux, d is the distance and M is the mass of the pulsar. For 4U 1907+09 using the values, $B = 2.1 \times 10^{12}$ G, $P = 441.2$ s, $d = 5$ kpc the limiting X-ray flux that the propeller effect would turn on/off is found to be 5.2×10^{-14} erg cm^{-2} s^{-1} which correspond to a luminosity of 1.5×10^{32} erg/s. This luminosity is 3 to 4 orders lower than the luminosity of 4U 1907+09 in regular accretion mode, which is $10^{35} - 10^{36}$ erg/s.

The mechanism that causes the calculated drop in the luminosity is accused to be accretion from strongly structured inhomogeneous clumpy wind of the companion star (Kreykenbohm et al. 2008 and references therein). This type of wind structure contains different regions with variety of densities. Models calculated the magnitude change of the density in the wind clumps could be as high as $10^{3} - 10^{5}$ (Runacres & Owocki 2005; Walter & Zurita-Heras 2007). Therefore, a passage from a low density region results in a sudden decrease in mass accretion rate at the same order as the density drops. The X-ray luminosity also drops at the same order, since it depends on the mass accretion rate. As the accreting matter lessens the magnetospheric radius increases such that propeller effect comes into work and accretions stops. This scenario naturally explains the disappearance of pulsations during the dipping states and it is also suggested for similar dipping activity in accretion powered pulsars such as GX 1+4 and

GRO J1744–28 (Cui 1997), Vela X–1 (Kreykenbohm et al. 2008) and GX 301–2 (Fürst et al. 2011).

The orbital variation of n_H is an indication of the structured wind of the companion. While the X-ray flux of the source increases due to the enhanced accretion at periastron, n_H increases after the periastron. Denser matter of accretion consequently lessens the occurrence of the dips. It should be kept in mind that detailed timing analysis of orbital flaring times previously revealed transient QPO features around 0.055 Hz (In't Zand et al. 1998) and 0.069 Hz (Mukerjee et al. 2001). Since QPOs detected in accretion powered pulsars are related to formation of transient accretion discs, the times when dip states are less are candidate times in which the dominant accretion mechanism is a disc. When the occurrence of the dips increases between phases 0.1 and 0.6 (see Figure 2.11), the disk might be running out of material and the variable density clumpy wind structures taking the control over as the dominant accretion mechanism. The lower density clumps may lead the system to enter temporary propeller states that are identified with the dipping states. This scenario composed of a combination of wind and disk mechanisms at work for different phases of the orbit can also explain the random walk in pulse frequency.

The latest study on the dipping episodes of 4U 1907+09 observed during 2006 with *Suzaku*, measured only one order difference in 'on' and 'off' state flux values of the source (Doroshenko et al. 2012). Doroshenko et al. (2012) measured the dip luminosity to be at the order of 10^{34} erg/s , which is far more greater than the luminosity for the propeller mechanism to be at work. Moreover, these authors reported that the folded light curve of the 'off' state produces a similar pulse profile as in the 'on' state of the source. The preservation of the pulsed emission during the dipping state implies that the accretion is maintained. It is discussed that the process responsible for the penetration of matter into the magnetosphere might be changing from Rayleigh–Taylor instability to Kelvin–Helmholtz instability as the source switches off (Burnard et al. 1983, Bozzo et al. 2008, Doroshenko et al. 2011). Connections to SFXT systems are considered for both Vela X–1 (Kreykenbohm et al. 2008) and 4U 1907+09 (Doroshenko et al. 2012). SFXTs have very short duration of outbursts in between long

quiescence episodes (Negueruela et al. 2008, Sidoli 2011), where as the dipping HMXBs act quite the opposite with short duration of 'off' states in between long active phases. The property that discriminates persistent sources that show dipping activity (e.g. Vela X–1 and 4U 1907+09) from SFXTs might be the compactness of the binary resulting in relatively bright 'off' states on the contrary to quiescent times of SFXTs. Therefore the dipping HMXBs could be the missing link between regular persistent HMXBs and SFXTs (Doroshenko et al. 2012).

CHAPTER 3

SWIFT J1729.9–3437

In this chapter, results of the X-ray timing and spectral analysis of the first and the only outburst of SWIFT J1729.9–3437 are given. The outburst is monitored with both *RXTE* and *Swift* from 2010 July 20 to 2010 August 12 (MJD 55397 – MJD 55420). This study is published on MNRAS with the title "*RXTE and Swift observations of SWIFT J1729.9–3437*" (Şahiner et al. 2013).

3.1   Introduction

The X-ray transient SWIFT J1729.9–3437 was discovered on 2010 July 13 with *Swift*–BAT (Markwardt et al. 2010a). Independently, on the next day of its discovery, Galactic centre monitoring program with *RXTE*–PCA also detected a new source at the same coordinates. From then on, pointing observations with both instruments had screened the outburst of the source. Improved *Swift*–XRT position of SWIFT J1729.9–3437 is measured as RA=262.53746, Dec.=–34.61239 (J2000) with $1''.7$ uncertainty (Markwardt et al. 2010b). Markwardt et al. (2010b) also noticed in the first $\sim$1.5 ks *RXTE*–PCA light curve that the source is highly variable and suggested a pulse period of $\sim$530 s. In addition, they modelled the X-ray spectrum of SWIFT J1729.9–3437 with a basic model for X-ray pulsars, which is an absorbed power law with a high energy cut-off.

As an X-ray source showing outbursts and long period pulsations, SWIFT J1729.9–3437 is possibly located in an HMXB system. However, there are no optical or infra-red stars in the X-ray error circle. During the outburst, *Swift*–

UVOT observations of the X-ray position did not detect any source neither (Krimm et al. 2013). The most nearby candidate is a bright 2MASS star $4''.6$ away. According to Krimm et al. (2013) 2MASS 17300946–3436433 could not be the counterpart of SWIFT J1729.9–3437, because it is too far. Moreover they report that, UVOT magnitude of this 2MASS star did not show any variation during the ∼20 days of monitoring. Since the location of SWIFT J1729.9–3437 in the Galaxy is close to the central bulge, its counterpart is probably obscured.

3.2 Observations and Data Reduction

3.2.1 *RXTE*

SWIFT J1729.9–3437 was observed with *RXTE* between 2010 July 20 and 2010 August 8. There are 11 pointing observations with a total exposure of about 42 ks (see Table 3.1). The data of PCA instrument on-board *RXTE* are analysed with the standard tools of `HEASOFT v.6.11`. Only PCU2 top anode layer data is selected in order to increase the spectral quality. The data is filtered to exclude the times of elevation angle $\leq 10°$, offset $\geq 0°.02$ and electron contamination $\geq$ 0.1 for PCU2.

For the overall spectral analysis the data mode considered is the Standard2f, which have 128 channels for 2–60 keV energy range. In addition, pulse phase resolved spectral files are constructed using the tool `FASEBIN Rev.1.8`. The main phase-binned spectral analysis is carried out for the first three observations of SWIFT J1729.9–3437 which are the only ones that have 256 channels Good Xenon event mode data. The events of the remaining observations were recorded in a different data mode (`E_125us_64M_0_1s`), which have 64 spectral channels. `FASEBIN` files are also constructed for `E_125us_64M_0_1s` events in order to generate energy resolved pulse profiles with the tool `FBSSUM`. Background files are extracted with the provided estimator model suitable to observation times, which is `EPOCH 5C`. Spectral response matrices are generated with the tool `PCARSP V.11.7.1`. 3–25 keV spectra are modelled with `XSPEC v.12.7.0`.

For the timing analysis, selected energy range is from 3 to 20 keV. 1 s binned

Table3.1: Log of *RXTE* observations of SWIFT J1729.9–3437.

Observation ID	Mid-Time(MJD)	Exposure (s)
95044-05-01-00	55397.76	1424
95044-05-01-01	55398.72	5776
95044-05-02-00	55400.78	3200
95044-05-02-01	55402.34	2384
95044-05-02-02	55404.63	3200
95044-05-02-03	55406.66	3152
95044-05-03-00	55408.46	6400
95044-05-03-01	55410.61	5328
95044-05-03-02	55413.33	2336
95044-05-03-03	55413.39	2736
95044-05-04-00	55416.43	6432

background subtracted light curves are generated from event mode data, which are Good Xenon or `E_125us_64M_0_1s`. The time column of the light curves are converted to barycentric times using the tool `FXBARY`.

3.2.2 *SWIFT*

Follow-up *Swift*–XRT (X-ray Telescope; Burrows et al. 2005) observations of SWIFT J1729.9–3437 started on 2010 July 20, 7 days after its discovery with *Swift*–BAT (Burst Alert Telescope; Barthelmy et al. 2005) all-sky survey. 11 pointing observations are enrolled until 2010 August 12 with a total exposure of ∼31 ks. A log of these observations are listed in Table 3.2.

The *Swift* satellite (Gehrels et al. 2004) has three instruments on-board, one of which is a focusing X-ray telescope (XRT) that works in soft X-ray band with an energy range 0.2–10 keV. XRT has a FOV with dimensions $23'.6 \times 23'.6$. The spatial resolution of the CCD–22 detector is $18''$. The effective area is 110 cm^2 at 1.5 keV. XRT changes its operation mode, according to the source brightness. Above 140 mCrab, imaging mode operates for highly

Table3.2: Log of *Swift* observations of SWIFT J1729.9–3437.

Observation ID	Start Time (MJD)	Off-axis (′)	Exposure (s)
31767001	55397.62	3.08	2989
31773001	55402.25	2.65	2635
31773002	55404.65	2.88	2986
31773003	55406.13	2.43	2964
31773004	55408.19	2.60	3056
31773005	55409.74	2.77	3114
31773006	55412.48	2.38	3031
31773007	55414.30	1.60	1146
31773008	55416.03	2.21	3390
31773009	55418.30	2.49	2648
31773010	55420.05	2.20	3127

accurate position determination and has no X-ray event recognition. Photon-counting mode is also a 2 dimensional imaging mode along with the full spectral capability and ∼2.5 s time resolution. Windowed timing mode is a 1 dimensional mode with higher time resolution of 1.7 ms and can operate for 1-600 mCrab sources that require high resolution timing. SWIFT J1729.9–3437 is observed in PC mode. Raw event files are cleaned using the pipeline `XRTPIPELINE v.0.12.6` of `XRTDAS v.2.7.0` package. 0–12 grade filtering is applied to the data.

Images, spectral files and light curves are generated by `XSELECT v.2.4b`. In Figure 3.1, the background and source regions are shown on the combined image produced from all XRT observations. A source-free circular region with radius 141″.4 is selected for background. The source region is an annulus with inner radius 11″.8 and outer radius 82″.5. An annular region is often used to correct for the pile-up effect. Pile-up occurs on X-ray CCDs when multiple photons hit the detector at the same place and it affects both flux measurements and spectral characterization. XRT count rates above 0.5 cts/s produce pile-up events. In order to determine the radius of the central region affected by pile-up, one should model the outer wings (> 15″) of the point spread function (PSF) with a King
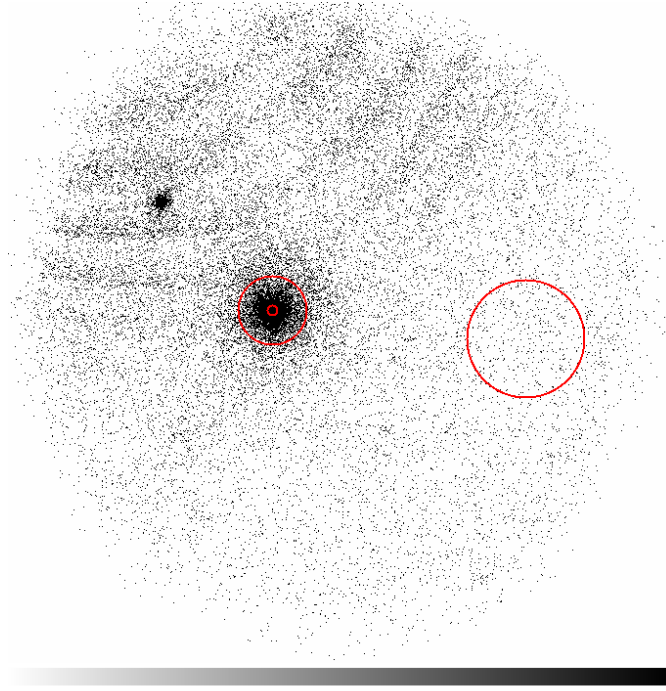
Figure 3.1: Combined *Swift*–XRT image of SWIFT J1729.9–3437. Regions shown are used for extraction of background and source files.

function;

$$PSF(r) = N \times [1 + (\frac{r}{r_c})^2]^{-\beta} \tag{3.1}$$

where, the typical parameters for *Swift* are $r_c \sim 5.8$ and $\beta \sim 1.55$ (Moretti et al. 2005). Then, the inner regions of the observed and nominal PSF are compared and the exclusion radius is determined by the point where the data and the model deviate from each other. The nominal PSF fit and the observed PSF data points for SWIFT J1729.9–3437 are given in Figure 3.2.

XRT spectral files are re-binned to have at least 50 counts per bin using `GRPPHA`. Response file version v013 is used from `CALDB`. Exposure maps are produced by `XRTEXPOMAP v.0.2.7` and they are merged with `XIMAGE`. Merged exposure map is used to create an ancillary response file using the tool `XRTMKARF v.0.5.9`. Resulting 0.3–10 keV spectrum is modeled with `XSPEC`.

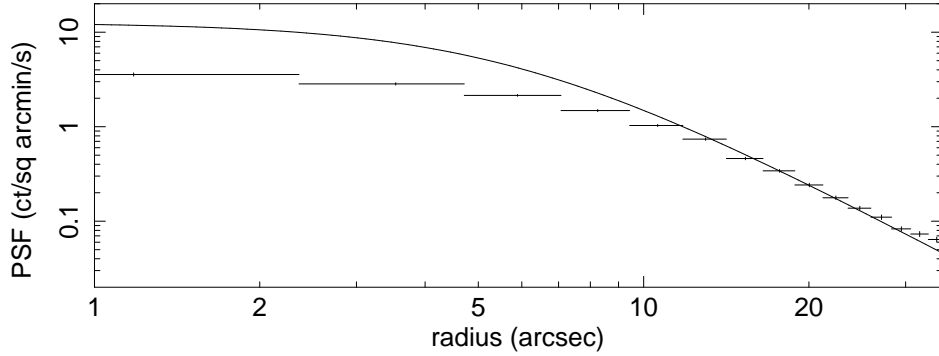Figure 3.2: The nominal PSF fit and the observed PSF data points for SWIFT J1729.9–3437. The data and the model deviate from each other before $\sim 12''$, therefore the inner region is excluded during extraction of source files by selecting an annulus.

XRT light curves are also extracted using the regions described above. They are extracted from the events barycentred with `BARYCORR v.1.11`. The energy range is 0.3–10.0 keV and the time resolution is 2.51 s. Background is subtracted using `LCMATH` with a scaling factor of 0.33, which is the ratio of source and background areas.

3.3 Timing Analysis

RXTE–PCA and *Swift*–XRT light curves of SWIFT J1729.9–3437 are used for the timing analysis. In Figure 3.3 530 s binned light curves are presented in order to give an illustration of time coverage of the data. The long term decrease of the outburst is also evident in Figure 3.3.

3.3.1 Timing Solution

The method described in Section 2.3.1 is applied in order to obtain the timing solution. For the timing analysis of SWIFT J1729.9–3437, 20 phase pulse profiles are constructed from the light curve segments and represented by 10 harmonics ($m = 10$ in Eqn. 2.1). Figure 3.4 shows examples of pulse profiles constructed from *Swift*–XRT and *RXTE*–PCA observations. The pulse arrival
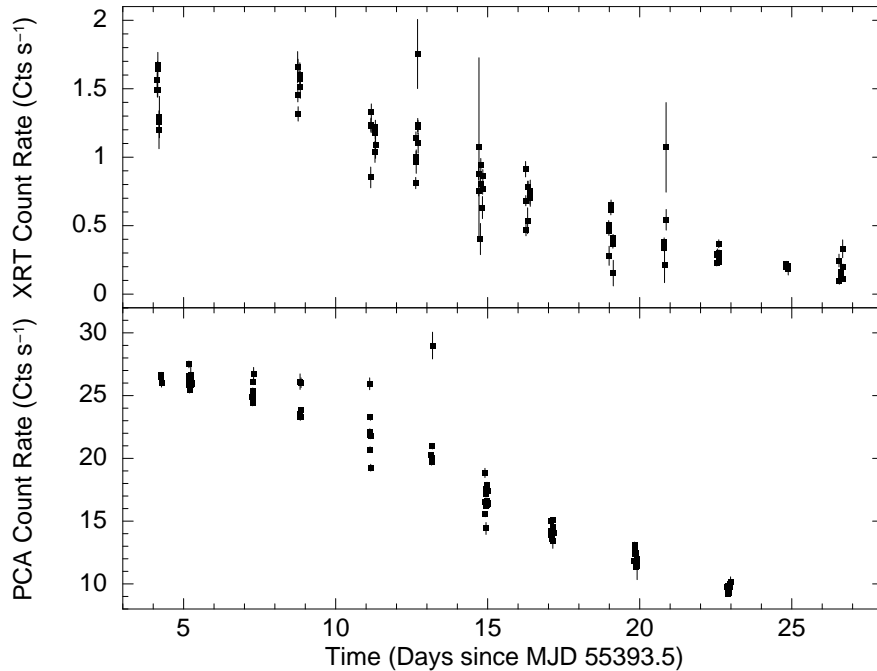
Figure 3.3: 530 s binned light curves of SWIFT J1729.9–3437. The upper panel is the 0.3–10.0 keV light curve from $Swift-$XRT and the lower panel is the 3–20 keV light curve from $RXTE-$PCA (PCU2 top layer).

times obtained by cross-correlation are connected in phase with a second order form of Eqn. 2.4. In Figure 3.5, pulse phase offsets after the removal of linear trend and the residuals of the quadratic fit are given. In this plot, cross markers are used for $RXTE$ and triangles are used for $Swift$ data points. Since $Swift$ pulse profiles have SNR lower than SNR of $RXTE$ profiles (see Fig. 3.4), the pulse phases of $Swift$ have larger error bars.

The timing solution obtained by the quadratic fit is given in Table 3.3. The remaining residuals from the quadratic fit are in agreement (giving a $\chi^2_{Red.} \simeq 1$) with a sinusoidal function;

$$\delta\phi = \frac{2\pi\nu_o}{P_{orb}} \frac{a}{c} \sin(i) \sin(l) \tag{3.2}$$

in which ν_o is the pulse frequency at t_o, $\frac{a}{c}\sin(i)$ is the light travel time for the projected semi-major axis, P_{orb} is the orbital period and $l = \frac{2\pi(t-T_{\pi/2})}{P_{orb}} + \frac{\pi}{2}$ is the mean orbital longitude at time t, $T_{\pi/2}$ is the epoch when $l = 90^o$. The

59
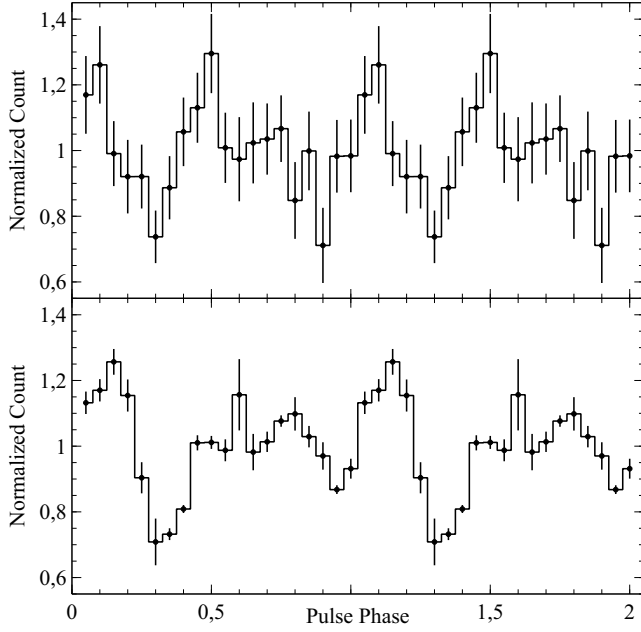
Figure 3.4: Sample pulse profiles of SWIFT J1729.9–3437. The upper panel is from the *Swift*–XRT observation with ID 31767001 and the lower panel is from the *RXTE*–PCA observation with ID 95044-05-01-00.

parameters of the circular orbit are reported in Table 3.3 and the plot of the fit is given in Figure 3.5 (a). The orbital period is found to be 15.3(2) days.

If the same residuals are fitted with an elliptical orbital model (see Fig. 3.5 (b));

$$\delta\phi = \frac{2\pi\nu_o}{P_{orb}} \frac{a}{c} \sin(i) \left[\cos(l) + e\cos(w)\cos(2l) + e\sin(w)\sin(2l)\right] \qquad (3.3)$$

(e is the eccentricity, w is the longitude of periastron) $\chi^2_{Red.}$ of the fit drops to ~ 0.4. Although the small $\chi^2_{Red.}$ means that the data is "over-fitted", this fit is useful for finding an upper limit to the eccentricity as 0.60.

Alternatively, the residuals from the timing solution can also be expressed by random fluctuations due to torque noise. The method described in Section 2.3.3 is applied in order to find the noise strength of SWIFT J1729.9–3437. For this estimation, a cubic polynomial is fitted to the residuals. Following the approach of Deeter (1984) the noise strength is calculated as 6.8×10^{-18} Hz s^{-2}. The order
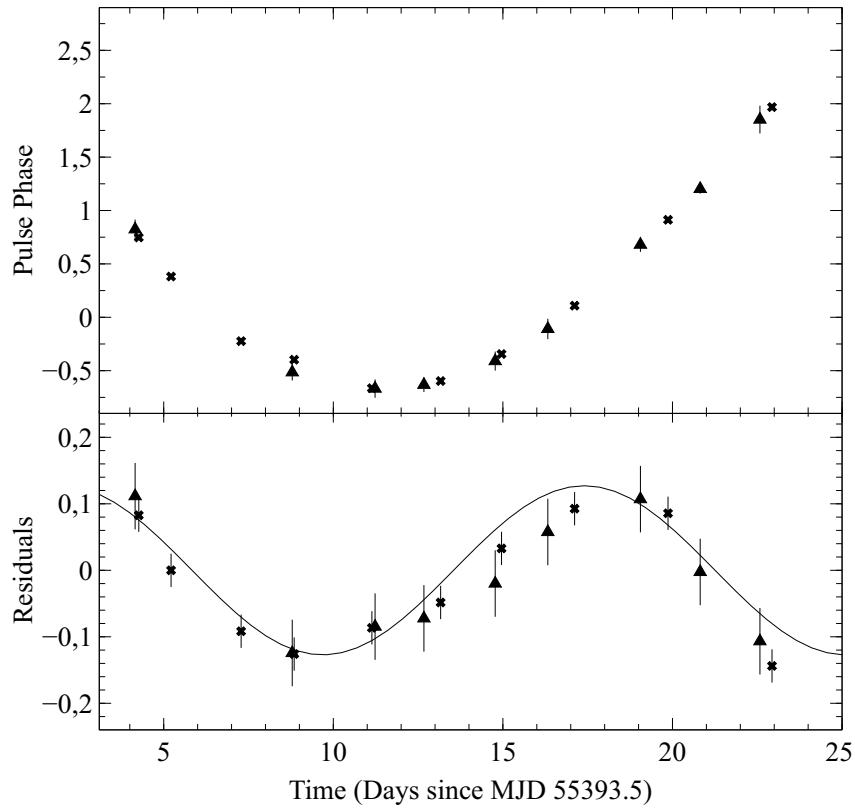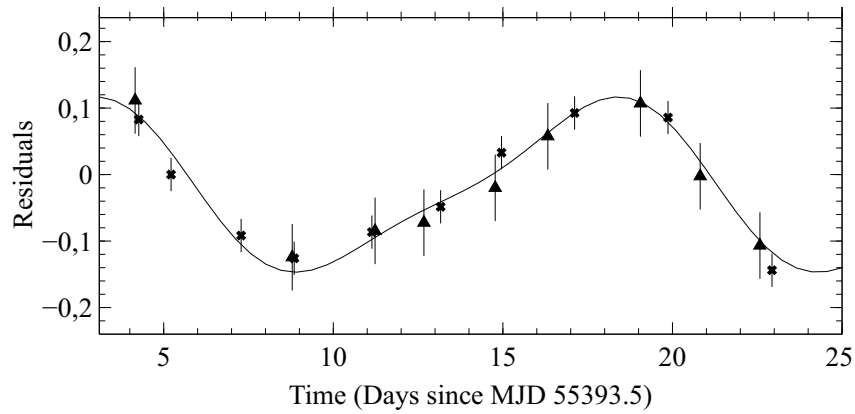
Figure 3.5: Pulse phase offsets of SWIFT J1729.9–3437 after the linear trend is removed (upper panel of (a)). Crosses represent *RXTE*–PCA points, whereas triangles are data from *Swift*–XRT. The residuals of the quadratic fit are fitted with a circular orbit model in lower panel of (a) (see Table 3.3 for model parameters). In (b), residuals are fitted with an elliptical orbital model giving an upper limit to the eccentricity as 0.60.

Table3.3: Timing solution and the parameters for the orbital model of SWIFT J1729.9–3437.

Timing Solution	Value
Timing Epoch (MJD)	55393.50(6)
Frequency (Hz)	$1.8734(8) \times 10^{-3}$
Frequency Derivative (Hz s^{-1})	$6.42(6) \times 10^{-12}$

Circular Orbital Model	Value
Orbital Epoch (MJD)	55395.7(6)
$\frac{a}{c} \sin i$ (lt.s)	65(3)
Orbital Period (days)	15.3(2)

of the noise strength is in agreement with the noise strength estimates of other accretion powered pulsars (Bildsten et al. 1997). Due to short time coverage of the observations, power density spectrum could not be constructed for SWIFT J1729.9–3437. A single measurement alone is not conclusive to discuss whether the source is a member of a disk-fed or a wind-fed system, since wind-fed systems have noise strengths between 10^{-20} and 10^{-18} Hz s^{-2} and disk fed systems have noise strengths between 10^{-15} and 10^{-18} Hz s^{-2} (see Section 2.3.3 and references therein).

3.3.2 Pulse Profiles

Sample pulse profiles for SWIFT J1729.9–3437 are given previously in Figure 3.4. At first sight, the profile has double peaks with approximately same relative counts; however one peak is narrower than the other with phase coverage of about 0.3 phases. *RXTE*–PCA observations of SWIFT J1729.9–3437 are further studied to find whether there are any changes in pulse profiles with respect to time and energy.

Pulse profile variation in time is directly examined on the 26 s binned light curves, in which a pulse is ∼20 bins. This method is chosen to search for pulse-to-pulse variations. For the first five observations pulse profiles are mainly
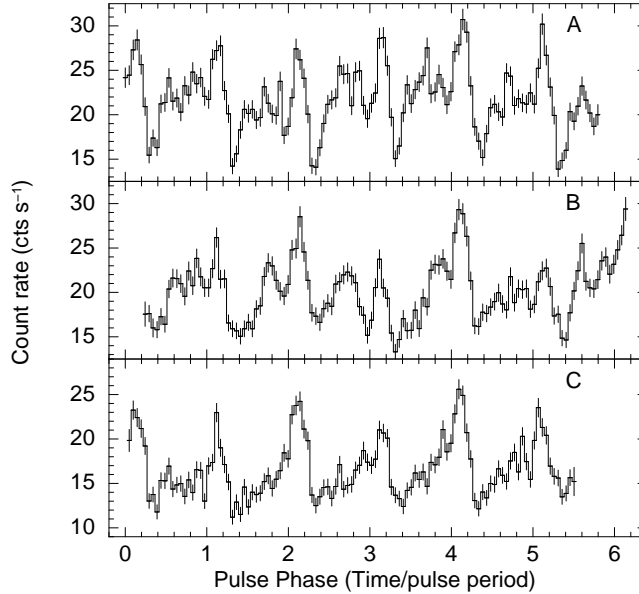
Figure 3.6: Pulse-to-pulse profile variation on 26 s binned light curves (3–20 keV, PCU2 top layer). X-axes are converted to phases (or time/pulse period) for arbitrary observation epochs. Three different examples are given for; A) double-peaked profiles (Obs. ID 95044-05-02-02) B) profile transformation to single-peaked (Obs. ID 95044-05-02-03) and C) single-peaked profiles (Obs. ID 95044-05-32-00).

double-peaked (see panel (A) of Fig. 3.6). The main peak is always narrow and sharp, where as the secondary peak somewhat changes from pulse to pulse. It is sometimes a high plateau and sometimes divided into two or three narrow peak-like features (see panel (A) of Fig. 3.6). The secondary peak starts to lose its intensity at the middle of the sixth observation (see panel (B) Fig. 3.6) and after that the pulses maintain a single-peaked profile (see panel (C) Fig. 3.6). During the profile transformation, the flux of SWIFT J1729.9–3437 is decreasing. 2–10 keV unabsorbed flux [1] is measured to be maximum for the second $RXTE$ observation, that is $3.04 \times 10^{-10} \, \mathrm{erg \, cm^{-2} \, s^{-1}}$. When the pulse profiles become single-peaked the flux drops to $1.96 \times 10^{-10} \, \mathrm{erg \, cm^{-2} \, s^{-1}}$. For the last $RXTE$ observation minimum flux is measured as $1.36 \times 10^{-10} \, \mathrm{erg \, cm^{-2} \, s^{-1}}$. Although the count rates significantly decrease during the outburst the flux of the source remains at the same order.

---

[1] 2–10 keV unabsorbed flux values are calculated from the model flux of individual spectral fitting of each observation.

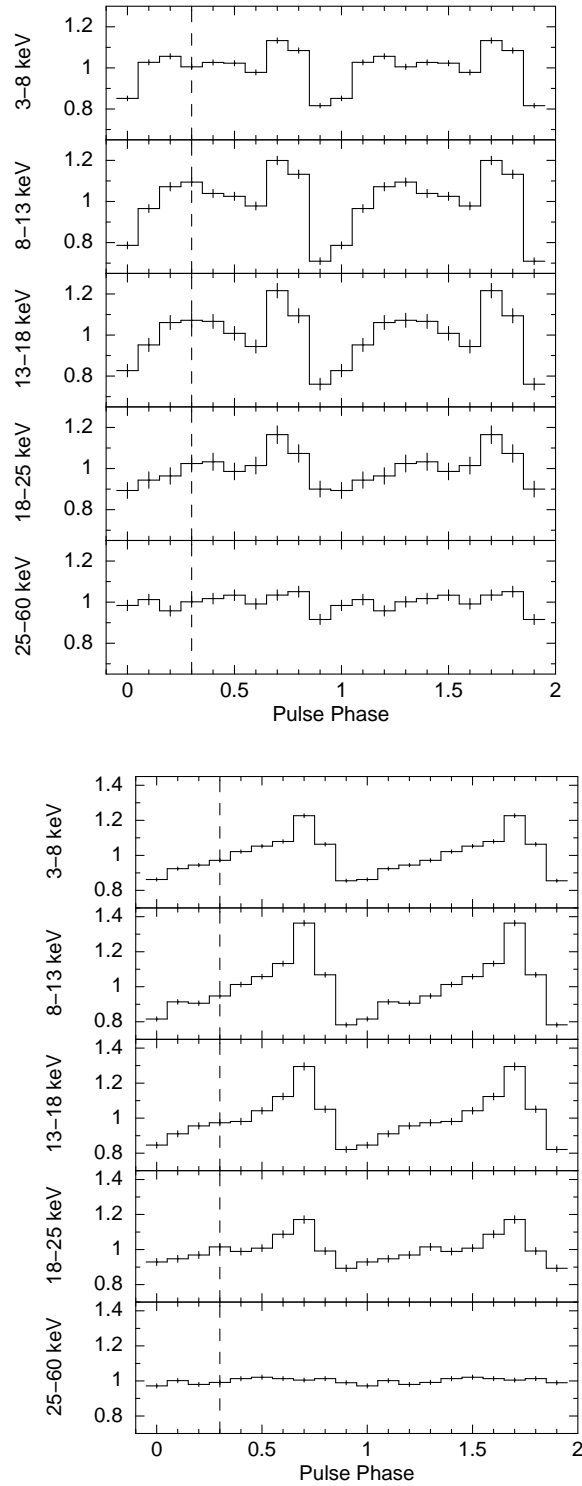Figure 3.7: Two samples for energy-resolved pulse profiles. Y-axes are normalized count rates. Energy bands are given on y-axes labels of each panel. The peak point of the secondary peak is represented with a dashed line. For Obs. ID 95044-05-02-00 (top panels) the secondary peak loses intensity in 18–25 keV band. On the bottom panels (Obs. ID 95044-05-03-00) energy dependence of a single-peaked profile is shown.

Energy-resolved pulse profiles [2] are constructed for each observation, in five energy bands; i.e. 3–8, 8–13, 13–18, 18–25 and 25–60 keV. The energy dependence for two of the observations are given as examples to double-peaked and single-peaked times in Figure 3.7. The pulse is evident in the first four energy bands, whereas the pulse fraction in the last band (25–60 keV) is ∼0.03. Although the shape of the profile does not strongly depend on energy during the double-peaked observations; there are two exceptions, one of which is given in Figure 3.7. The secondary peak, peaking around phase 0.3 significantly loses intensity in 18–25 keV pulse profiles of the observations with IDs 95044-05-02-00 and 95044-05-02-02. Moreover, calculating the pulse fractions for each energy band reveals that the strongest pulses are observed in 8–13 keV and 13–18 keV for all observations. The maximum fraction in 8–13 keV band is 0.23±0.01. The pulse fraction drops about 50% in 18–25 keV band, where as the fraction in 3–8 keV band is 30% less than the 8–13 keV value. Lastly, the pulse fractions of times with single-peaked profiles are slightly larger than the pulse fractions of double-peaked profiles. The highest pulse fraction is observed for the observation ID 95044-05-03-00 which is the first single-peaked observation (see Fig. 3.7).

3.3.3 Hardness Ratios

Energy-resolved light curves are generated for the same energy bands (i.e. 3–8, 8–13, 13–18 and 18–25 keV) and two hardness ratios are calculated as; HR1 $= \frac{8-13 \text{ keV}}{3-8 \text{ keV}}$ and HR2 $= \frac{18-25 \text{ keV}}{13-18 \text{ keV}}$ count rate ratios. First, HR1 and HR2 are averaged daily and the changes during the ∼20 days of time are explored (see (a) of Fig. 3.8). Only HR1 shows variation in time, whereas HR2 remains constant. HR1 values are around 1.1 for the first 4 observations, and then HR1 starts to decrease reaching to a minimum value of 0.77 for the last observation. The progress of HR1 is somewhat in line with the change in the shape of the pulse profile. The pulse profiles are double-peaked during the time interval of constant HR1; while for the decreasing interval of HR1 the pulse profiles are single-peaked. On the other hand, no significant change in energy-resolved pulse profiles is observed (see Fig. 3.7).

---

[2] Pulse Profiles are extracted from phase-binned spectra using the tool FBSSUM.
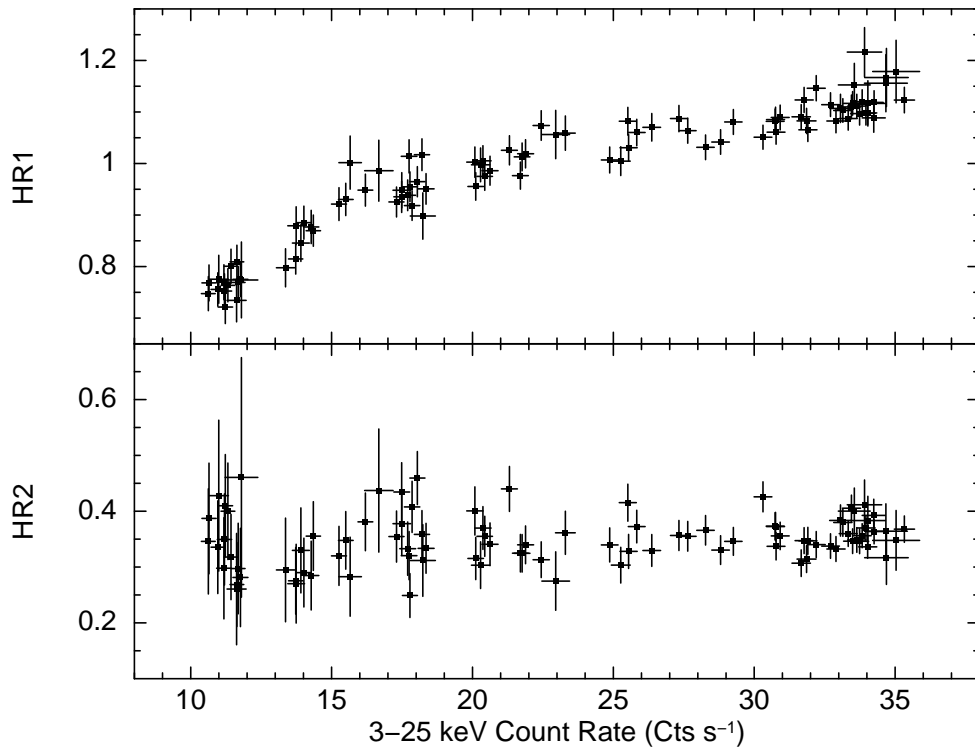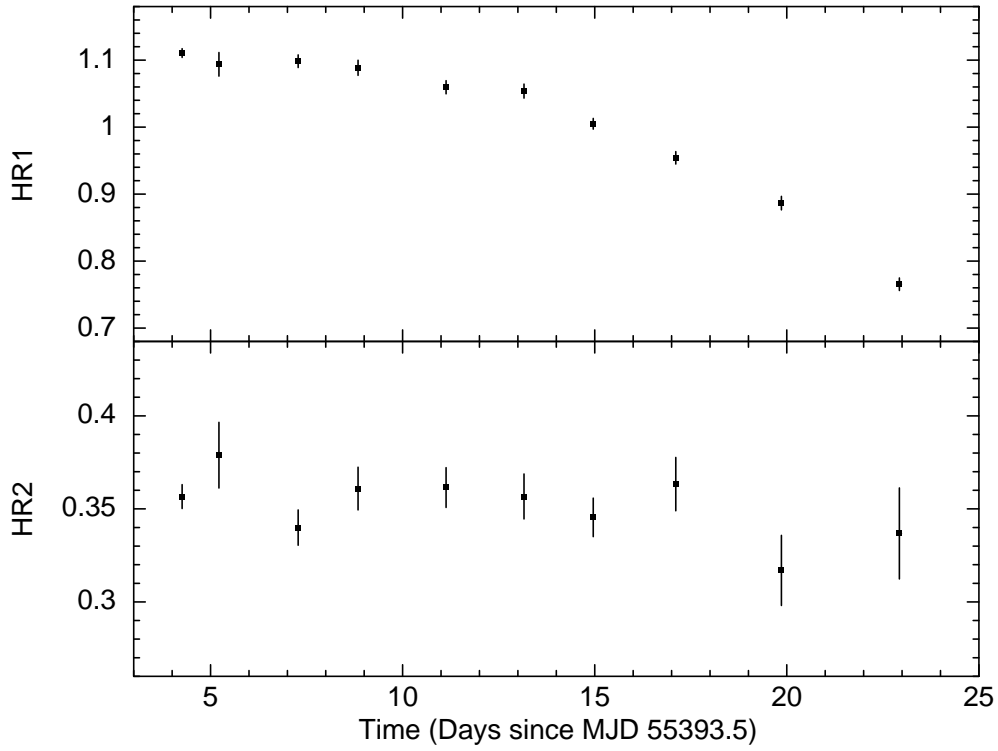
Figure 3.8: Hardness ratio variations in time and count rate. HR1 ($= \frac{8-13 \text{ keV}}{3-8 \text{ keV}}$) and HR2 ($= \frac{18-25 \text{ keV}}{13-18 \text{ keV}}$) ratios are constructed from energy resolved light curves. Daily averaged ratios are plotted over time at the top. 530 s binned ratios are plotted over 3–25 keV PCU2 count rates at the bottom.
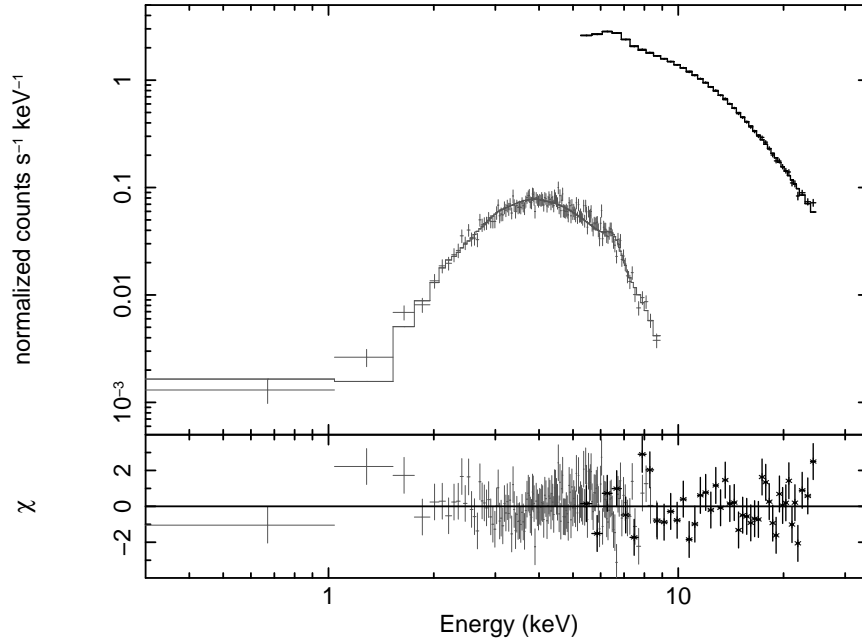
Figure 3.9: Simultaneous spectral fit of the overall XRT (0.3–9.3 keV; grey) and PCA (5–25 keV; black) spectra. Best fit is achieved by the model WABS×(CUTOFFPL+GAU) ($\chi^2 = 1.09$ see Table 4.7 for model parameters). The residuals of the fit are shown on the bottom panel.

Further investigation on hardness ratios is maintained on the variation with respect to total count rate. 530 s binned values for HR1 and HR2 are plotted over 3–25 keV count rate in (b) of Figure 3.8. HR1 shows correlation with the count rate, whereas HR2 remains constant again. As the count rate of SWIFT J1729.9–3437 declines during the outburst, HR1 continues to decrease. A drop in the $\frac{8-13 \text{ keV}}{3-8 \text{ keV}}$ ratio denotes that the decrease in 8–13 keV count rate is sharper than the decrease of 3–8 keV count rate, which also implies that the emission becomes softer as the count rate of SWIFT J1729.9–3437 diminishes.

3.4 Spectral Analysis

3.4.1 Overall Spectrum

The energy spectrum of the very first observations of SWIFT J1729.9–3437 was represented with a basic model of an absorbed power law with a high energy cut-

Table3.4: Spectral parameters for the best fit model `WABS`$\times$`(CUTOFFPL+GAU)`. C_1 and C_2 are constant multipliers for the different detectors. Uncertainties are calculated at the 90% confidence level.

Parameter	Unit	Value
C_1	for XRT	1.00 (fixed)
C_2	for PCA	1.55 ± 0.04
n_H	$(10^{22}\,\mathrm{cm}^{-2})$	$8.27^{+0.37}_{-0.36}$
Γ		1.23 ± 0.07
Γ Norm.	$(10^{-2}\,\mathrm{cts\,cm}^{-2}\,\mathrm{s}^{-1})$	$2.42^{+0.26}_{-0.25}$
E_{fold}	(keV)	$16.50^{+1.79}_{-1.52}$
E_{Fe}	(keV)	6.51 ± 0.03
σ_{Fe}	(keV)	$0.25^{+0.06}_{-0.05}$
Fe Norm.	$(10^{-4}\,\mathrm{cts\,cm}^{-2}\,\mathrm{s}^{-1})$	$4.68^{+0.49}_{-0.41}$
Unabs. $F_{0.3-9.3\,\mathrm{keV}}$	$(10^{-10}\,\mathrm{erg\,cm}^{-2}\,\mathrm{s}^{-1})$	$2.08^{+0.017}_{-0.024}$
Unabs. $F_{5-25\,\mathrm{keV}}$	$(10^{-10}\,\mathrm{erg\,cm}^{-2}\,\mathrm{s}^{-1})$	$3.00^{+0.004}_{-0.016}$
Reduced χ^2 (dof)		1.09 (187)

off (Markwardt et al. 2010b). Here, the spectral study of the source is extended by using all the available observations. A simultaneous fit to the overall 31 ks *Swift*–XRT and 42ks *RXTE*–PCA spectra is implemented with several cut-off power law models (i.e. `CUTOFFPL`, `HIGHECUT`, `FDCUT` and `NPEX`). The model parameters and their errors are best constrained using the `CUTOFFPL` model. During the simultaneous fit, a constant multiplier is added to the model in order to reckon with the normalization uncertainty between different detectors. Furthermore, `WABS` model is used for the photoelectric absorption. In addition; $\sim$6.4 keV *Fe* emission is modelled with a simple Gaussian line profile. Therefore, the best fit model comprises as `CONS*[WABS×(CUTOFFPL+GAU)]`, the fitting and its residuals are given in Figure 3.9 whereas the spectral parameters are listed in Table 4.7.

When the overall XRT and PCA spectra are modelled separately, the absorption component gives different results. This discrepancy was also reported by Markwardt et al. (2010b). A PCA only fit gives $n_H = 3.76 \pm 0.38 \times 10^{22}$ cm^{-2}, while a XRT only fit gives $n_H = 8.25 \pm 0.5 \times 10^{22}$ cm^{-2}. Beside this inconsistency, the best fit model is equally satisfactory for both spectra separately. The absorption parameter is determined from the first few spectral bins in the PCA spectrum. In contrast, the XRT spectrum is sensitive in the soft X-rays starting from 0.3 keV. Consequently XRT is a reliable instrument for absorption measurements. Therefore the energy range of the PCA spectrum is selected to be 5–25 keV during the simultaneous fit, while it is 0.3–9.3 keV for the XRT spectrum.

Markwardt et al. (2010b) reported a weak line at $\sim$6.6 keV in the spectrum of the first PCA observation. These authors could not be certain about the origin of this line, since the line was not present in the spectrum of the first XRT observation. For sources near the Galactic ridge, contamination to the spectrum due to the thermal emission from the ridge is a common problem for PCA, since its FOV is large. SWIFT J1729.9–3437 is close to the Galactic ridge, therefore the detection of the *Fe* line is challenging. The feature around $\sim$6.5 keV becomes more significant when an overall PCA spectrum is constructed from all observations. An attempt to fit this feature with Galactic ridge models (Valinia & Marshall 1998) confirms that the flux of the thermal ridge emission should

be two orders of magnitude smaller than the source flux of SWIFT J1729.9–3437, therefore the contamination could be neglected. Furthermore; when an overall XRT spectrum is constructed from all available observations, the Fe line appears to be present in the XRT spectrum as well. During the separate fits of the overall XRT spectrum, a simple absorbed power law fit gives a reduced χ^2 of 1.08 (χ^2/d.o.f. = 159.0/147), while the reduced χ^2 drops to 0.98 (χ^2/d.o.f. = 143.8/146) when a Gaussian profile is added with line energy 6.40 ± 0.06 keV ($\sigma_{Fe} = 0$; fixed). The F-test probability calculated for this improvement is achieved by chance is 1.3×10^{-4}. When the overall PCA spectrum is fitted alone, the line energy is found as $6.53^{+0.05}_{-0.02}$ keV. Also a similar value is found for the simultaneous fit (see Table 4.7). There appears to be an instrumental broadening for the line energy in PCA spectrum. Although the energy of the neutral Fe I K_α emission line is located correctly for XRT spectrum, the simultaneous fit seems to be effected by the strong distortion in PCA spectral bins. In conclusion, there is strong evidence that the Fe emission originates from the source.

3.4.2   Spectra of Individual $RXTE$ Observations

Individual spectra for 10 $RXTE$ observations are modelled with the same model (WABS$\times$(CUTOFFPL+GAU)) that is used to describe the overall spectrum. As discussed previously, the hydrogen column density for PCA is different than the one for XRT spectrum. n_H value is left as a free parameter during fits of the individual PCA spectra not to deteriorate the spectral statistics. The resulting parameters are plotted with respect to time in Figure 3.10. The panels of this figure from top to bottom are unabsorbed flux at 2–10 keV, n_H, photon index, exponential folding energy (E_{fold}), Fe line energy (E_{Fe}) and the reduced χ^2. The reducing flux in the uppermost panel demonstrates the decline of the outburst. In the third panel a slight increase in the photon index with time is observed. The photon index values are increasing with the decreasing flux, indicating a spectral softening with decreasing flux. This outcome is also confirmed by the hardness ratio changes with the source count rate in Figure 3.8. n_H, E_{fold} and E_{Fe} remain constant within their error ranges, although a $\sim$15 day modulation of E_{fold} values exists, when the error bars are not considered. 12.1 keV and 16.2
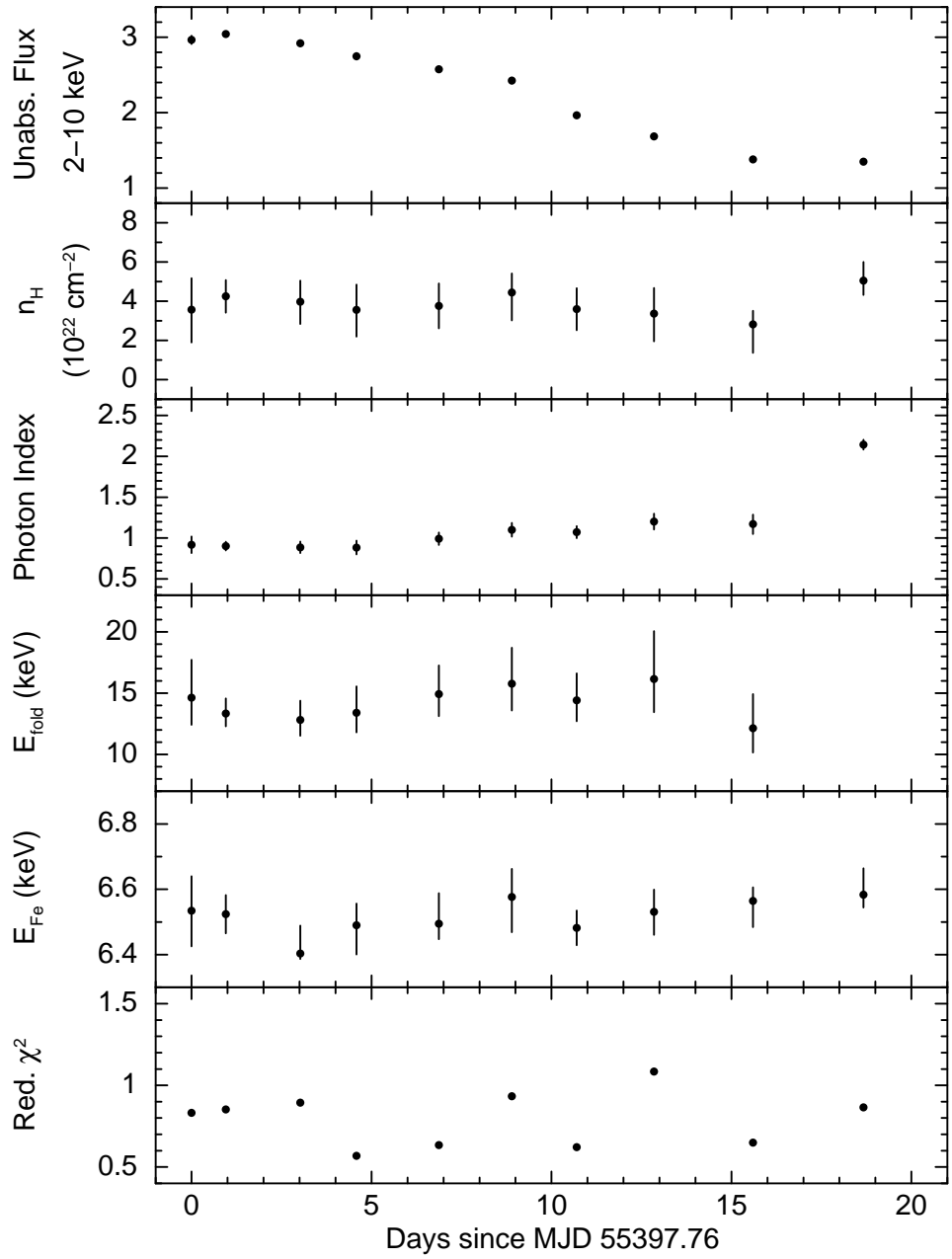
Figure 3.10: Spectral fit results of individual *RXTE*–PCA observations. The panels from top to bottom are unabsorbed flux at 2–10 keV, n_H, photon index, exponential folding energy, *Fe* line energy and the reduced χ^2. Uncertainty of each parameter is calculated for 90% confidence range.
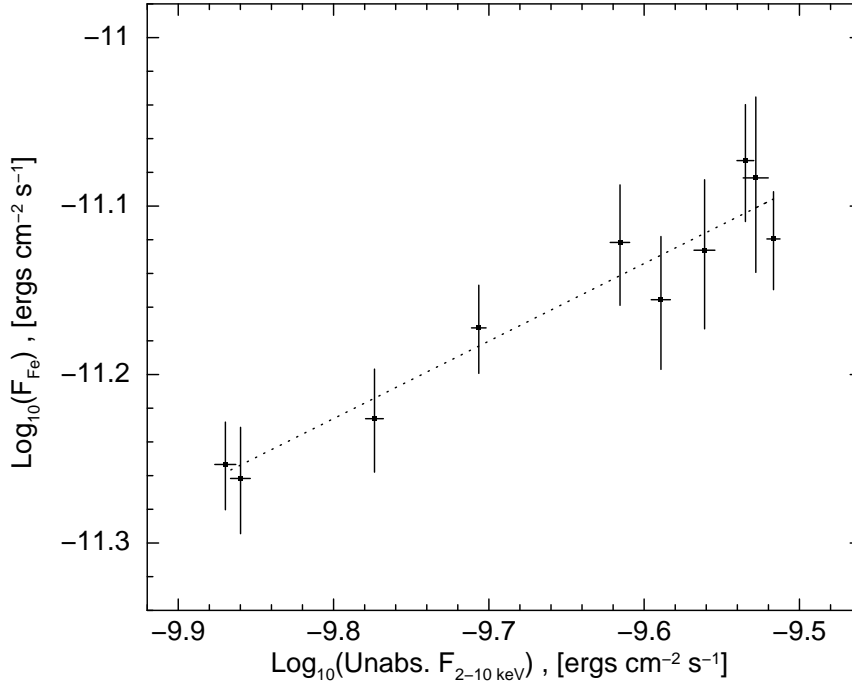
Figure 3.11: The flux variation of Fe line with the X-ray flux of SWIFT J1729.9–3437. X and Y error bars indicate 68% confidence range (1σ) of the parameters. The linear fit to the data is represented by the dotted line.

keV are the minimum and maximum energies obtained for E_{fold}.

The contribution of Fe line to the total flux is measured using the CFLUX model in XSPEC, which allows one to measure the flux of a single model component. The line flux values (F_{Fe}) are found to be correlated with the total source flux of SWIFT J1729.9–3437 ($F_{2-10keV}$) (see Fig. 3.11). A linear fit to the $\log(F_{Fe})$ versus $\log(F_{2-10keV})$ plot gives a slope of 0.46 ± 0.12 and the Pearson product-moment correlation coefficient [3] between the parameters is 0.96 with a null-hypothesis probability [4] of 1.2×10^{-5}. The correlation between Fe line intensity

---

[3] Pearson product-moment correlation coefficient (r) of two variables (X, Y) with n values, is calculated as;

$$r = \frac{\sum_{i=1}^{n}(x_i - \overline{x})(y_i - \overline{y})}{\sqrt{\sum_{i=1}^{n}(x_i - \overline{x})^2 \sum_{i=1}^{n}(y_i - \overline{y})^2}} \tag{3.4}$$

that is the covariance of (X, Y) divided by the product of the standard deviations. $\overline{x}$ and $\overline{y}$ are the mean of the variables. This equation gives a value between -1 and 1. 1 means a linear positive correlation and -1 means a negative correlation, whereas 0 means no correlation.

[4] Null-hypothesis probability, or the p-value, is a measure of significance of the observed correlation. The significance is larger for smaller p-value. p-value is calculated from a two-tailed Student's t distribution $p = T(n-2, t)$, where t is calculated using r as, $t = r\sqrt{\frac{n-2}{1-r^2}}$. Here, $(n-2)$ is the degrees of freedom for n data points.

and continuum intensity is observed for many sources (e.g. Vela X–1: Ohashi et al 1984, GX 301–2: Leahy et al. 1989, Cen X-3: Naik et al. 2011). In HMXBs, the line producing region is specified as the cold and low ionized material surrounding the neutron star (White et al. 1983). The X-ray emission absorbed by this matter causes fluorescence in the cold plasma. While the reprocessing of X-rays increases with higher luminosities, the surrounding matter is illuminated more and more resulting in more intense *Fe* lines. Therefore the correlation between the line flux and source luminosity found for SWIFT J1729.9–3437, is yet another evidence for the origin of the *Fe* emission.

3.4.3 Pulse Phase Resolved Spectra

The phase resolved spectra of SWIFT J1729.9–3437 are constructed for the first three *RXTE* observations, which correspond to times of maximum source brightness. Five spectra each of which is about 2.1 ks are generated from a total of 10.4 ks exposure time. For correct binning in pulse phase, the timing solution (see Table 3.3) is appended into the timing file (i.e. `psrtime.dat`) of the `FASEBIN` tool. Background emission is estimated from the three observations that are being considered for the analysis. Spectral response files are produced for the un-phase-binned spectrum of the same data. 3–25 keV spectra of each bin is modelled with (`WABS`×(`CUTOFFPL`+`GAU`). During the analysis, n_H and E_{Fe} are kept as fixed parameters, as they are not expected to vary based upon the preliminary fitting results. Therefore, we focus on the variation of the photon index and exponential folding energy of the high energy cut-off here.

The variation of spectral parameters in pulse phase are given in Figure 3.12. Ten phase-binned pulse profile of SWIFT J1729.9–3437 is given in the uppermost panel. Below that, from top to bottom; 2–10 keV unabsorbed flux, photon index and exponential folding energy results from five phase bins are plotted. The reduced χ^2 of the fits are given in the lowermost panel. Comparing the photon index variation with the normalized count rates, it is certain that the highest spectral index (or the softest emission), that is 1.14 ± 0.13, is measured for the lowest count rate around phase 0.05. Furthermore, the photon index of

73
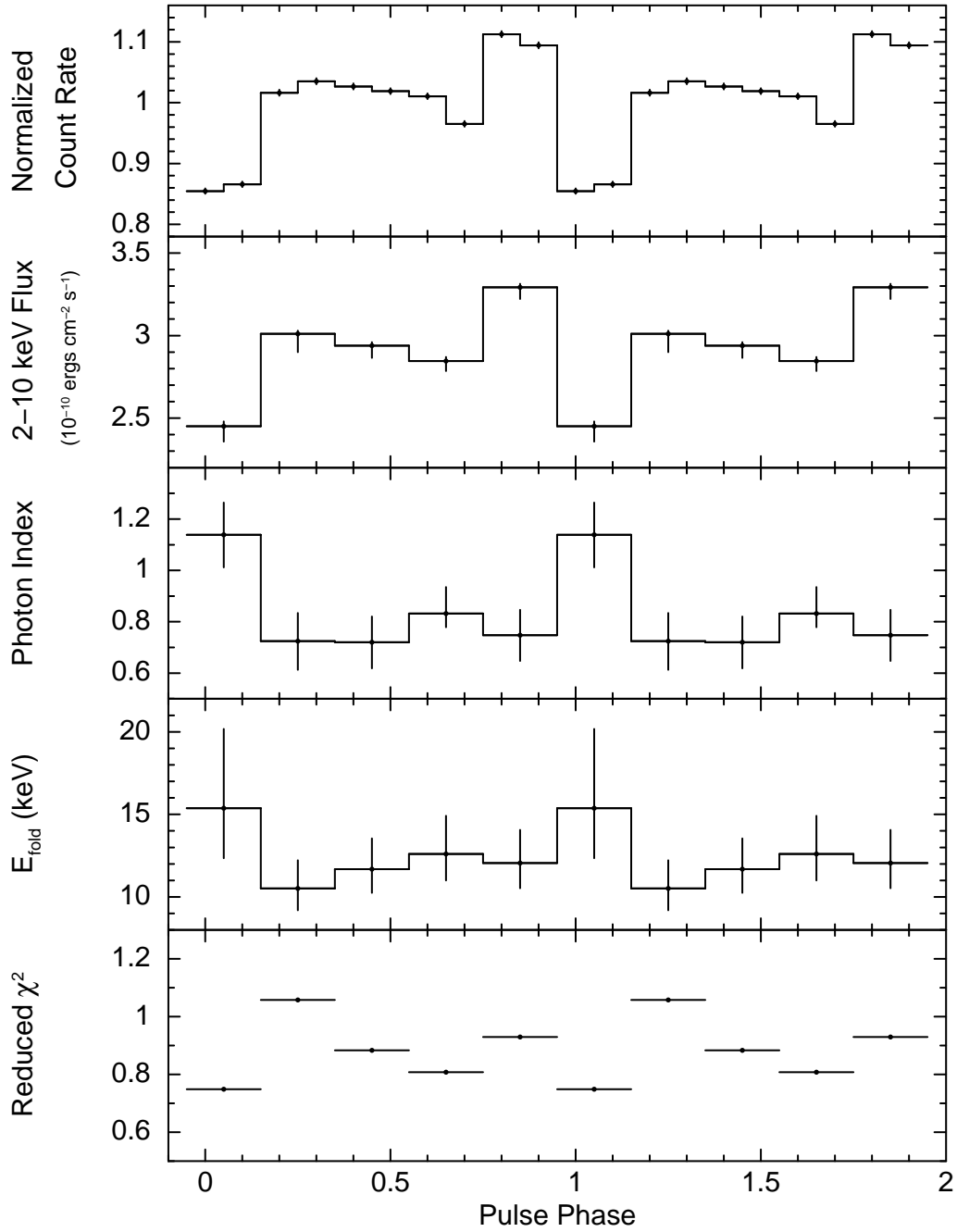
Figure 3.12: Variation of spectral parameters in pulse phase. 10 phase-binned pulse profile is plotted at the uppermost panel for comparison. 2–10 keV unabsorbed flux, photon index, exponential folding energy and reduced χ^2 of the fits are plotted in the following panels respectively. Uncertainty of each parameter is calculated for 90% confidence range. The same data is plotted repetitively in two cycles for a clear demonstration.

the bin corresponding to the local minimum between the pulse peaks is slightly larger than the neighbouring bins. Therefore, it seems that there is an inverse correlation between photon index and pulsed flux. The correlation coefficient between these parameters is calculated as -0.87 with a null-hypothesis probability around 0.06. Although the p-value is quite high these parameters are possibly physically related, since we find similar correlation between flux and photon index in time resolved spectral results (see Fig. 3.10). E_{fold} value is also maximum ($15.37^{+4.80}_{-3.03}$ keV) for the un-pulsed emission around phase 0.05, however the low count rates result in lower SNR in spectra making it difficult to constrain the errors of E_{fold}. Folding energy can be regarded as constant when the large uncertainties are considered. A constant fit to the fourth panel of Figure 3.12 gives a value of 11.7 ± 1.1 keV, that is lower than an average value for the time resolved spectra (see Fig. 3.10). Therefore the variation of E_{fold} with pulse phase might not be clearly resolved. The correlation coefficient between E_{fold} and photon index is 0.96 with a null-hypothesis probability of 0.01. However one should note that this correlation analysis ignores the uncertainties in the parameters.

3.5   Summary and Discussion

In this chapter, the properties of SWIFT J1729.9–3437 are investigated via its *RXTE* and *Swift* observations during the 2010 outburst. A timing solution for the pulsar (see Table 3.3) is acquired by the analysis of time series. The spin frequency of the pulsar is measured as $1.8734(8) \times 10^{-3}$ Hz. The arrival times are fitted with a quadratic polynomial turning out that the pulsar is spinning up with a rate of $6.42(6) \times 10^{-12}$ Hz s^{-1}. Further analysis on the residuals of the arrival times, reveals another possible periodicity of the source. A circular orbital model with a period of 15.3(2) days fits the data well, whereas an elliptical orbital model with the same period gives an upper limit to the eccentricity of the system as 0.60. Definitely, more observations of the source is required in order to refine the properties of orbit, since the data analysed only covers a time span of about 20 days. However, the source dimmed out since the outburst.

Even though a counterpart could not be detected for SWIFT J1729.9–3437, the determination of an orbital period strengthens its binary nature.

The mass function for a binary system is given as,

$$f(M_c, M_*) = \frac{4\pi^2}{G} \frac{(a\sin i)^3}{P_{orb}^2} = \frac{(M_c\sin i)^3}{(M_c + M_*)^2} \qquad (3.5)$$

where G is the gravitational constant, i is the binary inclination angle, $(a\sin i)$ is the projected semi-major axis, P_{orb} is the orbital period, M_c is the mass of the counterpart and M_* is the mass of the pulsar. When the $P_{orb} = 15.3$ d and $\frac{a}{c}\sin i = 65$ lt.s are used to calculate the mass function of SWIFT J1729.9–3437, Eqn. 3.5 gives a value of $\sim 1.3\,M_\odot$. Mass function of a binary system provides the minimum mass of the counterpart, when $i = 90^o$. This corresponds to minimum of $M_c = 2.82\,M_\odot$ for SWIFT J1729.9–3437, assuming $M_* = 1.4\,M_\odot$. As soon as SWIFT J1729.9–3437 takes its place on the Corbet diagram (Corbet 1984) with $P_{orb} = 15.3$ d and $P_{spin} = 533.76$ s, it lies in the region of high mass systems with a supergiant counterpart. Therefore, the orbital inclination should be small (i.e. $20^o < i < 30^o$ [5]) for the system.

On the other hand, alternative to the orbital models the residuals of the arrival times are used to calculate the torque noise strength of SWIFT J1729.9–3437. The value is found to be 6.8×10^{-18} Hz s^{-2}, which is quite consistent with other similar systems (Bildsten et al. 1997). If the source could be detected for a longer period of time, that allows one to observe at least two or three orbital cycles, the orbital solution would be stronger. However, the observations only cover a 1.25 cycle if the 15.3 day orbit is correct. Hence, there is a possibility that the residuals are only implying the torque noise fluctuations of the source. Future observations with longer time coverage are needed to identify the characteristics of the source.

The pulse profile variation with respect to time and energy are studied. While the initial profile is double-peaked, one peak loses its intensity significantly starting from MJD 55406.7 (see Fig. 3.6). During the change of shape the source

[5] The mass of the companion would be $34.13\,M_\odot > M_c > 12.47\,M_\odot$

flux decreases slightly, whereas the pulsed fraction increases a little. The transition from double-peak to single-peak profile can be explained by a change in the radiation pattern from fan beam to pencil beam. For high luminosities; a shock slows down the in-falling plasma, in which the photons are scattered resulting in a perpendicular emission and for lower luminosities the radiation is mostly along the magnetic axis of the pulsar (Wang & Welter 1981). Limiting luminosity that distinguishes the two different patterns is found, by solving hydrodynamic and radiative diffusion equations as $L_{lim} \approx 5 \times 10^{36}$ erg s^{-1} (White et al. 1983). During the pulse shape transition of SWIFT J1729.9–3437, the source flux is measured as 1.96×10^{-10} erg cm^{-2} s^{-1}. If this flux is assumed to be the L_{lim}, corresponding distance of SWIFT J1729.9–3437 would be ~15 kpc. This distance is a bit too far, where the source would be beyond the Galactic bulge on the outer wings of the Galactic plane. Moreover energy resolved pulse profiles show that the pulse is the strongest in the energy range from 8 to 18 keV. Apart from a fractional variation, there is no strong energy dependence of the pulse shape (see Fig. 3.7). Fan beam sources such as EXO 2030+375 (Parmar et al. 1989) and GX 1+4 (Paul et al. 1997), are known to have strong profile variations with energy. This behaviour is explained by the fact that, for lower energy photons the scattering cross-section depends on the propagation direction of the emission, whereas it does not for higher energy photons (Nagel 1981). Therefore more complex profile shapes are expected in lower energies for fan beam sources. However, lack of significant variation with energy for SWIFT J1729.9–3437 puts the fan beam interpretation into a disputable position.

For SWIFT J1729.9–3437, one of the two hardness ratios, HR1 ($= \frac{8-13 \text{ keV}}{3-8 \text{ keV}}$) is found to be decreasing as the flux drops during the decline of the outburst (see Fig. 3.8). Decreasing hardness ratio indicates that the radiation becomes softer, or that the 3–8 keV counts become more dominant on 8–13 keV counts as the overall continuum dims out. In other words, the X-ray emission becomes harder with increasing luminosity. For X-ray pulsars, an increase in X-ray luminosity is mainly associated with increasing mass accretion rate. The mechanism that produces hard X-ray photons is basically the comptonization of soft photons by the high energy electrons in the accretion column (Becker & Wolff 2007).

The soft photons emerging from the poles of the neutron star accumulate with increasing accretion rate, and the number of high energy electrons will also rise within the accretion column. Therefore, during the comptonization process the photons up-scatter with increasing number of collisions with electrons, producing harder X-ray photons. Hardness-intensity relations for several sources show similar behavior. For example 1A 0535+262, A 1118–616, SWIFT J1626.6–5156, XTE J0658–073 and GRO J1008–57 are sources which emit harder photons with increasing flux (Reig & Nespoli, 2013).

An overall spectrum constructed from all available *RXTE* and *Swift* observations of SWIFT J1729.9–3437 is modelled by an absorbed power law with a high energy cut-off plus a Gaussian for *Fe* emission line at 6.51 keV (see Fig. 3.9 and Table 4.7). The evidences that verify the origin of the *Fe* emission as the source itself, are rather strong. The only significant outcome of time resolved analysis on the spectral variation, is the correlation of *Fe* line flux with the source flux (see Fig. 3.11). The matter should be relatively cool and low ionized in order to emit *Fe* lines. Since absorption of the X-rays within the surrounding material ignites the fluorescence in the plasma, higher luminosities strengthen the *Fe* lines due to enhanced reprocessing. Less significant spectral changes in time are the spectral softening with decreasing flux and a possible variation in the folding energy of the cut-off (see Fig. 3.10). The phase resolved variation on spectral parameters is also investigated. The results indicate a weak evidence that the spectral index is dropping during pulsed flux and it is maximum for the un-pulsed emission at phase 0.05 (see Fig. 3.12). Furthermore, there is a marginal detection of the folding energy dependence on the photon index.

As mentioned above, SWIFT J1729.9–3437 lies in the region of wind-fed supergiant region on the Corbet diagram (Corbet 1984). The classical systems of this type are persistent sources of X-ray, in contrast SWIFT J1729.9–3437 is a transient source. On the upper left region of P_{orb} versus P_{spin} graph there are also transient systems which belong to other sub-classes of HMXBs, such as SFXTs and Obscured HMXBs. Outburst duration of SFXTs are very short, generally at the order of hours with a maximum duration of 1–2 days. Approximately one month duration of the 2010 outburst of SWIFT J1729.9–3437 is very long for

the system to be a SFXT. Furthermore; most of the SFXTs display recurrent outbursts linked to their orbital period, but SWIFT J1729.9–3437 showed only one burst since 2010. Moreover; X-ray spectra of SFXTs have soft blackbody components which we do not observe in the spectra of SWIFT J1729.9–3437. On the other hand, obscured HMXBs are faint sources with high absorption parameters where hydrogen column densities are at the order of 10^{23} atoms per cm^2. They have hard X-ray spectra with photon index in the range 0.5 to 1. The spectral results for SWIFT J1729.9–3437 are in agreement with obscured sources. In addition; the galactic position of SWIFT J1729.9–3437 is also convenient, since most of the obscured sources are discovered in the Galactic bulge along the Norma and Scutum spiral arms.

CHAPTER 4

SWIFT J0513.4–6547

In this chapter, X-ray spectral and timing properties of SWIFT J0513.4–6547 throughout its two outbursts are given. The first outburst is monitored with both *RXTE* and *Swift* from 2009 April 11 to 2009 May 13 (MJD 54932 – MJD 54964). The second outburst in 2014 is only monitored with *Swift*. This study is submitted for publication on MNRAS with the title "*RXTE and Swift observations of SWIFT J0513.4–6547*" (Şahiner et al. 2015).

4.1   Introduction

SWIFT J0513.4–6547 is a new X-ray transient detected with the *Swift*–BAT on 2009 April 2 (MJD 54923) (Krimm et al. 2009). The coordinates of the source is consistent with the Large Magellanic Cloud (LMC), therefore it is one of the 14 [1] APPs in LMC. Search in older data had shown that SWIFT J0513.4–6547 had become active one month before its discovery (since 2009 March 4) and peak brightness of ~ 40 mCrab had been measured for the date 2009 March 6. *RXTE* observations monitored the source until 2009 May 13 (MJD 54964) and strong pulsations with 27.28 s periodicity is detected in the light curves. A possible optical companion (2MASS 05132826–6547187) within the X-ray error circle strengthened the classification of the source as an HMXB (Krimm et al. 2009, Krimm et al. 2013). A recent optical study of the companion identified its spectral type as B1Ve, therefore the system is a *Be*/XB (Coe et al. 2015).

---

[1]   http://www.soton.ac.uk/~mjcoe/smc/

81

The orbital period of SWIFT J0513.4–6547 is 27.4 days. This period is first detected on 4.5 years of OGLE IV (Optical Gravitational Lensing Experiment Phase IV) optical light curve (Coe, Udalski & Finger 2013, Coe et al. 2015). The optical magnitude is found to be flickering ~ 0.05 regularly. Assuming that this modulation is because of the binary motion of the system, SWIFT J0513.4–6547 takes its position on the Corbet diagram within the cluster of points representing the *Be*/XBs. Coe et al. (2015) also revised the pulse detections with *Fermi*–GBM (Gamma Ray Burst Monitor) (Finger & Beklen 2009) and using the pulse timing method they confirmed that the optical period is actually the orbital period observed in X-rays. The upper limit of eccentricity provided by the same study is 0.17 using an orbital model with a fixed period of 27.405 d.

SWIFT J0513.4–6547 has become active again recently. It is detected on the *XMM-Newton* slew data of 2014 August 25 (MJD 56894) with a luminosity at the order of 10^{36} erg s^{-1} (Sturm et al. 2014). Follow-up observations of 2014 outburst are held on with *Swift*, however the source could only be monitored for 7 times until the end of the year. The luminosity of observations on September 19 (MJD 56919) and October 16 (MJD 56946) are also at the order of 10^{36} erg s^{-1}. These three luminosity peaks are at times of expected optical maximum, which may indicate that the 2014 outbursts of SWIFT J0513.4–6547 might be Type I outbursts, which are observed recurrently in certain orbital phases of *Be*/XBs due to enhanced mass transfer (see Chapter 1). On the other hand, 2009 outburst can be classified as a Type II outburst since the peak luminosity reaches to 1.3×10^{38} erg s^{-1} (Coe et al. 2015) and the decay of the outburst proceeded for about two orbital cycles.

4.2 Observations and Data Reduction

4.2.1 *RXTE*

18 *RXTE*–PCA observations of SWIFT J0513.4–6547 were carried out between 2009 April 14 (MJD 54935) and 2009 May 13 (MJD 54964) (see Table 4.1). These observations monitor the final stages of the 2009 outburst. Standard data

reduction is carried on by using the tools of `HEASOFT V.6.15.1`. Time filtering is applied with the criteria on elevation angle to be greater than 10°, offset from the source to be less than $0^o.02$ and electron contamination of PCU2 to be less than 0.1. The data within 30 minutes of the peak of South Atlantic Anomaly (SAA) is also excluded in order to increase signal-to-noise ratio (SNR). The resulting net exposure after the filtering is 24 ks.

For the timing analysis 0.1 s binned 3–10 keV light curves are generated from Good Xenon events, whereas Standard2f mode data are considered for broad spectral analysis. Furthermore, pulse phase resolved spectra are constructed using Good Xenon events in the `FASEBIN` tool. Moreover the count rates per phase bin are obtained by the tool `FBSSUM` in order to construct energy-resolved pulse profiles of the source. Only data from PCU2 are selected during the extraction of spectral files, since it is the only PCU that is active during all of the observations. In addition, only photons that are detected on the top anode layers of the detector are selected in order to increase SNR. EPOCH 5C background model supplied for faint sources (i.e. < 40 cts/s/PCU) is used to subtract the background from spectra and light curves.

4.2.2 *SWIFT*

As soon as *Swift*–BAT discovered SWIFT J0513.4–6547 on 2009 April, 3 follow-up *Swift*–XRT observations were performed. There are also 7 *Swift*–XRT pointings that monitor the 2014 re-brightening of the source. A log of *Swift*–XRT observations is given in Table 4.2. The total exposure of 2009 and 2014 observations are 12.67 ks and 7.92 ks respectively. The data mode is photon counting (PC) for all XRT observations, this mode has a time resolution of ~2.5 s. The default screening criteria of `XRTPIPELINE V.0.13.0` script of `XRTDAS V.2.9.2` package are used during filtering of XRT event files. Standard grade filtering (0-12) is applied to the data. For each observation, vignetting corrected exposure maps are generated during the pipeline processing.

The XRT count rates of 2009 observations were just around the pile-up limit (~ 0.5 cts s^{-1}), therefore the events are corrected for pile-up as explained in

Table4.1: Log of *RXTE*–PCA observations of SWIFT J0513.4–6547.

Observation ID	Mid-Time(MJD)	Exposure (s)
94065-01-01-00	54935.43	624
94065-01-02-00	54938.95	2112
94065-01-02-01	54941.45	1072
94065-01-02-02	54944.53	640
94065-01-03-00	54945.51	832
94065-01-03-01	54946.35	1488
94065-01-03-02	54946.42	1168
94065-01-03-03	54946.48	576
94065-01-03-04	54946.87	3792
94065-01-03-05	54947.05	1936
94421-01-01-02	54948.71	1472
94421-01-01-00	54949.94	2160
94421-01-02-00	54953.10	2032
94421-01-02-02	54955.06	640
94421-01-02-01	54958.91	1344
94421-01-03-00	54960.41	352
94421-01-03-01	54962.37	624
94421-01-03-02	54964.42	1104

Table4.2: Log of *Swift*–XRT observations of SWIFT J0513.4–6547. The observations given above the horizontal line are from 2009, whereas 2014 observations are below the line.

Observation ID	Start Time (MJD)	Off-axis (′)	Exposure (s)
00031393001	54932.07	0.45	4635
00031393002	54937.22	0.35	6341
00031393003	54940.02	1.01	1693
00031393004	56916.87	0.10	934
00031393005	56919.86	2.12	1413
00031393006	56925.05	0.39	969
00031393007	56939.77	2.48	1001
00031393008	56946.18	1.53	1244
00033532001	56985.54	2.39	1306
00033532002	56986.79	1.21	1051

Section 3.2.2 of the previous chapter. The PSF fit used to determine the inner radius of the source annulus is given in Figure 4.1. The annular source region for 2009 observations is selected to have an inner radius of $\sim 7''$, while the outer radius is determined as $\sim 70''$ (see Figure 4.2). On the contrary, the count rates were low (~ 0.1 cts s^{-1}) in 2014 observations, therefore a circular region with $\sim 35''$ radius is used for source extraction. For the background extraction, the same circular source-free region with $\sim$140 arcsec radius is used for both 2009 and 2014 observations (see Figure 4.2). Light curves and spectra are extracted by filtering selected regions using XSELECT V.2.4C.

For the overall spectral analysis of SWIFT J0513.4–6547, XRT spectral files are re-binned to have at least 20 counts per energy bin, which is required for χ^2 statistics to be applicable. For the individual observations, XRT spectra are re-binned to have at least 1 count per bin for Cash statistics (Cash 1979), as it is advised to use this statistical method for low count spectra. The latest response matrix file (version v014) is used and individual ancillary response files are created with the tool XRTMKARF V.0.6.0 using the exposure maps produced during the pipeline processing. Spectral analysis is performed using XSPEC V.12.8.1g.

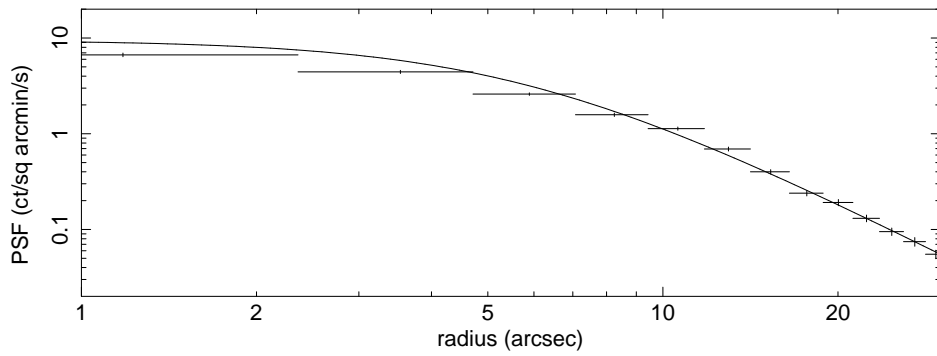Figure 4.1: The nominal PSF fit and the observed PSF data points for SWIFT J0513.4–6547 for 2009 observations. The data and the model deviate from each other before ~ 7″, therefore the inner region is excluded during extraction of source files by selecting an annulus.
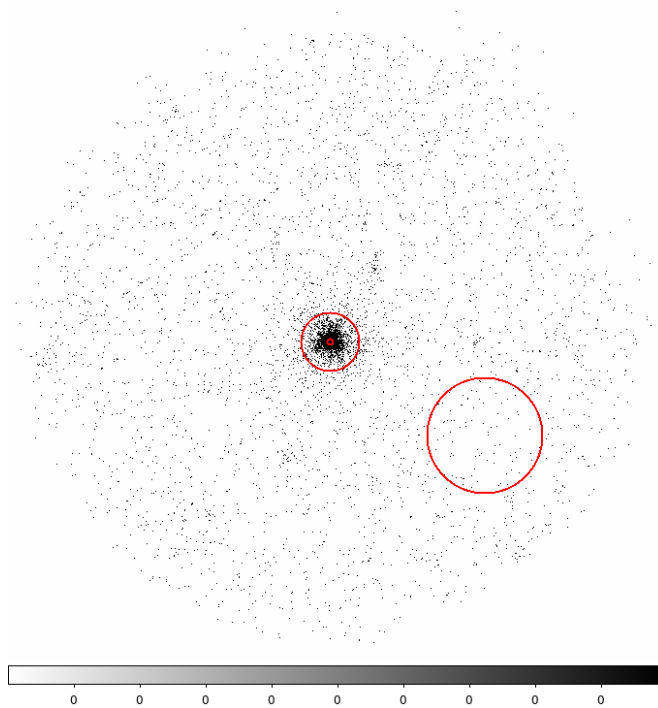

Figure 4.2: Combined *Swift*–XRT image of SWIFT J0513.4–6547 during 2009. Regions shown are used for extraction of background and source files.

4.3 Timing Analysis

4.3.1 Energy-Resolved Pulse Profile

The profile of the strong pulse detected in $RXTE$/PCA light curves of SWIFT J0513.4–6547 is double-peaked. One of the two peaks have more counts than the other, therefore one may call it the primary peak. The primary peak peaks at pulse phase ~ 0.75. The peaks of the pulse have similar phase duration, each having a coverage of ~ 0.5 phase. In order to identify any energy resolved variations of the pulse profile, profiles in four energy bands are constructed. Selected energy ranges are 3–7 keV, 7–10 keV, 10–16.5 keV and 16.5–25 keV. In the first band, 3–7 keV the source count rate is highest with an average of 3.2 cts s^{-1}. Remaining energy bands are selected to have similar count rates on average, approximately 1.7 cts s^{-1}. The pulse profiles constructed in these energies are given on the upper panels of Figure 4.3. Orbital and timing solutions are applied and $RXTE$/PCA data between MJD 54935–54950 are averaged during the extraction of pulse profiles from the phase-binned spectral files using the tool FBSSUM.

Using $RXTE$/PCA light curves in the selected energy bands, power spectra are also constructed for comparison (see the lower panels of Fig. 4.3). The double-peaked profile of the pulse is demonstrated by the strong power of the second harmonic frequency of the pulse, which is 0.0734 Hz. When compared with each other, 3–7 keV and 7–10 keV pulse profiles and power spectra are similar. The pulsed fraction of the 10–16.5 keV pulse profile significantly drops and its double-peaked structure strengthens. The count rate of the phase between the primary and the secondary peak (indicated with a dashed line in Fig. 4.3) reaches to the same level of the count rate of pulse minimum phase, which is the 0.0 phase. This change in 10–16.5 keV pulse profile, is displayed as an equivalence of the powers of the pulse and its second harmonic on the power spectrum of that band. As seen from Figure 4.3, the pulse is evident up to ~ 16.5 keV and it totally fades for 16.5–25 keV band. The powers of the pulse and its second harmonic are at the level of noise on the 16.5–25 keV power spectrum.
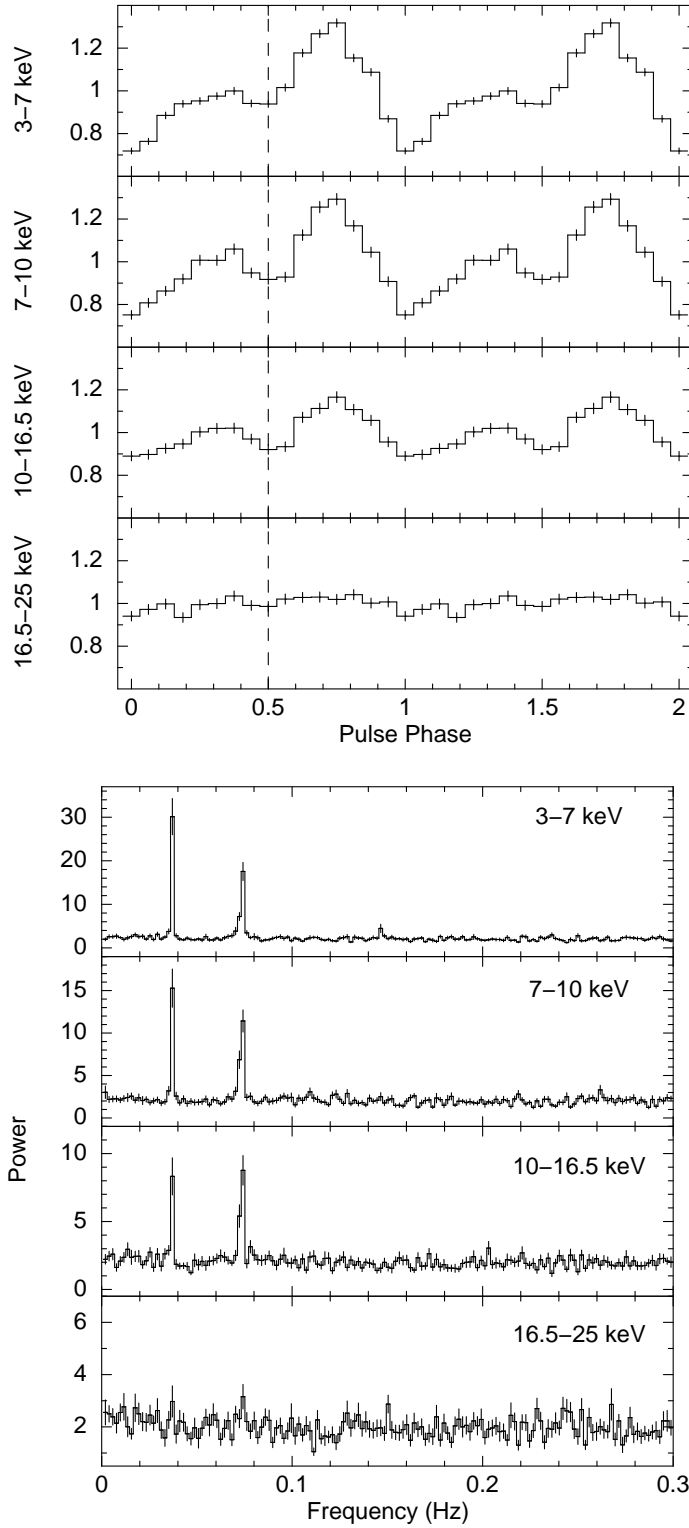
87

Figure 4.3: Energy resolved pulse profiles of *RXTE*/PCA observations are given on the upper panels. Y-axes are normalised counts from the energy bands given on y-axes labels. The dashed line represents the local minima in between the primary and the secondary peak. Energy resolved power spectra of the corresponding energy bands are given on the lower panels.
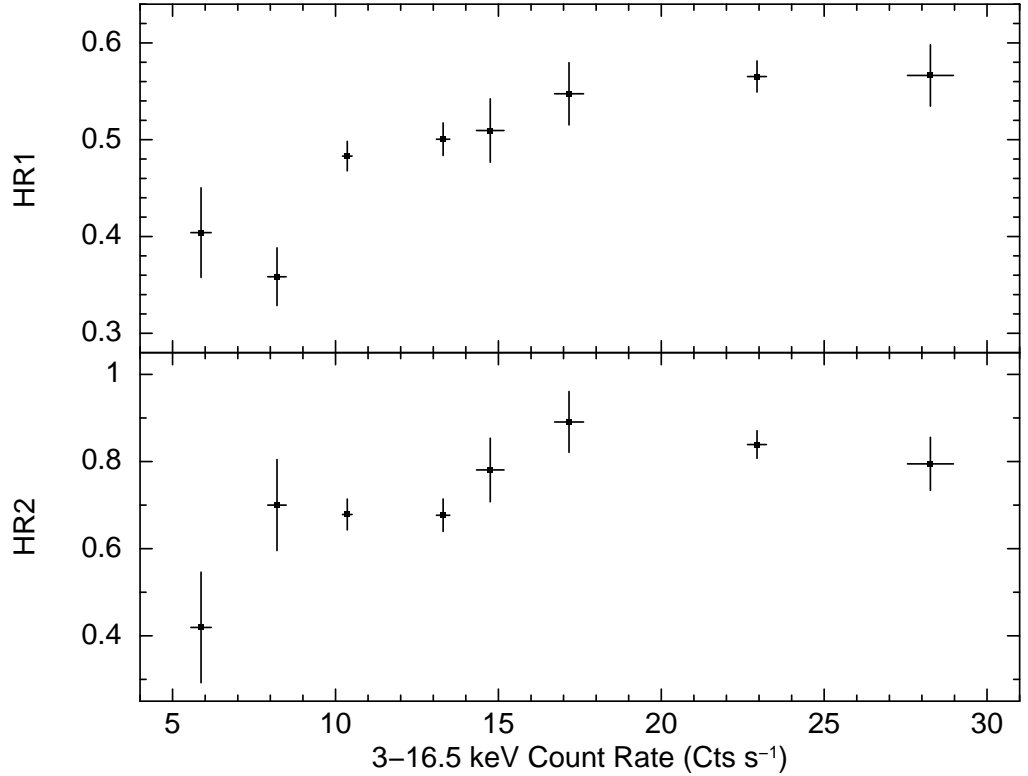
Figure 4.4: Count rate dependences of the hardness ratios. HR1 ($\frac{7-10 \text{ keV}}{3-7 \text{ keV}}$)and HR2 ($\frac{10-16.5 \text{ keV}}{7-10 \text{ keV}}$) are plotted over daily averaged 3–16.5 keV count rate.

4.3.2 Hardness Ratio

Energy dependent light curves of SWIFT J0513.4–6547 are also used to calculate the daily averaged hardness ratios (HR) of the source. The two HRs; HR1 = $\frac{7-10 \text{ keV}}{3-7 \text{ keV}}$ and HR2 = $\frac{10-16.5 \text{ keV}}{7-10 \text{ keV}}$ are plotted in Figure 4.4 with respect to daily averaged count rate. HR1 and HR2 both seem to be in correlation with the count rate, until a certain brightness is acquired by the source. When the 3–16.5 keV count rate of the source is lower than 17 cts s^{-1}, both HR1 and HR2 decreases with decreasing count rate, implying softer emission for lower count rates. On the contrary, when the 3–16.5 keV count rate of the source is higher than 17 cts s^{-1}, HR1 values seem to remain constant and HR2 values seem to be decreasing.

Further analysis of HRs is carried in pulse phase. HR1 and HR2 values in pulse
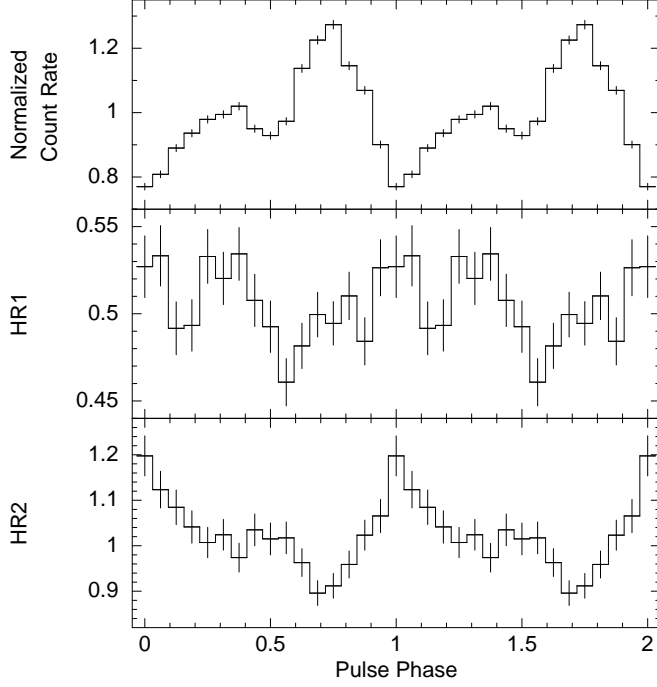
Figure 4.5: Pulse phase resolved hardness ratios. 3–16.5 keV pulse profile is plotted on the top panel. $\frac{7-10 \text{ keV}}{3-7 \text{ keV}}$ and $\frac{10-16.5 \text{ keV}}{7-10 \text{ keV}}$ count rate ratios are denoted as HR1 and HR2 on y-axes labels of the second and third panels, respectively.

phase are calculated from the un-normalized count rates of the pulse profiles given in Figure 4.3. In Figure 4.5 the pulse phase dependence of HR1 and HR2 are plotted. The top panel is the average pulse profile for 3–16.5 keV energy range, which is a combination of pulsed bands in Figure 4.3. HR2 is clearly in negative correlation with the count rate. The hardest phase corresponds to 0.0 phase and the softest phase corresponds to the primary peak of the pulse. However, the variation of HR1 with pulse phase is rather complex, showing no distinguishable similarity with the pulse profile of the source. HR1 reaches its minimum between the double peaks of the pulse at phase ∼ 0.5. Both the 0.0 phase and the secondary peak have the hardest ratio, whereas the primary peak has an average HR1 value. In addition, HR1 values are low for phases between 0.1 − 0.2, indicating a softening for these phases.

90
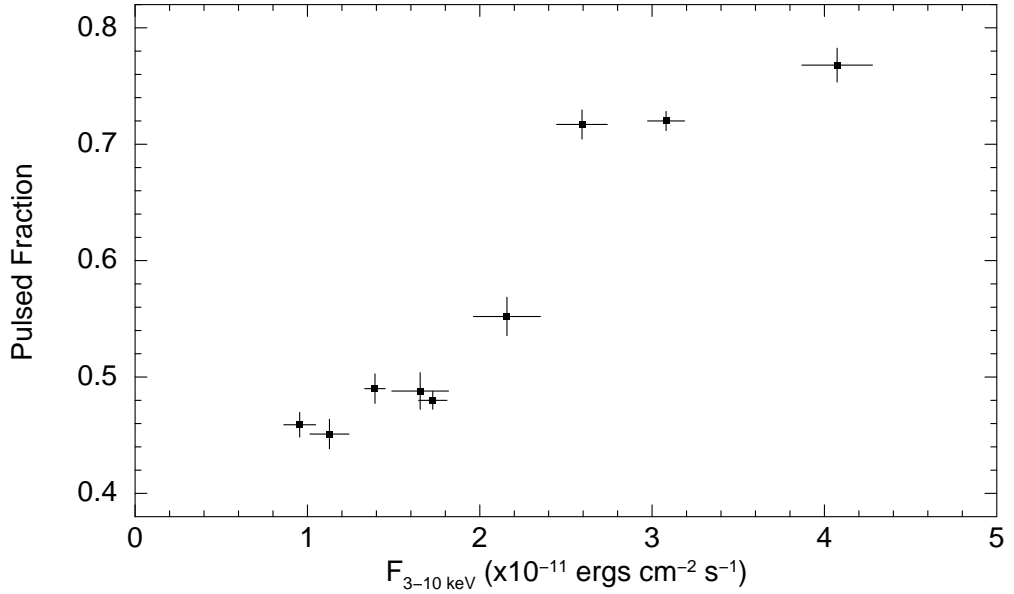
Figure 4.6: Pulsed fraction as a function of unabsorbed flux. Pulsed fractions are calculated in the energy range 3–16.5 keV.

4.3.3 Pulsed Fraction

The pulsed fraction (PF) of individual $RXTE$–PCA observations are calculated from the count rates of background subtracted phase-binned spectra in the energy range 3–16.5 keV. The standard definition; that is

$$PF = \frac{p_{max} - p_{min}}{p_{max} + p_{min}} \qquad (4.1)$$

[2] is used for calculations. Obtained results are plotted over 3–10 keV unabsorbed flux values measured from the spectral fits of individual observations (see Fig. 4.6). It is clearly evident that higher PF is measured for observations with higher flux values. The correlation of PF with the source flux indicates that more material fall onto the magnetic poles when the accretion rate is increased, since higher flux is a consequence of increased accretion rate. As a result, increased efficiency of accretion increases the amount of pulsed emission.

---

[2] p_{min} and p_{max} are minimum and maximum counts of the pulse
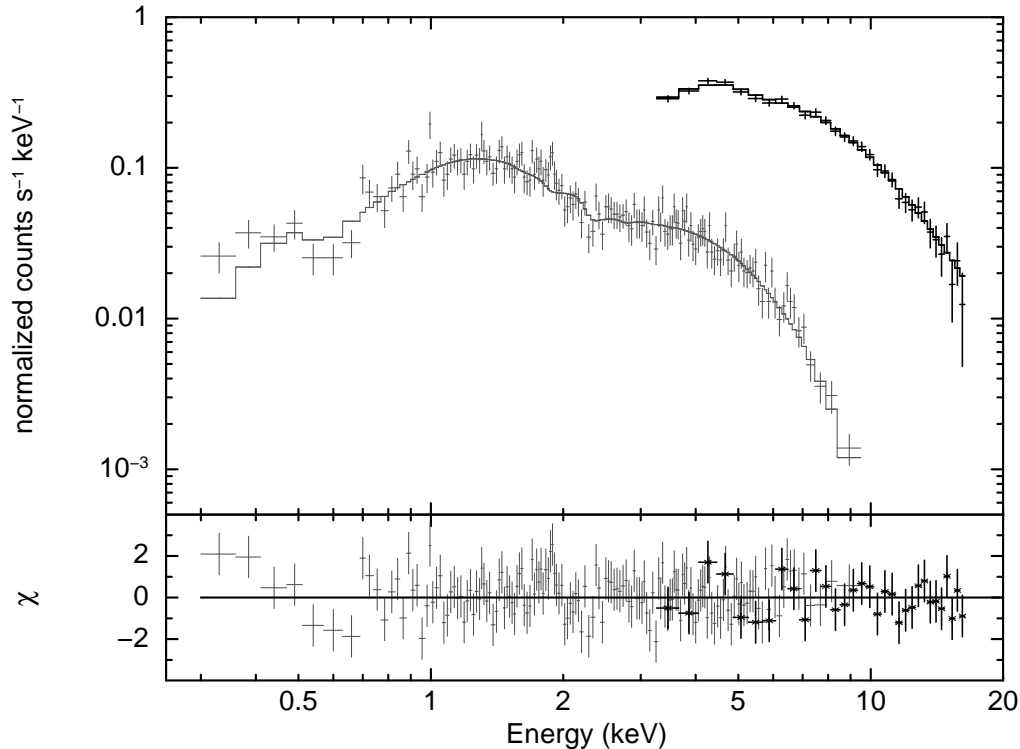
Figure 4.7: Simultaneous spectral fitting of *Swift*–XRT (0.3–9.5 keV; grey) and *RXTE*–PCA (3–16.5 keV; black) data from 2009. The data and its best fit with `PHABS*POW*HIGHECUT` ($\chi^2_{Red} = 0.98$; solid line) are shown in upper panel, the residuals are given in the lower panel. See Table 4.3 for the spectral parameters.

4.4 Spectral Analysis

4.4.1 Overall Spectrum during 2009

X-ray spectrum of SWIFT J0513.4–6547 is previously defined with a simple absorbed power law using *Swift*–XRT observations of the 2009 outburst (Krimm et al. 2009, Coe et al. 2015). In this work, results obtained by a re-analysis of 0.3–10 keV *Swift*–XRT spectrum is consistent with previous studies. However, a simultaneous fit of overall spectrum during 2009 using both instruments *Swift*–XRT and *RXTE*–PCA, could not be fully described by this basic model, giving a reduced χ^2 of 1.53 (see Table 4.3 for best fit parameters). During the simultaneous fit, the energy ranges considered for different instruments are 0.3–9.5 keV for XRT and 3–16.5 keV for PCA. The energies above 16.5 keV are excluded

for PCA, since the statistical significance of the spectral bins are very low. The exposure times are 12.7 ks for XRT and 17.9 ks for PCA spectra in 2009. The fitting model is multiplied by different constant factors for different detectors, in order to mimic the normalization uncertainty between the two instruments.

In order to improve the simultaneous fit of the overall spectrum during 2009, we tried to insert more components to the model. Similar improvements are achieved by two different models. Adding a blackbody component (`BBODYRAD`) or a high energy cut-off (`HIGHECUT`) to the model provide the same improvement by decreasing the reduced χ^2 to 0.96. Although both of these models are adequately observed in the spectra of HMXBs, the physical interpretations of the spectral parameters obtained for the case of SWIFT J0513.4–6547 should be cautiously discussed, with the intention of preferring the appropriate one.

The $kT_{BB} = 1.89 \pm 0.11$ keV found for the additional blackbody model is somewhat unusual among the HMXBs that show blackbody components in their X-ray spectra. Up to date the highest kT_{BB} is observed for another LMC source SWIFT J045106.8–694803, that is 1.8 keV (Bartlett et al. 2013). High kT_{BB} values above 1 keV are commonly attributed to thermal excess from the surface of the neutron star (Hickox 2004). Using the normalization of the `BBODYRAD` model, blackbody emitting radius is calculated as $R = 1.73 \pm 0.17$ km for SWIFT J0513.4–6547. This radius is also moderately large to be the radius of the emission region, which is the polar cap of a neutron star. In Table 1 of Bartlett et al. (2013) HMXB systems that show high kT_{BB} blackbody feature in their spectra are listed. A common property of these systems is that they are all low luminosity ($\sim 10^{34-35}$ erg s^{-1}) systems. Moreover the fractional contribution of blackbody flux to the 0.3–10 keV total unabsorbed flux of SWIFT J0513.4–6547 is rather low, which is about 30 per cent, while the contribution of the thermal emission is often expected to be high in soft energies. Alternatively, power law with high energy cut-off is a commonly used model for X-ray pulsar spectra. Although the cut-off energy $E_{cut} = 5.04^{+0.77}_{-0.67}$ keV measured for SWIFT J0513.4–6547 is at the lowest end of range of energies measured for other sources (e.g. for 4U 1626–67 $E_{cut} = 6.8$ keV, see Coburn et al. 2002), we prefer to represent the individual spectra of SWIFT J0513.4–6547 with the cut-off model.

Table4.3: Best fit spectral parameters for *Swift* 2009, *Swift* 2014 and for the simultaneous fitting of *Swift* and *RXTE* data from 2009 (see Fig. 4.7). All uncertainties are calculated at the 90 per cent confidence level. The acronyms used for the different model components are: *ph* for PHABS, *po* for POWERLAW, *bb* for BBODYRAD and *hi* for HIGHECUT.

Swift & *RXTE* 2009	*ph*po*	*ph*(bb+po)*	*ph*po*hi*
n_H [10^{21} cm^{-2}]	$2.58^{+0.33}_{-0.30}$	$1.66^{+0.29}_{-0.26}$	$1.20^{+0.24}_{-0.22}$
Γ	1.32 ± 0.04	1.32 ± 0.06	0.93 ± 0.04
kT_{BB} [keV]	–	1.89 ± 0.11	–
$R^{(a)}$ [km]	–	1.73 ± 0.17	–
E_{cut} [keV]	–	–	$5.04^{+0.77}_{-0.67}$
E_{fold} [keV]	–	–	$11.59^{+1.67}_{-1.56}$
Flux [b]	3.95 ± 0.15	4.06 ± 0.16	3.93 ± 0.14
χ^2_{Red} / dof	1.53/186	0.96/184	0.96/184

	n_H	Γ	Flux [b]	χ^2_{Red} / dof
Swift 2009	$1.35^{+0.31}_{-0.29}$	0.99 ± 0.07	4.2 ± 0.16	0.98/155
Swift 2014	$1.32^{+0.70}_{-0.58}$	$1.13^{+0.17}_{-0.16}$	0.8 ± 0.07	0.98/32

Notes. [a] Radius of the blackbody emitting region calculated from the normalization parameter of BBODYRAD model, assuming a 50.6 kpc distance to the LMC. [b] Unabsorbed flux values calculated using CFLUX model for the energy range 0.3–10 keV, in units of 10^{-11} erg cm^{-2} s^{-1}.
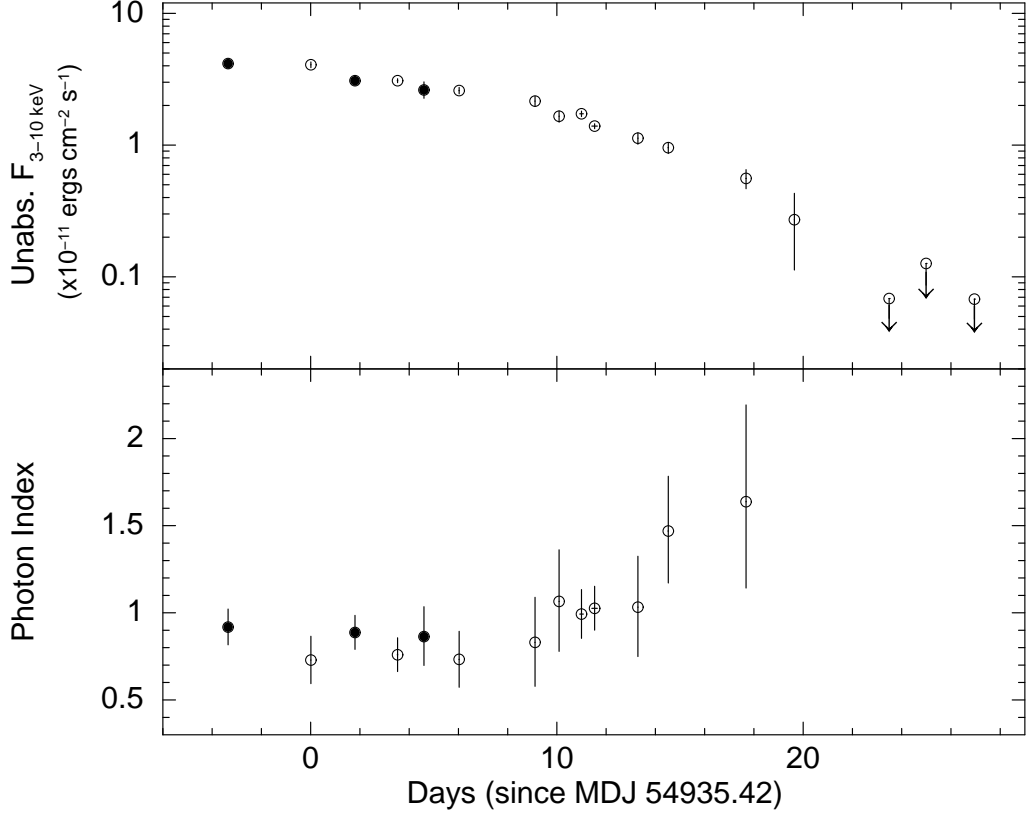
Figure 4.8: 3–10 keV unabsorbed flux (upper panel) and photon index (lower panel) measurements for the individual *Swift*–XRT (filled circles) and *RXTE*–PCA (empty circles) spectra from 2009. Error bars indicate uncertainties at 90 per cent confidence level.

4.4.2 Individual Spectra of 2009 observations

SWIFT J0513.4–6547 has 21 pointing observations recorded during the 2009 outburst, 18 of which are recorded with *RXTE* and 3 with *Swift*. The time span of these observations is about one month. In order to investigate any possible spectral variations throughout this period of time, we fit individual spectra using the power law with high energy cut-off model. Observations recorded on the same days are summed for an analysis on daily basis. Exposure times of resulting spectra were low about $\sim$ 1–2 ks. In combination with this fact the low count rates from the source resulted in low SNR spectra, therefore we fixed the cut-off model parameters (i.e. E_{cut} and E_{fold}) to their best fit values given in Tabel 4.3. Since no significant change could be observed in the low hydrogen column

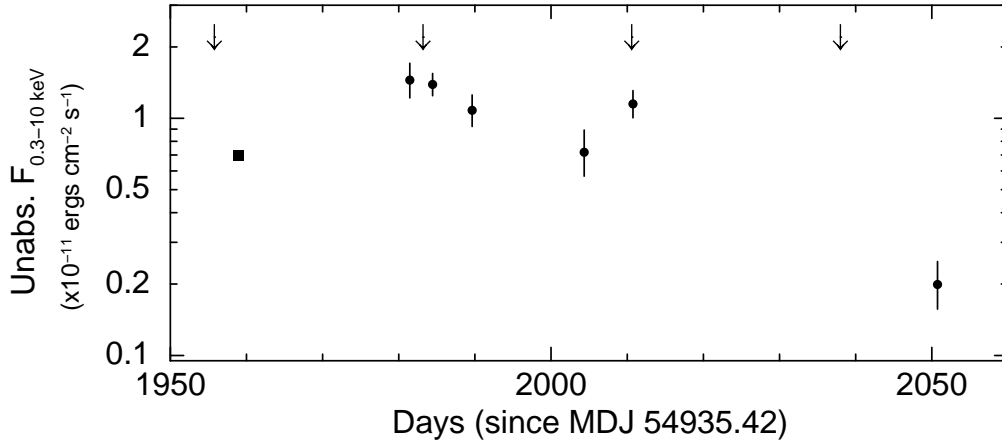Figure 4.9: Unabsorbed flux (0.3–10 keV) values measured for the individual spectra of *Swift* 2014 observations. The first data point at day ~ 1960 is the *XMM* flux measurement of Sturm et al. (2014). The arrows above show the times of optical maximum according to the ephemeris given in Coe et al. (2015). Error bars indicate uncertainties at 90 per cent confidence level.

density (n_H) along the line of sight, it is also fixed to its best fit value. 3–10 keV unabsorbed flux values are obtained with the help of the `CFLUX` model in `XSPEC`.

Spectral results obtained from 3 XRT and 14 PCA spectra are plotted in Figure 4.8. The upper panel demonstrates the flux decline of the 2009 outburst. Only an upper limit could be estimated for the flux of observations later than MJD 54955. The lower panel shows the variability of photon index during the 2009 outburst of SWIFT J0513.4–6547, in which the spectral index increases as the source flux decreases in time. A correlation between the photon index and the X-ray flux indicates that hard photons emerge from the source when the X-ray flux increases. Slightly higher photon index values measured for *Swift* (filled circles) spectra, than the indexes of *RXTE* (empty circles) spectra are probably because of the different energy bandpass of detectors.

4.4.3   Re-brightening in 2014

2014 re-brightening of SWIFT J0513.4–6547 has only 7 pointing *Swift* observations (each $\sim$1 ks) between MJD 56916 and 56986. The total spectrum, as the sum of all 2014 observations, is successfully modelled by a simple absorbed

96

power law model and similar parameters are obtained as in the case of *Swift* 2009 observations (see Table 4.3). The absorption parameter n_H is found to be just the same with 2009 measurements. The photon index is slightly larger than that of 2009, however the uncertainty is higher since the low count of 2014 spectrum cause a decline in the statistical quality of the data. Yet the higher spectral index may be a consequence of the lower flux of 2009 observations, since a flux dependence of the photon index is identified for in 2009 data of SWIFT J0513.4–6547 (see Fig. 4.8). The average X-ray flux of 2014 re-brightening is about 20 per cent of the average value of 2009 flux.

SWIFT J0513.4–6547 is sparsely monitored during 2014, there are only 7 observations within a time span of $\sim$ 70 days. In Figure 4.9 0.3–10 keV unabsorbed flux measurements of individual *Swift* spectra are given along with the *XMM-Newton* measurement on MJD 56894 (Sturm et al. 2014). Given that the *XMM-Newton* detection and the first *Swift* detection are close to the time of expected optical maxima Sturm et al. (2014) suggested that these might be recurrent outbursts of Type I. Calculating the optical maxima according to the ephemeris given in Coe et al. (2015), we signify them with arrows on Figure 4.9. Although it is not definitely possible to discriminate the type of the outbursts from only seven data points, the 2014 measurements resemble a series of Type I outbursts as it is suggested by Sturm et al. (2014). We observe one more supporting flux enhancement on MJD 56946 which exactly corresponds to the time of the next optical maximum. Furthermore, the peak flux measured for 2014 implies a luminosity of 4.3×10^{36} erg s^{-1} [3]. Therefore 2014 outburst of SWIFT J0513.4–6547 has two orders of magnitude lower luminosity than the 2009 outburst. This fact is in agreement with the Type I scenario for the 2014 re-brightening.

4.4.4   Pulse Phase Resolved Spectra

RXTE–PCA observations between MJD 54935–54950 are used to produce pulse phase resolved spectra of SWIFT J0513.4–6547. Timing and orbital parame-

---

[3]   using the LMC distance of $\sim$ 50 kpc
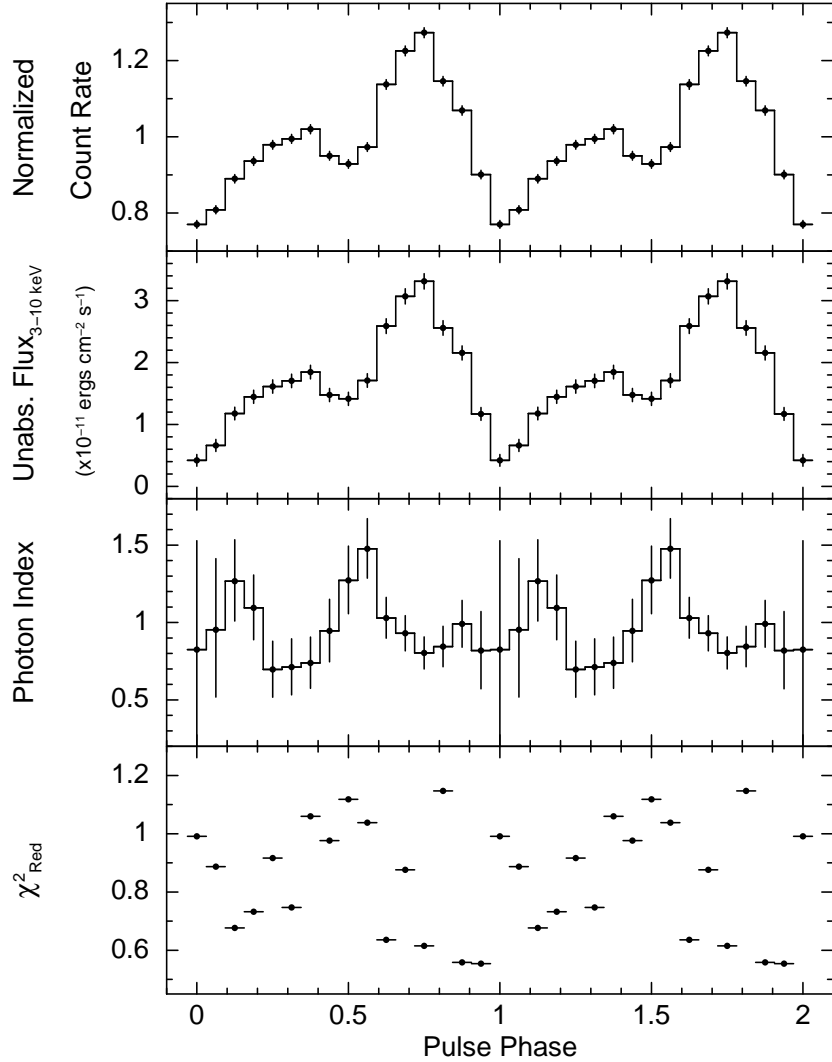
Figure 4.10: Pulse phase resolved spectral results for cut-off model. Results are deduced from 3–16.5 keV *RXTE*–PCA spectra for 16 phase bins. The 3–16.5 keV pulse profile is plotted on the top panel. 3–10 keV unabsorbed flux values are in agreement with the pulse profile (second panel). The photon index variation is plotted on the third panel. Reduced χ^2 of the fits are given on the bottom panel. All uncertainties are calculated at the 90 per cent confidence level. For clarity, the data points are repeated for a cycle.

ters are taken from Şahiner et al. (2015) and attached to the timing files (i.e. `psrtime.dat` and `psrbin.dat`) of the tool `FASEBIN`. Spectra of 16 bins in pulse phase are constructed in order to examine the pulse phase variability in spectral parameters. The exposure time of each phase bin turns out to be ~ 1.1 ks.

3–16.5 keV spectra are modelled with the high energy cut-off model. As described in Section 4.4.2 the cut-off parameters and n_H are fixed to their best fit values obtained for the overall spectra (see Table 4.3). Measured flux and photon index values are plotted over pulse phase in Figure 4.10. Flux measurements are in agreement with the pulse profile of SWIFT J0513.4–6547 which is given at the top panel of the same figure. The average value of the photon index is 0.93, however it definitely exceeds this value in some certain pulse phases. The steepest power law is observed in the phase ~ 0.5 with a measured index of 1.48. Both of the peaks of the double-peaked pulse have lower spectral indexes than the average, such as 0.7 and 0.8. The photon index is also high for phases between $0.1 - 0.2$. The spectral parameters of lowest count rate bins (i.e. phase 0.0 and 0.0625) are not constrained well, an average index is found with a large uncertainty for these phases. The phase dependence of photon index is not in a straightforward correlation with the flux. The variation is similar to the variation of HR1 in Figure 4.5. A high photon index and a low hardness ratio, both describe a softer spectrum. The reason why the phase dependence of photon index is only similar to one of the hardness ratios but not all might be due to the fact that the higher energy bands have less count rates, so even modest variations in these energy bands do not affect the photon indices significantly.

4.5 Summary and Discussion

In this chapter, two outburst events of the newly discovered *Be*/XB SWIFT J0513.4–6547 are studied by analyzing its observations with *RXTE* and *Swift* satellites. Here, the main work focuses on the X-ray spectral characteristics of the source. The properties of the pulse profile are also investigated. Although the detailed pulse timing analysis of the source is left beyond the scope of this work, the results are a part of the publication that is being prepared (Şahiner et

al. 2015). The source is found to be spinning up with a rate $1.74 \times 10^{-11} \mathrm{Hz} \ \mathrm{s}^{-1}$ during the final stage of its 2009 outburst. Comparison with the values found for the initial stages of the outburst (Coe et al. 2015) suggests that the spin rate of the source is correlated with the X-ray luminosity. Coe et al. (2015) declared that the correlation is as follows, $\dot{\nu} = 3.5 \times 10^{-11} \mathrm{Hz} \ \mathrm{s}^{-1} L_{38}^{6/7}$, where L_{38} is the luminosity in units of $10^{38} \mathrm{erg} \ s^{-1}$. Results of Şahiner et al. (2015) are consistent with this relation. Theoretical prediction of this correlation is a magnetic field at the order of 10^{13} G (Coe et al. 2015).

The pulse profile of SWIFT J0513.4–6547 is found to be evident until ~ 16.5 keV and its shape is double-peaked. No strong energy dependence is observed in pulse shape, although the pulse fraction decreases in the 10–16.5 keV band. Regardless of the energy band, the peaks have similar phase coverage, where the mid-point between primary and secondary peaks is at ~ 0.5 phase.

The time dependent hardness ratios of SWIFT J0513.4–6547 are found to be correlated with the count rate only up to certain brightness. When the count rate in 3–16.5 keV is lower than 17 cts s^{-1} a clear correlation indicates hardening with increasing count rate. For the observations which have count rates beyond this value (first three $RXTE$–PCA observations) hardness ratios are observed to be constant. The separation point correspond to 3–10 keV unabsorbed flux value of 2.8×10^{-11} ergs cm^{-2} s^{-1}. Using the distance of LMC as ~ 50 kpc the luminosity is calculated as 8.4×10^{36} erg s^{-1}. Postnov et al. (2015) recently reported similar hardness ratio variations depending on luminosity for several other transient sources (EXO 2030+375, GX 304–1, 4U 0115+63, V 0332+63, A 0535+26 and MXB 0656–072). These authors showed by numerical calculations of the accretion column structure that; this "saturation" behavior of the hardness ratio beyond certain luminosity is caused by the changing geometry of the accretion column due to increased accretion rate. They show that when $\dot{M}$ exceeds a critical value the height of the accretion column increases resulting in a regression of reflected radiation. Since reflected radiation is the main source of the spectral hardness, this regression shows itself as the saturation of the hardness ratio. The critical luminosity for this saturation effect to occur is determined from observations as few times 10^{37} erg s^{-1} (Postnov et al. 2015).

For the case of SWIFT J0513.4–6547 we find it slightly less.

The overall spectrum of 2009 outburst of SWIFT J0513.4–6547 needs an additional model component along with the basic model of a simple absorbed power law. Addition of a blackbody component peaking at $\sim$ 1.9 keV or a high energy cut-off component at $\sim$ 5 keV, both result in a similar statistical improvement in the spectral fit of the data. However the results are quite unusual for both, the blackbody kT and cut-off energy values reside marginal within the ranges observed in HMXB spectra. During the spectral analysis of individual observations we prefer to use the power law with high energy cut-off model due to better statistical confinement of the spectral parameters.

From the spectral analysis of individual observations we find that the photon index increases as the source flux decreases during 2009. Similar spectral dependence which might be an indication of accretion geometry changes due to mass accretion rate variations was also found for the X-ray pulsars SAX J2103.5+4545 (Baykal et al. 2002), 2S 1417–62 (İnam et al. 2004), XMMU J054134.7–682550 (İnam et al. 2009b), Her X–1 (Klochkov et al. 2011) and SWIFT J1626.6–5156 (İcdem, İnam & Baykal 2011).

For 2014 observations of SWIFT J0513.4–6547 no significant change in spectral properties could be observed. Yet, the average 2014 flux is measured to be about 20 per cent of the average value of 2009 flux. Three flux maxima detected in 2014 observations coincide with times of expected optical maxima according to the ephemeris of Coe et al. (2015). Although there are very few observations, 2014 activity of the source resembles a series of Type I outbursts. The peak luminosity of 2014 being at the order of 10^{36} erg s^{-1} is also in accordance with Type I scenario. Whereas the duration and the peak luminosity of 2009 outburst suitably allow one to identify the 2009 outburst as a Type II outburst.

Pulse phase resolved variations in the spectra of SWIFT J0513.4–6547 are analyzed using the first $\sim$ 17.6 ks $RXTE$–PCA data of 2009 outburst. The photon index is found to be changing with pulse phase, however the variation is not in a straightforward correlation with the phase resolved flux values. The midpoint between primary and secondary peaks at $\sim$ 0.5 phase has a steeper (softer)

spectrum with a power law index of 1.48, whereas the peaks have lower spectral indexes such as 0.7 and 0.8 indicating that the harder emission is emerging from the poles of the pulsar. The phase dependent change in the photon index resembles the pulse phase resolved variation of HR1. A high photon index and a low hardness ratio corresponding to the same pulse phases, both describe a softer spectrum. However the hardness ratio involving higher energy bands (i.e. HR2) shows a different hardness profile such that the primary peak is softer than that of the secondary peak and the hardest phase is the 0.0 phase. Therefore only HR2 seems to be correlated with the flux.

CHAPTER 5

CONCLUSION

In this thesis, X-ray characteristics of three HMXB systems are studied by analyzing observations from *RXTE*, *INTEGRAL* and *Swift* extensively. A major study on a historically well known source, 4U 1907+09, is combined with primitive work on the two newly discovered systems discovered by the *Swift* satellite. Although SWIFT J1729.9–3437 and SWIFT J0513.4–6547 are transient sources which have limited number of observations during their outbursts, a variety of X-ray properties could be resolved for these systems. The focus of the work on the persistent source 4U 1907+09 has become its exceptional dipping activity, while long term monitoring reveal the latest spin down episode of the pulsar in detail.

The timing analysis of 4U 1907+09 using *INTEGRAL* data between October 2005 and November 2007 give approximately steady pulse period $\sim$ 441.1 s. Later on timing solution obtained from the analysis of *RXTE* data between June 2007 and December 2011, show a long term spin down trend with a rate close to the older spin down rate of the source. Apart from its historical spin down trend, 4U 1907+09 were found in spin up once (for about $\sim$ 900 days) without any sign of a change in the mass accretion rate or X-ray spectral characteristics. Şahiner (2009) previously discussed the torque reversal event and mentioned a model that considers an asymmetric magnetospheric boundary (Perna et al. 2006). In this model, the variable radius of the boundary provokes different regions at which the accretion is halted or permitted and the dual characteristic of the disc might generate cyclic torque reversals without a significant change in accretion

rate. Despite the fact that 4U 1907+09 is found to be spinning down again, period measurements indicate small fluctuations are also evident. The nature of these fluctuations is investigated via power density spectrum of the source. The noise strength is found to be constant between analysis frequencies 1/1300 and 1/75 d^{-1}. Therefore the fluctuations are in agreement with the random walk model indicating a white noise in frequency derivatives of 4U 1907+09 and implies an accretion disk formation.

As *RXTE* observations of 4U 1907+09 are taken frequently along a time of 4.5 year, they cover a variety of orbital phases. This advantage allowed us to distinguish orbital dependence in the properties of the source. Orbital phase resolved X-ray spectroscopy verified a significant modification of the column density along the orbit. The column becomes Hydrogen rich just after the pulsar passes from the periastron, and the density of the absorbing material remains considerably high until the apastron, where it turns to its base value. The phase of maximum n_H lagging the periastron, implies the existence of a gas stream trailing behind the pulsar. A spirally structured dense material that catches the pulsar up but does not overtake it for about several orbital phases explains the preservation of high n_H. Another result from time resolved spectra is a correlation between spectral index and X-ray flux. The index is higher for higher flux values, specifying a softening with increasing flux.

Another property of 4U 1907+09, which the orbital dependence is investigated is its dipping activity. The incidence of dipping episodes noticeably increases after the apastron and a sharp decrease in the probability of observing a dip is discovered for phases corresponding to periastron and after. When the variation of the dipping probability over the orbit is compared with the n_H variation in non-dip observations, it is perceived that the phases of high n_H coincide with the lower possibility of observing a dip state, whereas the phases of low n_H coincide with high dipping possibility. Hence it is suitable to conjecture that the reason to be an altering structure in the spherical wind of the companion. Previous spectral studies on the dipping time data showing no clues of an absorber obscuring the X-ray source, the scenario of cessation of accretion becomes more appropriate to explain the dips of 4U 1907+09 and several other sources. Theoretical mod-

els showing that the density of clumps in the wind may change 3 to 5 orders, strengthens the possibility of propeller due to insufficient amount of matter. Remembering the detection of a QPO during periastron flares, the dominant accretion mechanism during the orbital half where dipping is less, could be an accretion disc formed around the pulsar. During the times when the dips occur more frequently, the disk might be running out of material and inhomogeneous clumpy wind structures become the dominant accretion mechanism. The dual wind and disc mechanism can also promote the random walk that is detected in frequency.

In 2010, the first and the only outburst of SWIFT J1729.9–3437 is monitored by *RXTE* and *Swift* for about three weeks. These observations are held subject to pulse timing analysis and the resulting quadratic solution bring up to date that the source is spinning up with a rate of $6.42(6) \times 10^{-12}$ Hz s^{-1}. The residuals of the timing solution are further investigated by means of two possibilities. A noise strength of 6.8×10^{-18} Hz s^{-2} successfully explains the residuals with random walk in pulse period. On the other hand, the residuals fit well to a circular model giving an orbital period of 15.3(2) days. SWIFT J1729.9–3437 takes its place in the wind-fed supergiant region of the Corbet diagram (Corbet 1984) with this orbit and its pulse period (533.76 s). The mass function of the system is calculated to be $\sim 1.3\, M_\odot$ by using the orbital parameters. The small mass function requires low orbital inclination, e.g. $i = 30^o$ would result in a companion mass of 12.47 $M_\odot$.

Temporal variations of the pulse profiles and hardness ratios of SWIFT J1729.9–3437 are examined. The double-peaked pulse profile transforms in to single-peaked during the decrease of the source flux. If this transition is representing a change from fan beam to pencil beam, an upper limit to distance could be calculated as $\sim$ 15 kpc by using the limiting luminosity for pattern change. However we did not observe any strong differences between the energy resolved pulse profiles, which would be the case for fan beams. The pulse is detected to be the strongest in energies between 8 and 18 keV. The hardness ratio, HR1 ($= \frac{8-13 \text{ keV}}{3-8 \text{ keV}}$) decreases with decreasing count rate. In other words, the hardening with increasing luminosity can be explained by an increase of inverse componiza-

tion process as the accretion rate increases. As the accretion column becomes denser in high energy electrons, the hard photons are produced via collisions between these electrons and soft photons.

Time resolved, pulse phase resolved and overall spectra of SWIFT J1729.9–3437 are examined. The data is best represented by a model of absorbed power law with a high energy cut-off, which is a basic model for accretion powered pulsars. A combination of all available observations strengthens the existence of Fe emission line at 6.51 keV. When time resolved spectra are studied, it is found that the Fe line flux is in correlation with the source flux. Therefore, we conclude that the Fe line originates from the fluorescence of surrounding matter via X-ray emission of the source. From the pulse phase resolved spectra, an increase in photon index during un-pulsed emission is detected. In addition, there is weak evidence that higher cut-off energies are measured for harder spectral index. The Hydrogen column density could only be measured for the overall spectrum and it is as high as 8.27×10^{22} cm^{-2}. This type of high absorption is not an uncommon property for wind-fed supergiant systems, as SWIFT J1729.9–3437 falls to the associated region of the Corbet diagram. However, classical wind-fed systems are persistent sources, whereas SWIFT J1729.9–3437 is of transient nature. Two new sub-classes are discovered in the past decade, SFXTs and Obscured HMXBs. As discussed in the end of Chapter 3 the resolved properties of SWIFT J1729.9–3437 allow one to predict that the source could be an obscured HMXB. The coordinates of the source is also in agreement with other obscured sources.

The source SWIFT J0513.4–6547 being identified as a Be/XB have gone under two active time periods. 2009 outburst of the source continued for about two months and it is monitored with $RXTE$ and $Swift$ satellites. The peak luminosity of this outburst was calculated as 1.3×10^{38} erg s^{-1} (Coe et al. 2015). Therefore 2009 outburst is a Type II outburst. In 2014 the source underwent another brightening episode, however this time the peak luminosity could only reach up to $\sim 10^{36}$ erg s^{-1}. Although the source could only be observed seven times in a ~ 70 day time interval, three flux maxima are measured in times of expected optical maxima. These findings strengthen the suggestion that the 2014 activity of the source consists of a series of Type I outbursts (Sturm et al.

2014).

As a part of the timing analysis of SWIFT J0513.4–6547 energy dependent pulse profiles, hardness ratios with respect to count rate and pulse phase, and flux dependence of pulse fraction are investigated. We find that the double-peaked pulse profile is preserved below $\sim$ 16.5 keV, whereas the pulse fades totally in above energies. Hardness ratios of the source demonstrate a correlation with the source count rate up to certain brightness, which means hardening with increasing count rate. Beyond separating luminosity; hardness ratios come to a "saturation" point, remain constant and they even slightly decrease. This behaviour is also observed for other transient sources by Postnov et al. (2015) and is explained by a geometrical change in the accretion column due to increased accretion rate. A reduction in the reflected radiation weakens the hard emission, due to increased height of the column. The pulse fraction of SWIFT J0513.4—6547 is found to be positively correlated with X-ray flux, which indicates increased efficiency of accretion.

In order to investigate general spectral properties of SWIFT J0513.4–6547, an overall 2009 spectrum is modelled. A simple power law model is found unsatisfactory to describe the continuum. Two models are tried for an improvement and both resulted in similar statistics. However the spectral parameters such as a blackbody component peaking at $\sim$ 1.9 keV or a high energy cut-off component at $\sim$ 5 keV reside marginal within the ranges observed in HMXB spectra. During the analysis of low exposure spectra from individual observations and different pulse phases we used the high energy cut-off model with fixed parameter. For the outburst in 2009 we observe an increase in photon index with decreasing flux. However the variation of photon index with pulse phase does not seem to correlate with flux directly. The double peaks of the pulse have lower spectral index than the index of their midpoint at phase $\sim$ 0.5. This behaviour is also observed in pulse phase resolved variation of HR1.

REFERENCES

[1] Balman S., 2009, AJ, 138, 50

[2] Barthelmy S. D., Barbier L. M., Cummings J. R. et al., 2005, Space Sci. Rev., 120, 143

[3] Bartlett E. S., Coe M. J., Ho W. C. G., 2013, MNRAS, 436, 2054

[4] Baykal A., İnam S. Ç., Alpar M. A., In't Zand J., Strohmayer T., 2001, MNRAS, 327, 1269

[5] Baykal A., Stark M. J., Swank J. H., 2002, ApJ, 569, 903

[6] Baykal A., İnam S. Ç., Beklen E., 2006, MNRAS, 369, 1760

[7] Baykal A., İnam S. Ç., Stark M. J., Heffner C. M., Erkoca A. E., Swank J. H., 2007, MNRAS, 374, 1108

[8] Becker P. A., Wolff M. T., 2007, ApJ, 654, 435

[9] Bildsten L., Chakrabarty D., Chiu J. et al., 1997, ApJS, 113, 367

[10] Blondin J. M., Kallman T. R., Fryxell B. A., Taam R. E., 1990, ApJ, 356, 591

[11] Bondi H., Hoyle F., 1944, MNRAS, 104, 273

[12] Boynton P. E., Groth E. J., Hutchinson D. P., Nanos G. P. Jr., Partridge R. B., Wilkinson D. T., 1972, ApJ, 175, 217

[13] Bozzo E., Falanga M., Stella L., 2008, ApJ, 683, 1031

[14] Burnard D. J., Arons J., Lea S. M., 1983, ApJ, 266, 175

[15] Burrows D. N., Hill J. E., Nousek J. A. et al., 2005, Space Sci. Rev., 120, 165

[16] Cash W., 1979, ApJ, 228, 939

[17] Chaty S., 2011, ASP Conference Proceedings, Vol. 447, p.29

[18] Chitnis V. R., Rao A. R., Agrawal P. C., Manchanda R. K., 1993, A&A, 268, 609

[19] Church M. J., Dotani T., Balucinska-Churc, M., Mitsuda K., Takahashi T., Inoue H., Yoshida K., 1997, ApJ, 491, 388

[20] Coburn W., Heindl W. A., Rothschild R. E. et al., 2002, ApJ, 580, 394

[21] Coe M. J., Finger M., Bartlett E. S., Udalski A., 2015, MNRAS, 447,1630

[22] Coe M. J., Udalski A., Finger M., 2013, ATel, 5511

[23] Cook M. C., Page C. G., 1987, MNRAS, 225, 381

[24] Corbet R. H. D., 1984, A&A, 141, 91

[25] Corbet R. H. D., 1986, MNRAS, 220, 1047

[26] Cordes J. M., 1980, ApJ, 237, 216

[27] Cox N. L. J., Kaper L., Mokiem M. R., 2005a, A&A, 436, 661

[28] Cox N. L. J., Kaper L., Foing B. H., Ehrenfreund P., 2005b, A&A, 438, 187

[29] Cui W., 1997, ApJ, 482, L163

[30] Cusumano G., di Salvo T., Burderi L., Orlandini M., Piraino S., Robba N., Santangelo A., 1998, A&A, 338, L79

[31] Davidson K., Ostriker J. P., 1973, ApJ, 179, 585

[32] Deeter J. E., 1981, Ph.D. Thesis, Washington Univ., Seattle

[33] Deeter J. E., 1984, ApJ, 281, 482

[34] Deeter J. E., Boynton P. E., 1985, in Hayakawa S. and Nagase F., Proc. Inuyama Workshop: Timing Studies of X-Ray Sources, p.29, Nagoya Univ., Nagoya

[35] Deeter J. E., Boynton P. E., Lamb F. K., Zylstra G., 1989, ApJ, 336, 376

[36] Doroshenko V., Santangelo A., Suleimanov V., 2011, A&A, 529, A52

[37] Doroshenko V., Santangelo A., Ducci L., Klochkov D., 2012 A&A, 548, A19

[38] Drave S. P., Bird A. J., Townsend L. J. et al., 2012, A&A, 539, 21

[39] Elsner R. F., Lamb F. K., 1977, ApJ, 215, 897

[40] Filliatre P., Chaty S., 2004, ApJ, 616, 469

[41] Finger M. H., Beklen E., 2009, ATel 2023

[42] Frank J., King A., Raine D. J., 2002, Accretion Power in Astrophysics: Third Edition, Cambridge University Press, Cambridge

[43] Fritz S., Kreykenbohm I., Wilms J. et al., 2006, A&A, 458, 885

[44] Fürst F., Kreykenbohm I., Wilms J., Kretschmar P., Klochkov D., Santangelo A., Staubert R., 2008, Conf. Proc. of 7th INTEGRAL workshop, PoS Integral08:119

[45] Fürst F. et al. 2011, A&A, 535, 9

[46] Gehrels N., Chincarini G., Giommi P. et al., 2004, ApJ, 611, 1005

[47] Ghosh P., Lamb F. K., 1978, ApJ, 223L, 83

[48] Ghosh P., Lamb F. K., 1979a, ApJ, 232, 259

[49] Ghosh P., Lamb F. K., 1979b, ApJ, 234, 296

[50] Ghosh P., 2007, Rotation and Accretion Powered Pulsars, World Scientific Publishing Co., Pte. Ltd., Singapore

[51] Giacconi R., Kellogg E., Gorenstein P., Gursky H., Tananbaum H., 1971, ApJ, 165, L27

[52] Göğüş E., Kreykenbohm I., Belloni T. M., 2011, A&A, 525L, 6

[53] Haberl F., White N. E., 1990, ApJ, 361, 225

[54] Haberl F., White N. E., Kallman T. R., 1989, ApJ, 343, 409

[55] Hemphill P. B., Rothschild R. E., Caballero I., Pottschmidt K., Kühnel M., Fürs, F., Wilms J., 2013, ApJ, 777, 61

[56] Hickox R. C., Narayan R., Kallman T. R., 2004, ApJ, 614, 881

[57] Hoyle F., Lyttleton R. A., 1939, PCPS, 34, 405

[58] Illarionov A. F., Sunyaev R. A., 1975, A&A, 39, 185

[59] İçdem B., İnam S. Ç., Baykal A. 2011, MNRAS, 415, 1523

[60] İnam S. Ç., Baykal A., Scott D.M., Finger M., Swank J., 2004, MNRAS, 349, 173

[61] İnam S. Ç., Şahiner Ş., Baykal A., 2009a, MNRAS, 395, 1015

[62] İnam S. Ç., Townsend L. J., McBride V. A., Baykal A., Coe M. J., Corbet R. H. D., 2009b, MNRAS, 395, 1662

[63] In't Zand J. J. M., Strohmayer T. E., Baykal A., 1997, ApJ, 479, L47

[64] In't Zand J. J. M., Baykal A., Strohmayer T. E., 1998, ApJ, 496, 386

[65] Iye M., 1986, PASJ, 38, 463

[66] Jain C., Paul B., Dutta, A., 2010, MNRAS, 403, 920

[67] Klochkov D., Santangelo A., Staubert R., Rothschild R. E., 2011, Conf. Proc. of 8th INTEGRAL Workshop, arXiv:1105.3547

[68] Kostka M., Leahy D. A., 2010, MNRAS, 407, 1182

[69] Kreykenbohm I., Wilms J., Kretschmar P. et al., 2008, A&A, 492, 511

[70] Krimm H. A., Corbet R. H. D., Evans P. A. et al., 2009, ATel 2011

[71] Krimm H. A., Holland S. T., Corbet R. H. D., 2013, ApJS, 209, 14

[72] Lamb F. K., Pethick C. J., Pines D., 1973, ApJ, 184, 271

[73] Lamb F. K., Pines, D., Shaham, J., 1978a, ApJ, 224, 969

[74] Lamb F. K., Pines, D., Shaham, J., 1978b, ApJ, 225, 582

[75] Lamb F. K., 1989, in Ögelman, H., van den Heuvel, E. P. J., Timing Neutron Stars, p.649, Dordrecht, Kluwer

[76] Leahy D. A., Darbro W., Elsner R. F., Weisskopf M. C., Kahn S., Sutherland P. G., Grindlay J. E., 1983, ApJ, 266, 160

[77] Leahy D. A., Matsuoka M., Kawai N. and Makino F., 1989, MNRAS, 236, 603

[78] Leahy D. A., 2001, Proc. 27th International Cosmic Ray Conference, p.2528, Copernicus Gesellschaft, Hamburg

[79] Leahy D. A., Kostka M., 2008, MNRAS, 384, 747

[80] Lebrun F., Leray J. P., Lavocat P. et al., 2003, A&A, 411, L141

[81] Levine A. M., Bradt H., Cui W. et al. 1996, ApJ, 469, 33

[82] Liu Q. Z., van Paradijs J., van den Heuvel E. P. J., 2006, A&A, 455, 1165

[83] Liu Q. Z., van Paradijs J., van den Heuvel E. P. J., 2007, A&A, 469, 807

[84] Liu Q. Z., Chaty S., Yan J. Z. 2011, MNRAS, 415, 3349

[85] Lund N., Budtz-Jorgensen C., Westergaard N. J. et al. 2003, A&A, 411, L231

[86] Ohashi T., Inoue H., Koyama K. et al., 1984, PASJ, 36, 699

[87] Negueruela I., Torrejon J. M., Reig P., Ribo M., Smith D. M., 2008, AIPC, 1010, 252

[88] Maitra C., Paul B., 2013, ApJ, 771, 96

[89] Makishima K., Kawai N., Koyama K., Shibazaki N., 1984, PASJ, 36, 679

[90] Makishima K., Ohashi T., Kawai N. et al., 1990, PASJ, 42, 295

[91] Makishima K., Mihara T., Nagase F., Tanaka Y., 1999, ApJ, 525, 978

[92] Markwardt C. B., Krimm H. A., Swank J. H., 2010a, Atel 2747

[93] Markwardt C. B., Krimm H. A., Swank J. H., 2010b, Atel 2749

[94] Marshall N., Ricketts M. J., 1980, MNRAS, 193, P7

[95] Mas-Hesse J. M., Gimenez A., Culhane J. L. et al. 2003, A&A, 411, L261

[96] Matsuda T., Inoue M., Sawada K., 1987, MNRAS, 226, 785

[97] Miceli M., Decourchelle A., Balle, J. et al., 2006, A&A, 453, 567

[98] Mihara T., 1995, PhD thesis, RIKEN, Tokyo

[99] Mihara T., Makishima K., Ohashi T., Sakao T., Tashiro M., 1990, Nature, 346, 250

[100] Moretti A., Campana S., Mineo, T. et al., 2005, SPIE, 5898, 360

[101] Mukerjee K., Agrawal P. C., Paul B., Rao A. R., Yadav J. S., Seetha S., Kasturirangan K., 2001, ApJ, 548, 368

[102] Nagase F., 1989, PASJ, 41, 1

[103] Nagel W., 1981, ApJ, 251, 278

[104] Negueruela I., Smith D. M., Reig P. et al. 2006, ESASP, 604, 165

[105] Negueruela I., Torrejon J. M., Reig P., Ribo M., Smith D. M., 2008, AIP Conference Proceedings, Vol. 1010, 252

[106] Naik S., Paul B., Ali Z., 2011, ApJ, 737, 79

[107] Nespoli E., Fabregat J., Mennickent R. E., 2008, A&A, 486, 911

[108] Parmar A.N., White N.E., Stella L., 1989, ApJ, 338, 373

[109] Paul B., Agrawal P.C., Rao A.R., Manchanda R.K., 1997, A&A, 319, 507

[110] Perna R., Bozzo E., Stella L., 2006, ApJ, 639, 363

[111] Postnov K. A., Gornostaev M. I., Klochkov D. et al., 2015, MNRAS, 452, 1601

[112] Pringle J. E., Rees M. J. 1972, A&A, 21, 1

[113] Reig P., 2011, Ap&SS, 332, 1

[114] Reig P., Nespoli E., 2013, A&A, 551, A1

[115] Rivers E., Markowitz A., Pottschmidt K. et al., 2010, ApJ, 709, 179

[116] Roberts M. S. E., Michelson P. F., Leahy D. A., Hall T. A., Finley J. P., Cominsky L. R., Srinivasan R., 2001, ApJ, 555, 967

[117] Rothschild R. E., Blanco P. R., Gruber D. E. et al. 1998, ApJ, 496, 538

[118] Runacres M. C., Owocki S. P., 2005, A&A, 429, 323

[119] Schwartz D. A., Griffiths R. E., Bowyer S., Thorstensen J. R., Charles P.A., 1980, AJ, 85, 549

[120] Sguera V., Barlow E. J., Bird A. J. et al. 2005, A&A, 444, 221

[121] Sguera V., Bazzano A., Bird A. J. et al. 2006, ApJ, 646, 452

[122] Shakura N. I., Postnov K. A., Kochetkova A. Yu., Hjalmarsdotter L., 2014, EPJ Web of Conferences, Vol. 64, id.02001

[123] Sidoli L., Romano P., Mereghetti S. et al. 2007, A&A 476, 1307

[124] Sidoli L., Romano P., Mangano V. et al. 2008, ApJ, 687, 1230

[125] Sidoli L., 2009, AdSpR, 43, 1464

[126] Sidoli L., 2011, in PoS(Texas 2010)082, 25th Texas Symposium on Relativistic Astrophysics

[127] Sidoli L., 2013, in Proc. 9th INTEGRAL Workshop, (arXiv:1301.7574)

[128] Smith D. M., Main D., Marshall F. et al. 1998, ApJ, 501, L181

[129] Stella L., White N. E., Rosner R., 1986, ApJ, 308, 669

[130] Stevens I. R., 1988, MNRAS, 232, 199

[131] Sturm R., Carpano S., Haberl F., Maggi P., Vasilopoulos G., 2014, ATel 6483

[132] Şahiner Ş. 2009, M.S. Thesis – Middle East Technical University, Ankara

[133] Şahiner Ş., İnam S. Ç., Baykal A., 2011, AIPC, 1379, 214

[134] Şahiner Ş., İnam S. Ç., Baykal A., 2012a, MNRAS, 421, 2079

[135] Şahiner Ş., İnam S. Ç., Baykal A., Kızıloğlu Ü., 2012b, Conf. Proc. of 9th INTEGRAL Workshop, id.32

[136] Şahiner Ş., Serim M. M., İnam S. Ç., Baykal A. 2015, submitted to MN-RAS

[137] Şahiner Ş., İnam S. Ç., Serim M. M., Baykal A., 2013, MNRAS, 434, 2772

[138] Taam R. E., Fryxell B. A., Brown D. A., 1988, ApJ, 331, 117

[139] Ubertini P., Lebrun F., Di Cocco G. et al., 2003, A&A, 411, L131

[140] Valinia A., Marshall F. E., 1998, ApJ, 505, 134

[141] Vedrenne G., Roques J. P., Schönfelder V. et al. 2003, A&A, 411, L63

[142] Walter R., Zurita-Heras J., 2007, A&A, 476, 335

[143] Walter R., Lutovinov A. A., Bozzo E., Tsygankov S. S., 2015, A&ARv, 23, 2

[144] Waters L. B. F. M., van Kerkwijk M. H., 1989, A&A, 223, 196

[145] Wang Y. M., Welter G. L., 1981, A&A, 102, 97

[146] White N. E., Swank J. H., 1982, ApJ, 253, L61

[147] White N. E., Swank J. H., HoltS. S., 1983, ApJ, 270, 711

[148] Winkler C., Courvoisier T. J. L., Di Cocco G. et al. 2003, A&A, 441, L1

[149] Zel'Dovich Y. B., Shakura N. I., 1969, SvA, 13, 175

CURRICULUM VITAE

PERSONAL INFORMATION

Surname, Name: Şahiner, Şeyda

Nationality: Turkish (TC)

Date and Place of Birth: 04.04.1983, Beyoğlu

Phone: +90312 2104319

Fax: +90312 2105099

e-mail: seyda@astroa.physics.metu.edu.tr

EDUCATION

Degree	Institution	Place	Grad. Date
Ph.D.	Department of Physics, METU	Ankara	August 2015
M.S.	Department of Physics, METU	Ankara	September 2009
B.S.	Department of Physics, METU	Ankara	July 2006
High School	Beyoğlu Anatolian High School	İstanbul	June 2001

PROFESSIONAL EXPERIENCE

Year	Place	Enrollment
Apr 2015 – Present	METU	Project Asistant TÜBİTAK:114F345
Sept 2013 – Feb 2015	Başkent Uni.	Part-Time Instructor;Freshmen Physics
Apr 2010 – Apr 2013	METU	Project Asistant TÜBİTAK:109T748
Jan 2009 – Feb 2009	ESA/ESAC	Visiting Researcher;COSPAR Fellowship
Apr 2007 – July 2009	METU	Project Asistant TÜBİTAK:106T040

PUBLICATIONS

1. **Şahiner, Ş.**; Serim, M. M.; İnam, S. Ç.; Baykal, A. "RXTE and Swift observations of SWIFT J0513.4–6547", submitted to MNRAS (2015)

2. Acuner, Z.; İnam, S. Ç.; **Şahiner, Ş.**; Serim, M. M.; Baykal, A.; Swank, J. "Timing studies of X Persei and the discovery of its transient quasi-periodic oscillation feature", MNRAS, 444(1), 457-465 (2014)

3. **Şahiner, Ş.**; İnam, S. Ç.; Serim, M. M.; Baykal, A. "RXTE and Swift observations of SWIFT J1729.9–3437", MNRAS, 434(4), 2772-2778 (2013)

4. **Şahiner, Ş.**; İnam, S. Ç.; Baykal, A. "A comprehensive study of RXTE and INTEGRAL observations of the X-ray pulsar 4U 1907+09", MNRAS, 421(3), 2079-2087 (2012)

5. İnam, S. Ç.; **Şahiner, Ş.**; Baykal, A. "Recent torque reversal of 4U1907+09", MNRAS, 395(2), 1015-1020 (2009)

International Conference Publications

1. **Şahiner, Ş.**; İnam, S. Ç.; Baykal, A.; Kızıloğlu, Ü. "Analysis on RXTE, INTEGRAL and ROTSE IIId observations of the X-ray Pulsar 4U 1907+09", Proceedings of 9th INTEGRAL Workshop, Published online at `http://pos.sissa.it/cgi-bin/reader/conf.cgi?confid=176`, id.32, (2012)

2. **Şahiner, Ş.**; İnam, S. Ç.; Baykal, A. "Recent Spin Rate Measurements of 4U 1907+09", AIP Conference Proceedings, 1379, 214-216 (2011)